OPTICAL AND ELECTROLUMINESCENT PROPERTIES OF IMIDAZOLE BASED SMALL MOLECULES

A THESIS SUBMITTED TO
THE GRADUATE SCHOOL OF NATURAL AND APPLIED SCIENCES
OF
MIDDLE EAST TECHNICAL UNIVERSITY

BY

FATMA ELİF DEMİRGEZER

IN PARTIAL FULFILLMENT OF THE REQUIREMENTS
FOR
THE DEGREE OF MASTER OF SCIENCE
IN
CHEMISTRY

JUNE 2024

Approval of the thesis:

OPTICAL AND ELECTROLUMINESCENT PROPERTIES OF IMIDAZOLE-BASED SMALL MOLECULES

submitted by **FATMA ELİF DEMİRGEZER** in partial fulfillment of the requirements for the degree of **Master of Science** i**n Chemistry, Middle East Technical University** by,

Prof. Dr. Naci Emre Altun
Dean, Graduate School of **Natural and Applied Sciences** _____

Prof. Ali Çırpan
Head of the Department, **Chemistry** _____

Prof. Dr. Ali Çırpan
Supervisor, **Chemistry, METU** _____

Dr. Gönül Hızalan Özsoy
Co-Supervisor, **ODTÜ-GÜNAM** _____

Examining Committee Members:

Prof. Dr. Levent Toppare
Chemistry, METU _____

Prof. Dr. Ali Çırpan
Chemistry, METU _____

Assist. Prof. Dr. Erol Yıldırım
Chemistry, METU _____

Prof. Dr. Emren Nalbant
Chemistry, METU _____

Prof. Dr. Yasemin Arslan Udum
Chemistry and Chemical Processing Technologies, Gazi University _____

Date: 06.06.2024

I hereby declare that all information in this document has been obtained and presented in accordance with academic rules and ethical conduct. I also declare that, as required by these rules and conduct, I have fully cited and referenced all material and results that are not original to this work.

Name Last name : Fatma Elif Demirgezer

Signature :

ABSTRACT

OPTICAL AND ELECTROLUMINESCENT PROPERTIES OF IMIDAZOLE-BASED SMALL MOLECULES

Demirgezer, Fatma Elif
Master of Science, Chemistry
Supervisor : Prof. Dr. Ali Çırpan
Co-Supervisor: Dr. Gönül Hızalan Özsoy

June 2024, 92 pages

OLEDs are the trending topic in the lighting and display industry because of their properties, such as being flexible, highly bright, and thinner. In this thesis, the synthesis of imidazole-bearing small molecules with different substituents and their application to OLEDs were studied. Moreover, the effects of substituents in imidazole molecules on OLEDs were examined. In order to investigate the electronic properties CV studies were performed. Photoluminescence peaks were centered at 490, 492, 495, 488, 490, and 489 nm for 2-(4-(tert-butyl)phenyl)-4,5-diphenyl-1H-imidazole (BIm-H-*t*Bu), 2-(4-(tert-butyl)phenyl)-1-(4-chlorophenyl)-4,5-diphenyl-1H-imidazole (BIm-PhCl-*t*Bu), 2-(4-(tert-butyl)phenyl)-1,4,5-triphenyl-1H-imidazole (BIm-Ph-*t*Bu), 2-(4-methoxyphenyl)-4,5-diphenyl-1H-imidazole (BIm-H-OMe), 2-(4-methoxyphenyl)-1,4,5-triphenyl-1H-imidazole (BIm-Ph-OMe), 1-(4-chlorophenyl)-2-(4-methoxyphenyl)-4,5-diphenyl-1H-imidazole (BIm-PhCl-OMe), respectively. Electroluminescent properties were investigated with the device architecture of ITO/ α-NPD/ Small Molecules/ TPBi/ LiF-Al with the incorporated OLED; the luminance value was exceeded of 10,000 $cd.m^{-2}$, and current efficiency of 5.9 and 7.73 $cd.A^{-1}$ were achieved. These results are promising for first-generation OLEDs.

Keywords: Blue emitting materials, OLED, Imidazole core, Substituent effect, Color purity

ÖZ

İMİDAZOL BAZLI KÜÇÜK MOLEKÜLLERİM OPTİK VE ELEKTRİKLE IŞILDAMA ÇALIŞMALARI

Demirgezer, Fatma Elif
Yüksek Lisans, Kimya
Tez Yöneticisi: Prof. Dr. Ali Çırpan
Ortak Tez Yöneticisi: Dr. Gönül Hızalan Özsoy

Haziran 2024, 92 sayfa

OLED'ler, esnek, çok parlak ve daha ince olmaları gibi özelliklerinden dolayı aydınlatma ve ekran endüstrisinde trend konusudur. Bu projede, farklı sübstitüentlerle imidazol küçük moleküllerinin sentezi ve OLED'lere uygulanması incelenmiştir. Ayrıca imidazol moleküllerindeki sübstitüentlerin OLED'ler üzerindeki etkileri incelenmiştir. Bu çalışmada, farklı sübstitüentlere sahip imidazol içeren küçük moleküller sentezlendi. Elektronik özelliklerini araştırmak için döngüsel voltametri çalışmaları yapılmıştır. Fotolüminesans tepe noktaları, 2-(4-(tert-butil)fenil)-4,5-difenil-1H-imidazol (BIm-H-*t*Bu), 2-(4-(tert-butil)fenil)-1-(4-klorofenil)-4,5-difenil-1H-imidazol (BIm-PhCl-tBu), 2-(4-(tert-butil)fenil)-1 ,4,5-trifenil-1H-imidazol (BIm-Ph-tBu), 2-(4-metoksifenil)-4,5-difenil-1H-imidazol (BIm-H-OMe), 2-(4-metoksifenil) -1,4,5-trifenil-1H-imidazol (BIm-Ph-OMe), 1-(4-klorofenil)-2-(4-metoksifenil)-4,5-difenil-1H-imidazol (BIm-PhCl-OMe) için sırasıyla 490, 492, 495, 488, 490, 489 nm'de merkezlenmiştir. ITO/ α-NPD/ Small Molecules/TPBi/ LiF-Al cihaz mimarisi ile entegre OLED ile elektrominesans özellikleri araştırılmış, 10,000 $cd.m^{-2}$ parlaklık değeri aşılarak 5,9 ve 7,73 $cd.A^{-1}$ akım etkinliği elde edilmiştir.

Anahtar Kelimeler: Mavi ışıyan malzemeler, Organik ışık yayan diyot, İmidazol, renk saflığı, Substituent etkisi

I dedicate this thesis to Marie Curie, whose lifelong dedication to science has inspired me, as well as to all other women in science whose achievements fuel my passion for research and science.

ACKNOWLEDGMENTS

First and foremost, I would like to express my deepest gratitude to my supervisor, Prof. Dr. Ali Çırpan. I feel incredibly fortunate to have had the opportunity to work with him, starting from the moment he accepted me into his research group. Throughout this journey, he has consistently supported me and had more faith and confidence in my abilities than I did. Whenever I had concerns or doubts, he went above and beyond to help me, always illuminating my path in my research endeavors. I am fortunate to have a supervisor like Prof. Dr. Ali Çırpan.

I would like to extend my thanks to my co-supervisor, Dr. Gönül Hızalan Özsoy, for her support and guidance throughout this journey. She consistently illuminated my path and broadened my horizons. Her advice on my research topics, the knowledge she imparted, and the experiences she shared were invaluable to me. These contributions played a significant role in my development in this field.

I would like to declare my gratitude to my thesis defense committee members, Prof. Dr. Levent Toppare, Assist. Prof. Dr. Erol Yıldırım, Prof. Dr. Emren Nalbant, and Prof. Dr. Yasemin Arslan Udum for their valuable recommendations.

I would like to extend my deepest gratitude to Dr. Şevki Can Cevher for his support and valuable insights during the synthesis part of this work and Assist. Prof. Dr. Erol Yıldırım, who added significant value to the research and broadened our perspectives through his theoretical studies.

I am thankful to Duygu Cevher for her assistance during the electrochemical studies and to Tuğba Hacıefendioğlu for her computational studies.

I would especially like to thank Dr. Eda Alemdar. Throughout this process, whether near or far, I always felt her presence and support. She always listened to and understood me, becoming one of my most incredible supporters during this journey. I also want to extend my heartfelt thanks to Mert Can Erer. Both of them shared their practical and theoretical knowledge regarding my research topics with me, and I am

very grateful for that. Additionally, I would like to express my gratitude to Dr. Mustafa Yaşa. These three individuals are among the most valuable people I have met here. They have indeed been a rock for me, offering both emotional and practical assistance. I am so thankful for their friendship.

I would also like to thank my colleagues and friends, Pelin Oral, Selin İlter, Esra Yenidoğan, and Elif Pınar Yılmaz. Working with them has been both enjoyable and incredibly fun.

I am truly grateful to my dear friend Özge for the enduring support and friendship since high school. Working with you in the lab has been a distinct pleasure, and I appreciate the late-night study sessions, shared laughter, and countless memories we have created together.

I would like to express my heartfelt gratitude to my beloved family, Hakan Demirgezer, Leyla Demirgezer, and Emir Demirgezer. Their unconditional support and the opportunities they have provided me both financially and emotionally are invaluable. I can never repay their countless efforts. Their presence is my most significant source of strength. I am deeply thankful for their endless love and for always being there to support and comfort me through every challenge.

Last but not least, I would like to express my gratitude towards Ahmet Yiğit Dip, whose presence in my life brings me joy every single day. Whenever I needed a helping hand, you were there to lift me up, offering unwavering support and being my biggest cheerleader. Your dedication to my personal growth and progress has never wavered. I carry you in my heart throughout this journey, knowing that you are always by my side. Your continuous love and support have been a cornerstone of my strength. I feel incredibly fortunate to have you in my life, and I am genuinely grateful for all that you do.

I would like to thank the Scientific and Technological Research Council of Turkey (TUBITAK) for their financial support (Project number: 122F307).

TABLE OF CONTENTS

LIST OF TABLES

TABLES

LIST OF FIGURES

FIGURES

LIST OF ABBREVIATIONS

ABBREVIATIONS

OLED: Organic Light-Emitting Diodes

PL: Photoluminescence

PI: Phenanthrol-imidazole

BI: Benzimidazole

LED: Light Emitting Diode

WOLED: White light-emitting OLED

HOMO: Highest Occupied Molecular Orbital

LUMO: Lowest Unoccupied Molecular Orbital

ITO: Indium Tin Oxide

ETL: Electron Transport Layer

HTL: Hole Transport Layer

HIL: Hole Injection Layer

EIL: Electron Injection Layer

V_{on}: Turn-on voltage

CE: Current Efficiency

EQE: External Quantum Efficiency

CIE: Commission Internationale de l'éclairage

CV: Cyclic Voltammetry

LiF: Lithium Fluoride

CHAPTER 1

INTRODUCTION

1.1 Use of Imidazole Small Molecules

Imidazole (1,3-diazole) is a planar five-membered ring-shaped molecule containing two nitrogen atoms, as shown in Figure 1.1. The two nitrogen atoms in the structure have different characteristics. One exhibits pyrrole characteristics, and the other is pyridine [1,2]. In addition to that, one of the imino nitrogen as an acceptor and hydrogen in amino nitrogen forms hydrogen bonding [3].

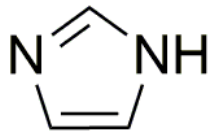

Figure 1.1. Structure of imidazole core unit.

The applications of imidazole molecules range from technology to medical applications. For example, catalytic use, agrochemical, pharmaceutical, and organic optoelectronics for energy, lighting, and display industry applications are the application areas of imidazole derivatives [4–7].

Due to their versatile features, they are popular in bioactive and biomedical utilizations. Its capability of forming hydrogen and metal-ligand bonding makes these molecules suitable for use in membrane and DNA sequencing applications [8]. Moreover, there are several studies of using imidazole derivatives in medicinal prospects of neurodegenerative diseases such as Alzheimer's disease. Cornec et al. used the leveraging of the ease of synthesis and synthetic versatility of the imidazole molecule and developed multi-targeted imidazole derivatives to be cured in degenerative brain disorders [9].

Many organic units such as triarylamine, imidazole, carbazole (Cz), triphenylphosphine oxide (PO), pyrene, etc., have the ability to emit light at the blue light range enhanced by adding functional groups to reach pure, bright, and stable blue color. They have become a frequently used emitting material, particularly in developing blue-emitting Organic Light-Emitting Diodes (OLEDs) [10]. Their essential photoluminescence (PL), electrochemical, and electroluminescence properties make them worth investigating [11]. Since the introduction of organic light-emitting diodes (OLEDs) in 1987 by Tang et al., the imidazole derivatives, primarily phenanthrol-imidazole (PI) and Benzimidazole (BI), have gotten a lot of press. Stable at 400°C, the imidazole derivatives have a strong aromatic character and easily undergo the standard electrophilic aromatic substitution processes. Moreover, their simplicity of production in a singular process, straightforward molecular adjustments, and ambipolar attributes have contributed to the widespread adoption of these compounds for use in the OLED device layers. They have also been proven as significant high-efficiency blue light emitters for improving device performances and fabricating stable OLEDs [12]. All the properties make the imidazole derivatives suitable for OLED manufacturing. In 2002, Aminul Islam et al. developed bis-imidazole derivatives to use as a dopant blue emitting OLED material, reaching higher than 4000 $cd.m^{-2}$ lumen and current efficiency around 2 $cd.A^{-1}$ values [13].

1.2 Principle and Classification of Luminescence

As in principle, any type of energy cannot be created from nothing so that light is released as a result of the transformation of another type of energy. There are two types of emission: incandescence and luminescence. Incandescence is the emission of light due to the material's temperature in the visible region of the electromagnetic spectrum. In addition to that, it is called black body radiation. This phenomenon can also be described as the emission of light due to heat energy. A Tungsten light bulb, the Sun, and a candle are examples of light sources that glow up because of their

heat. The other emission type that will interest us in this study is luminescence. In contrast to incandescence, it is called ‘cold body radiation’ since its light emission does not arise from its own heat; however, certain triggering events occur within the material. Therefore, it is given different names according to the sources of excitation. Chemiluminescence (a chemical reaction is the source of luminescence), cathodoluminescence (an electron causes to excite the material), triboluminescence (luminescence resulting in mechanical stimulation), electroluminescence (emission of light due to the electrical field) and photoluminescence (excitation of material by a photon) are the most common examples of luminescence [14]. Here, we are interested in photoluminescence and electroluminescence.

1.2.1 Photoluminescence

When a photon hit a molecule and the molecule absorbs the light energy, it becomes excited. This means that an electron from its ground state moves to a higher energy state. Due to the excited electron not being stable, it tends to go back to the ground state. Considering the principle that energy cannot be created or destroyed, whereas can only change from one form to another when an excited electron returns to its ground state, it will convert some of the absorbed energy back into the light, leading to its observation as the emission of light. This phenomenon is illustrated in Figure 1.2. The absorbed energy (energy of the photon) is not equal to the emitted energy due to the several non-radiative decays, such as collisional quenching, internal quenching, and vibrational relaxations [15].

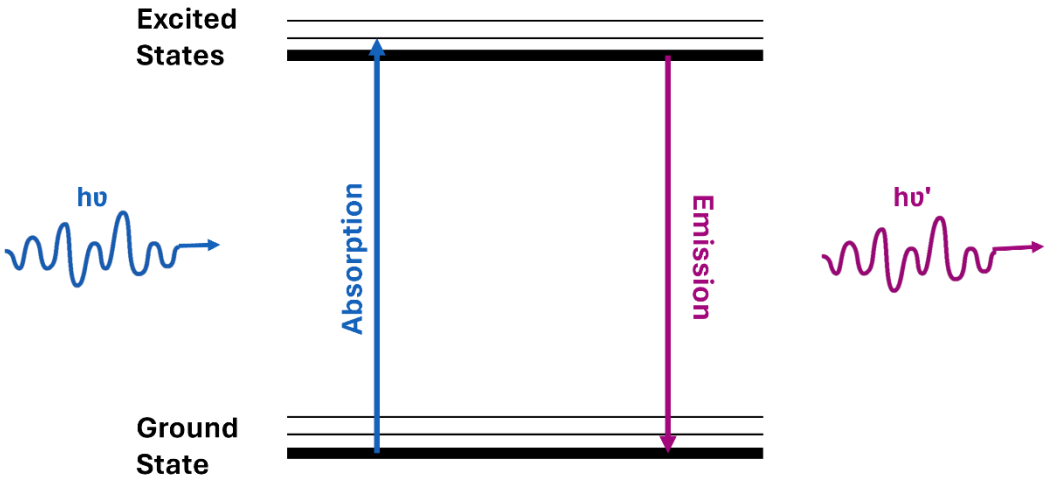

Figure 1.2. Schematic representation of photoluminescence phenomena.

Radiative emission takes place through two distinct processes: fluorescence and phosphorescence.

- Fluorescence:

  As shown in Figure 1.3, when an electron is excited from the ground state (S_0) to the singlet excited state (S_1), its emission mechanism is called fluorescence. The singlet excited state electron and the remaining ground state electron are paired, which means they have opposite spins. Therefore, its relaxation to the ground state is a spin-allowed process. As a result, the relaxation process is accelerated in nanoseconds (the rate of the fluorescence mechanism is around 10^8 s^{-1}) [16,17].

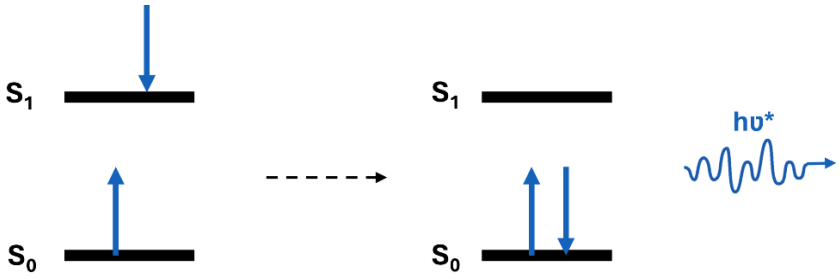

Figure 1.3. Schematic representation of fluorescence phenomena.

- Phosphorescence:

After absorbing a photon, the molecule reaches the singlet excited state. Subsequently, the excited electron reaches the triplet excited state through a non-radiative process known as intersystem crossing. As seen in Figure 1.4, electrons in the S_0 and triplet excited (T_1) states have the same spin, so the transition from T_1 to S_0 is forbidden. The electron then reaches the ground state via spin-orbit coupling. Consequently, the transition rate is shallow, leading to a millisecond-scale phosphorescence lifetime.

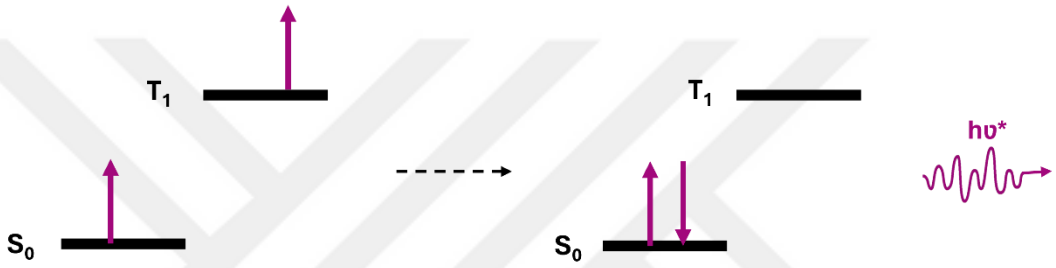

Figure 1.4. Schematic representation of phosphorescence.

1.2.2 Electroluminescence

Electroluminescence is when a material emits light upon applying an external voltage or electric field. Destriau first described this optoelectronic process as the emission of light following exposure to an electrical field [18]. The exposure of current to the material causes the movement of electrons and holes; then, their recombination creates photons, which are the excited states in molecules[19]. Electroluminescence, as a form of luminescence, is distinguished from incandescence by its nonthermal light generation. This process is schematically represented in Figure 1.5. The excited electrons can be classified into two groups, singlet, and triplet, depending on the excitation level which the singlet and triplet excited states. Similar to the photoluminescence mechanism, the relaxation of electrons from the S_1 state results in fluorescence, while relaxation from the T_1

state results in phosphorescence. After the recombination of charge carriers, the excitons separated into singlet and triplet excited states at 25% and 75%.

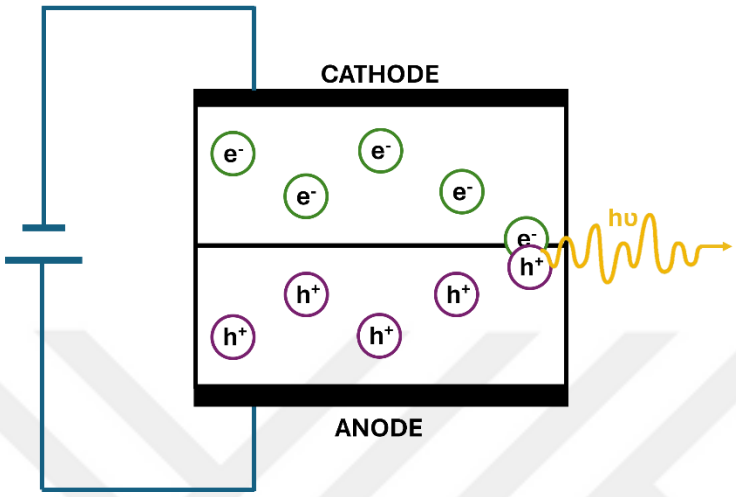

Figure 1.5. Schematic representation of the electroluminescence phenomenon.

1.3 Organic Light Emitting Diodes (OLEDs)

In the 21st century, around 17% of electricity is used for lighting worldwide [20]. This situation brought about the search for alternative ways to decrease the over-consumption of electricity. After extensive investigation, LED and OLED technologies were developed instead of incandescent and fluorescent lighting.

Organic Light-Emitting Diodes (OLEDs) are organic electronics composed of a sandwich-like structure with multiple functional layers [21]. Organic conjugated polymers or small molecules- semiconducting materials- are used to transport charges and active materials to emit light or transfer charge carriers in light-emitting devices.

Those new technologies have advantages like lowering the consumption of electricity and increasing efficiency. Except for lighting, OLED technology is used

in smartphones, smartwatches, and TV displays. Features like flexibility and transparency are applicable to human skin. Those technologies are based on electroluminescence phenomena, which refer to the conversion of electricity to light energy [22].

The OLED technology provides remarkable benefits over its counterpart technology products, such as inorganic Light Emitting Diodes (LEDs). Although both technologies are greener and more efficient than incandescent and fluorescent lighting, OLED technology has received considerable attention from both the display and lighting industry and also the academics over the last few decades due to their apparent advantages, including ease of preparation, low cost, safe use, lightweight, low driving voltage, and fast reaction [23]. Because of the promise of obtaining long-lasting, durable, and energy-efficient OLEDs, researchers dedicate a significant amount of time and effort to improving OLED technology and developing sophisticated OLEDs for the increasing demand for these products. Thanks to the rapid advancement in the manufacturing of stable and more efficient OLEDs, technology leaders have introduced various display products into the commercial marketplace, benefitting from the outstanding properties of OLEDs, such as being highly luminescent, flexible, and thin products. Due to their transparency, low power consumption, and renewable energy, OLEDs are increasingly recognized and widely employed in numerous industries [24]. Becoming a hot topic in materials chemistry and engineering, OLED technology showed incredible progress in device effectiveness and development. In the upcoming decades, these technology products will be seen more in the market, and outstanding developments will be expected.

1.3.1 A Brief History of Organic Light Emitting Diodes (OLEDs)

Before OLED technology evolved to its present state, in 1963, Pope, Kalman, and Magnante achieved fluorescence emission with anthracene and tetracene-doped anthracene after the application of high-level voltage [25]. Until 1987, there was a lot of research on this subject, but OLED performances suffered from high driving

voltages, instability, and lack of device efficiencies [26,27]. At that time, Tang and VanSlyke developed an OLED device using Tris(8-hydroxyquinoline)aluminum (Alq_3) as the emissive material. This device exhibited characteristics such as a low operating voltage of around 2.5 V and a high luminescence exceeding 1000 $cd.m^{-2}$ [28]. In the year 1999, Pioneer introduced the initial commercial OLED, which was incorporated into an automotive audio system [29]. After a duration of 8 years, the pioneering release of the world's initial OLED Television set as the XEL1 model was accomplished by the renowned Sony corporation [30]. The first-generation OLEDs follow the fluorescence mechanism, and because only 25% of the excitons can be harvested, the reachable maximum external quantum efficiency (EQE) is 5%. Then, the second-generation OLEDs are based on the phosphorescence mechanism. With this mechanism, 100% internal quantum efficiency can be achieved by using the complexes of heavy atoms and organic molecules. Nevertheless, the utilization of heavy atoms presents several drawbacks, such as elevated expenses and adverse environmental impacts. [31]. The third-generation OLEDs are based on thermally activated delayed fluorescence (TADF), a concept first introduced by Adachi and his colleagues in 2011 5.6% EQE [32]. Subsequently, in 2012, 12.5% EQE was achieved for green-emitting OLEDs [33].

1.3.2 Device Structure and Working Principle of OLEDs

OLEDs can be designed as single-layered or multilayered. Single-layer devices have the most straightforward OLED architecture, which consists of an organic emissive layer sandwiched between the metal anode and cathode layer (e.g., Al, Ca, Mg, etc.). The anode material used in organic optoelectronics should be transparent to get through the light emission. Moreover, this material should be chosen with a work function coherent with the HOMO level of the emissive layer because this affects the injection of electrons from the anode layer to the HOMO (Highest Occupied Molecular Orbital) level of the emissive material. Generally, indium tin oxide (ITO), a transparent conductive material, is preferred as an anode. The work function of

ITO (ϕ_{ITO}) is around 4.5 eV [34]. The other transparent alternatives to ITO are molybdenum oxide (MbO) and zinc oxide (ZnO) [35]. Moreover, organic conjugated polymers or organic small molecules are used as the emissive layer. The first transfer of an injected hole is performed from this layer, which means that the energetic barrier between the cathode, which is electron-injecting contact, and the LUMO (Lowest Unoccupied Molecular Orbital) level of the adjacent layer has crucial importance on the turn-on voltage value and the performance of the device. The materials with low $\phi_{cathode}$, such as Ba and Li, are feasible to reach the ohmic behavior. However, there is a problem with their reactivity toward the atmospheric water and oxygen because of their low $\phi_{cathode}$. For this reason, metals with higher work functions, such as Al (4.2 eV), are generally used as the cathode layer. Other alternatives for the cathode layer are Ca (2.9 eV) and Mg (3.7 eV), etc. [34].

Figure 1.6 shows the working principles of single-layered and multilayer OLEDs. For single-layered OLEDs, electrons are injected into the LUMO level of the organic emissive material upon applying a driving voltage to the cathode layer. At the same time, holes are injected from the anode to the HOMO level of the organic emissive material. In the emissive layer, recombining electrons and holes creates excitons, which means an excited states of the molecules. The relaxation of electrons from the excited state to the ground state results in the emission of light [34]. The working principle of multilayer OLEDs has the same trend as single-layered OLEDs, with differences in auxiliary layers. Upon applying a voltage to the cathode counterpart of the device, electrons are injected into the adjacent Electron Transport Layer (ETL) that supports the transport of electrons to the LUMO level of the emissive layer. In the meantime, from the anode counterpart, the holes are injected into the Hole Transport Layer (HTL), easing the transport of holes to the HOMO level of the Organic Emissive Layer [36]. In the emissive layer, like in the case of single-layered OLEDs, the holes generated from the anode and the electrons generated from the cathode combine to yield excitons, which are the bound state of the holes and excitons. The emission of light takes place due to the relaxation from the excited state to the ground state [37].

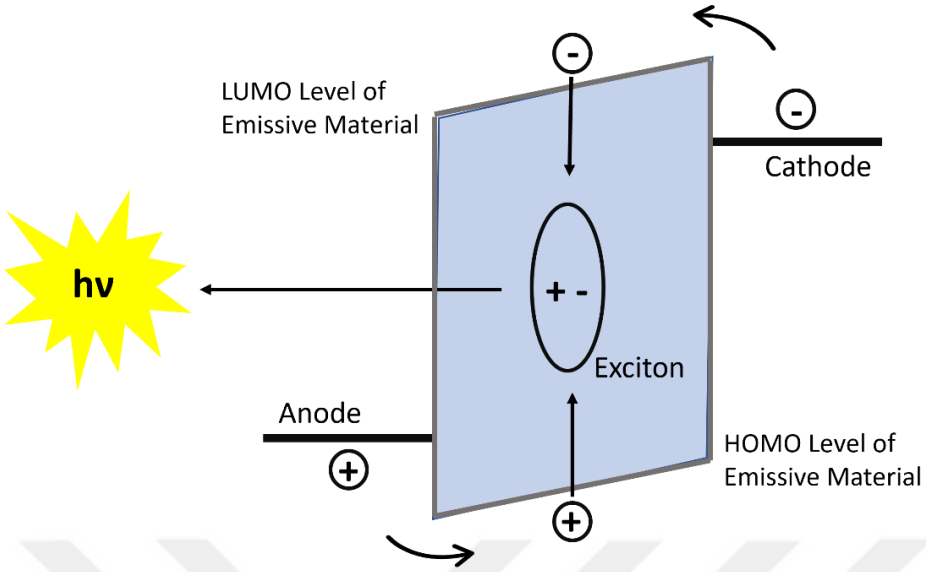

Figure 1.6. Schematic representation of the working principle of OLEDs.

High quantum efficiency is achieved by decreasing the charge injection after applying driving voltage and confining the injected electrons inside the organic emissive layer to increase the possibility of recombination of electrons and holes to create excitons. For this purpose, multi-layer OLEDs are used to enhance device efficiency [38]. Multilayered devices can be composed of a hole transport layer (HTL), a hole injection layer (HIL), an electron transport layer (ETL), and an electron injection layer (EIL). The injection layers are commonly used for extraction of charge carriers from electrodes in an effective way.

A typical OLED is made up of an emissive organic layer sandwiched between two electrodes, the anode and cathode, which are all placed on a glass substrate. Organic molecules become electrically conductive because of the delocalization of π-electrons generated by conjugation over a part of the molecule or all of the structure. These materials are classified as organic semiconductors because their conductivity values range between insulators to conductors [39]. Figure 1.7. shows a multilayer OLED construction. The anode part of the device is constructed on a glass substrate. An anode is an OLED device's positively charged counterpart, enabling the injection of holes into the organic layers. The commonly used anode material is Indium Tin Oxide (ITO). It is transparent to visible light and has a high work function, allowing

holes to be injected into the Highest Occupied Molecular Orbital (HOMO) of the organic emissive layer. Deviations in the surface of the anode reduce anode-organic film interface adhesion and increase electrical resistance [40]. All the drawbacks of the anode part of the fabricated OLEDs reduce their lifetime. Thin films are possible mechanisms for reducing anode roughness for ITO/glass substrates. To improve OLED performance and lifetime, new substrates and anode materials are being examined.

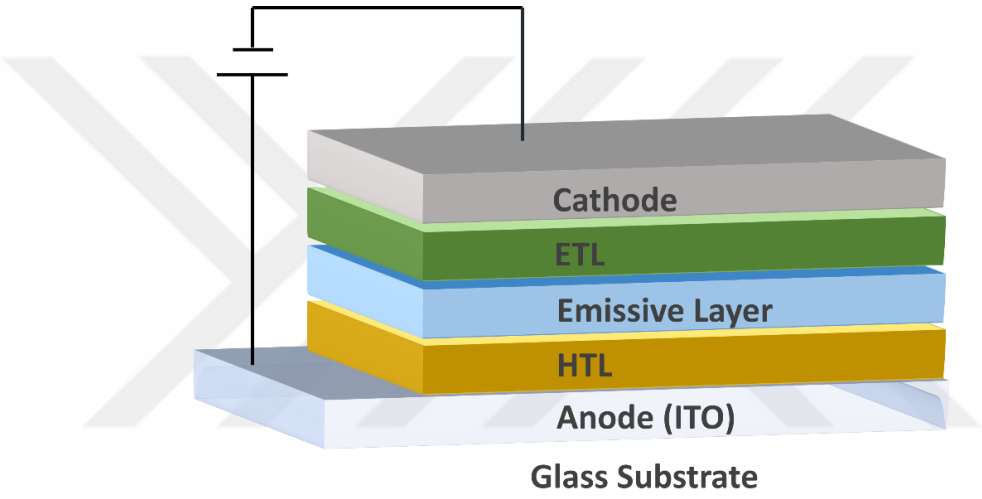

Figure 1.7. A conventional device architecture of OLED.

The Hole Transport Layer (HTL) is constructed on the top of the anode part of the structure. HTL is a crucial layer that supports the transport of holes from itself, enabling the holes to reach the Emissive Layer. The features of the anode, specifically the anode/hole transport layer (HTL) interface topography, have been shown to play a significant impact on the effectiveness, functionality, and lifetime of OLEDs in various experimental studies [41]. The Emissive Layer (EML), located above the HTL, is where the electrical energy is directly converted into light. As a composition of Emissive Layers, the small molecules and polymers are used as light-emitting materials. The Electron Transport Layer (ETL) is a layer enabling the transport of electrons from itself to the Emissive Layer [42]. On top of the ETL, the

LiF or Ca metal layer will be used to increase the stability and performance of the OLED devices. These are introduced to modify the electrode work function and the interfacial reactivity [43]. The cathode is a negatively charged counterpart of an OLED device, enabling the injection of electrons into the organic layers. In OLED devices, the efficiency and brightness depend on the work function. Due to its appropriate work function, Al metal is used as a cathode in combination with the LiF.

1.3.3 Important Parameters in OLED Performance Determination

Generally, current density-luminance versus voltage graphs, current efficiency versus voltage graphs, and electroluminescence spectra of OLED devices are provided to assess their performance.

Turn-on voltage (T_{on}) indicates the voltage at which the device first starts to emit light, and this value is recorded when a luminance of 1 cd/m² is achieved.

Current density is the current divided by the device area in the unit of $mA.cm^{-2}$. Current efficiency is calculated by using the current density and luminance values, and its formula is shown below;

$$\text{Current Efficiency (CE) } (cd.A^{-1}) = \frac{Luminance\ (cd.m^{-2})}{Current\ density\ (A.m^{-2})}$$

The EQE serves as a crucial parameter for assessing the effectiveness of devices in terms of converting current (electrical energy) into light. The EQE is calculated by comparing the quantity of output photons (produced by the OLED) to the quantity of injected electrons (electron supply facilitated through external voltage application).

In determining the color of light emitted by an OLED device, mostly Commission Internationale de l'éclairage (CIE) coordinates (x,y,z) are used. This standardizes the reporting of color values, ensuring a universal understanding of the represented colors when these coordinates are provided.

1.3.4 Blue-light Emission Problem and Aim of The Study

Figure 1.8. Red, green, and blue color emitting OLEDs.

Since the initial demonstrations of OLEDs, scientists and technology firms have been investigating more efficient red, green, and blue light emitters with excellent color purity and stability. White light-emitting OLEDs (WOLEDs) have an essential role in the lighting and display industry. They consist of a combination of red, green, and blue light emissions, the three primary colors (R, G, B). For this reason, research and development on red, green, and blue organic light-emitting materials and their application to OLEDs are exciting subjects for researchers. As a result of research conducted so far, satisfactory results for color purity, stability, and efficiency were obtained for red and green light-emitting OLEDs [44]. However, there are several drawbacks in the case of blue light-emitting materials regarding color purity, luminescence efficiency, and device endurance. Compared to green and red light-emitting OLEDs, blue light-emitting OLEDs have a significant disadvantage: the intrinsic wide-band-gap nature of deep-blue emitters [45]. In contrast to red light emission, a longer band gap between the Highest Occupied Molecular Orbital (HOMO) and Lowest Unoccupied Molecular Orbital (LUMO) levels of emissive material is needed to emit light at a shorter wavelength for blue light emission. Due

to the long bandgap of blue light-emitting materials, problems such as high charge injection barrier, unstable charge injection, and transportation emerge. To solve these problems, scientists are working to obtain pure, bright, and stable blue color emissions. Although one of the most essential requirements for electroluminescent devices is the device lifetime, studies of highly efficient deep-blue emitting materials with adequate device lifetime are still limited.

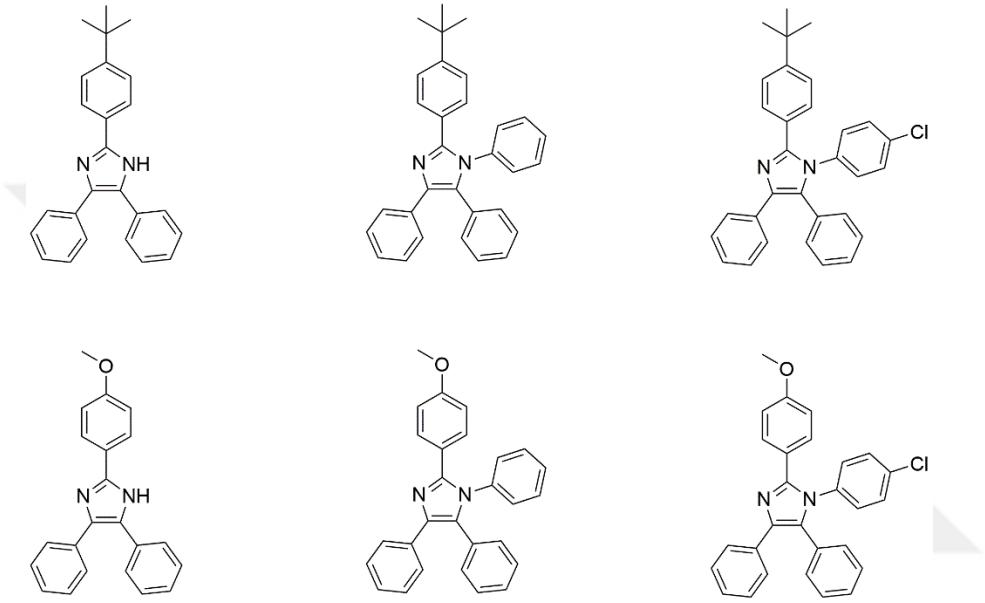

Figure 1.9. Synthesized imidazole derivatives

In this study, the effects of different substituents added to the imidazole molecule on device applications and their impact on color properties were investigated. Figure 1.9 shows the molecules synthesized and applied in devices for this purpose.

The first three molecules include tertiary-butyl substituents, and the second three molecules include methoxy substituents. In addition to that, these molecules are varied by changing the substituent in the N3 position in the imidazole core unit.

CHAPTER 2

EXPERIMENTAL

2.1 Materials, Equipment, and Methods

The materials used in the synthesis, including benzil, 4-(*tert*-butyl)benzaldehyde, 4-methoxybenzaldehyde, ammonium acetate, aniline, and 4-chloroaniline, were supplied by Sigma Aldrich Company. Acetic acid was provided by Carlo Erba Reagents GmbH as a solvent in the reactions. The synthesis took place in an open-air environment under reflux conditions at 60°C. Structures of molecules were verified using a Bruker Spectrospin Avance DPX-400 Nuclear Magnetic Resonance Spectroscopy (NMR) instrument in the chemistry department, with trimethyl silane (TMS) as a reference material, and all the molecules were dissolved in deuterated dimethyl sulfoxide for the analysis. Moreover, a high-resolution mass spectrometry (HRMS) analysis was conducted using a Water SYNAPT G1 MS device in the METU Central Laboratory to verify the materials.

Jasco V-770 double-beam UV-Visible/ NIR Spectrophotometer and PerkinElmer Fluorescence Spectrometer LS 55 instrument were used for molecular characterizations. Moreover, electrochemical studies were conducted for another molecular characterization technique by investigating cyclic voltammograms (CV) of materials in Gamry Instruments Reference 3000 Potentiostat.

ITO-coated glass substrates purchased from VisionTek Systems were used as anode contact in the device fabrication part of the study. During the OLED fabrication process, TPBi and α-NPD were purchased from Lumtec. The cathode contact was made using lithium fluoride (LiF), aluminum (Al), and silver, all procured from the Kurt J. Lesker Company. The materials were evaporated in vacuum chambers from

NANOVAK and mBraun. For the organic small molecule evaporation, boron nitride crucibles from NANOVAK were used.

2.2 Synthesis of the Imidazole Derivatives

In this study, all the imidazole derivatives were synthesized by following the Radziszewski reaction [46]. Imidazole molecules are produced through the synthesis involving a condensation reaction between 1,2-dicarbonyl derivative, ammonia, and aldehyde derivatives.

2.2.1 Synthesis of 2-(4-(*tert*-butyl)phenyl)-4,5-diphenyl-1H-imidazole (BIm-H-*t*Bu)

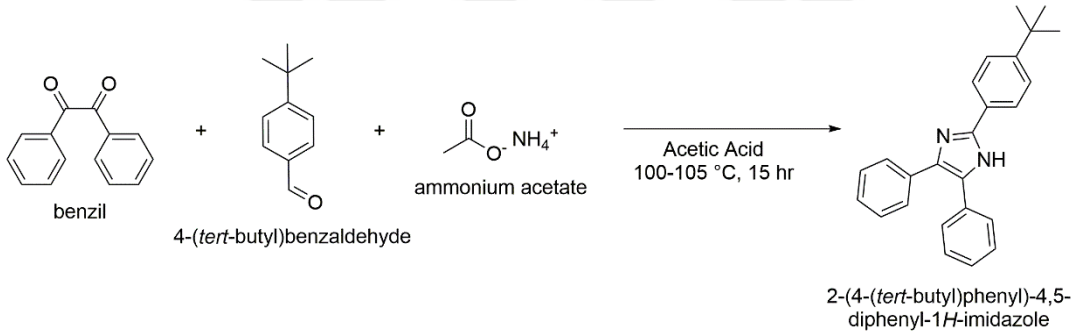

Figure 2.1. Reaction scheme of the synthesis of BIm-H-*t*Bu

The synthesis of molecule BIm-H-*t*Bu is outlined in Figure 2.1. Benzil (1 equivalent), 4-(*tert*-butyl)benzaldehyde (1 equivalent), and ammonium acetate (6 equivalents) were dissolved in glacial acetic acid and stirred at 100°C overnight. The progress of the reaction was monitored by thin-layer chromatography (TLC). After completion, the reaction mixture was allowed to cool and poured into ice for precipitation, followed by washing with distilled water. The resulting precipitate was filtered and dried.

For purification, the dried solid was dissolved in a mixture of ethanol (EtOH) and tetrahydrofuran (THF) with heating, and the solution was left to crystallize. The

formed crystals were filtered, and the filtrate was dried. The purified product was characterized by using NMR and HRMS techniques before further use.

^{1}H NMR (400 MHz, DMSO-d_6) δ 12.64 (s, 1H), 8.01 (d, J = 8.5 Hz, 2H), 7.54 (d, J = 7.7 Hz, 2H), 7.50 (d, J = 8.4 Hz, 4H), 7.45 (t, J = 7.4 Hz, 2H), 7.38 (d, J = 7.1 Hz, 1H), 7.30 (t, J = 7.5 Hz, 2H), 7.23 (d, J = 7.3 Hz, 1H), 1.32 (s, 9H).

HRMS analysis provided the mass of compound BIm-H-tBu ($C_{25}H_{24}N_2$) as 353.2018, which is calculated as 353.2018.

2.2.2 Synthesis of 2-(4-(*tert*-butyl)phenyl)-1,4,5-triphenyl-1H-imidazole) (BIm-Ph-*t*Bu)

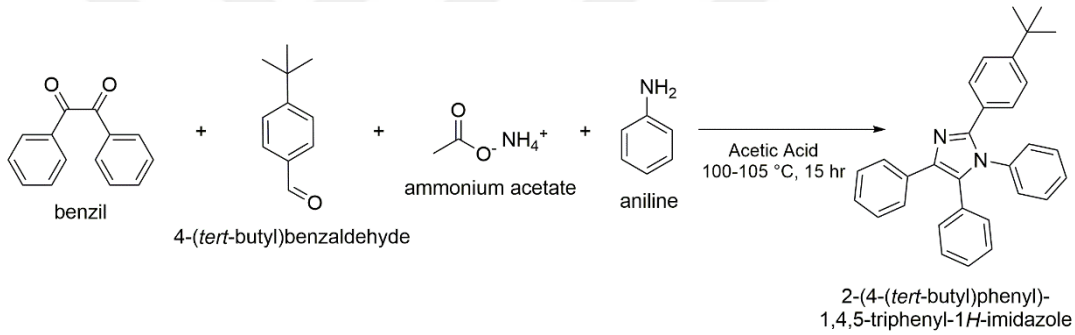

Figure 2.2. Reaction scheme of the synthesis of BIm-Ph-*t*Bu

The synthetic pathway of BIm-Ph-*t*Bu is shown in Figure 2.2. A mixture of Benzil (1 equivalent), 4-(*tert*-butyl)benzaldehyde (1 equivalent), ammonium acetate (10 equivalents), and aniline (4 equivalents) and acetic acid was put in a round bottom flask and heated at 100°C overnight. The formation of the new molecule was monitored using TLC.

Once the reaction was complete, the solution was poured into a beaker containing ice to cause precipitation. The resulting precipitate was then filtered using filter paper. The filtrate was washed with distilled water to eliminate the acetic acid solvent.

The solid product was dried and then purified by dissolving it in EtOH with heating to get rid of impurities and excess reactants. The solution was allowed to cool to induce crystallization. The crystals were then filtered using gravitational filtration and characterized by NMR and HRMS.

^{1}H NMR (400 MHz, DMSO-d_6) δ 7.49 (d, J = 7.3 Hz, 2H), 7.36 – 7.16 (m, 17H), 1.23 (s, 9H).

^{13}C NMR (100 MHz, DMSO) δ 150.8, 146.5, 145.9, 136.7, 136.7, 134.4, 131.1, 131.1, 130.4, 129.1, 128.8, 128.4, 128.3, 128.1, 127.8, 127.5, 126.4, 126.3, 124.9, 34.3, 30.9.

HRMS analysis provided the mass of compound BIm-Ph-*t*Bu ($C_{31}H_{28}N_2$) as 429.2331, which is calculated as 429.2331.

2.2.3 Synthesis of 2-(4-(*tert*-butyl)phenyl)-1-(4-chlorophenyl)-4,5-diphenyl-1H-imidazole (BIm-PhCl-*t*Bu)

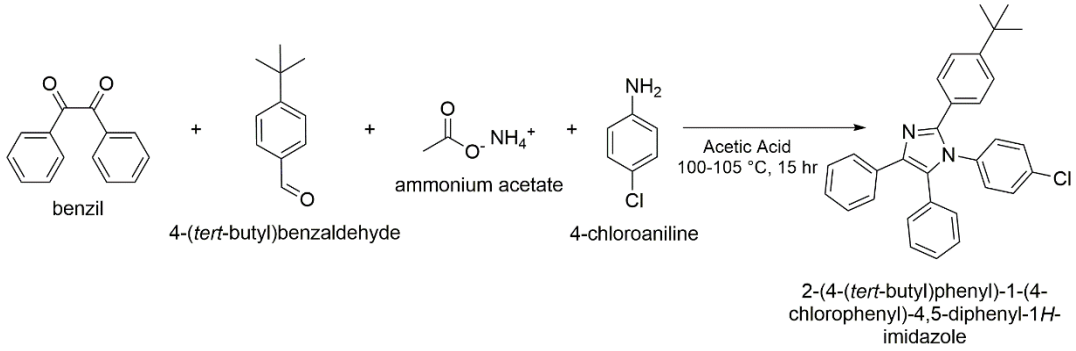

Figure 2.3. Reaction scheme of the synthesis of BIm-PhCl-*t*Bu

The synthesis of BIm-PhCl-*t*Bu is illustrated in Figure 2.3. Benzil (1 equivalent), 4-(tert-butyl)benzaldehyde (1 equivalent), ammonium acetate (10 equivalents), and 4-chloroaniline (4 equivalents) were dissolved in glacial acetic acid and reacted at 100°C overnight. The reaction mixture was then allowed to cool to room temperature before being poured onto ice to induce precipitation.

The resulting precipitates were filtered and washed with distilled water. After drying to remove residual water, the product was dissolved in a mixture of EtOH and THF by heating for crystallization. The solution was then left to crystallize.

The formed crystals were filtered using gravitational filtration and allowed to dry. The presence of the target product was confirmed by analyzing the NMR spectrum HRMS.

^{1}H NMR (400 MHz, DMSO-d_6) δ 7.59 – 7.10 (m, 18H), 1.25 (s, 9H).

^{13}C NMR (100 MHz, $CDCl_3$) δ 151.7, 147.1, 134.2, 131.2, 130.5, 129.8, 129.5, 128.7, 128.6, 128.3, 128.3, 127.5, 126.8, 125.4, 34.8, 31.3.

HRMS analysis provided the mass of compound BIm-Ph-*t*Bu ($C_{31}H_{27}ClN_2$) as 463.1941, which is calculated as 463.1941.

2.2.4 Synthesis of 2-(4-methoxyphenyl)-4,5-diphenyl-1H-imidazole (BIm-H-OMe)

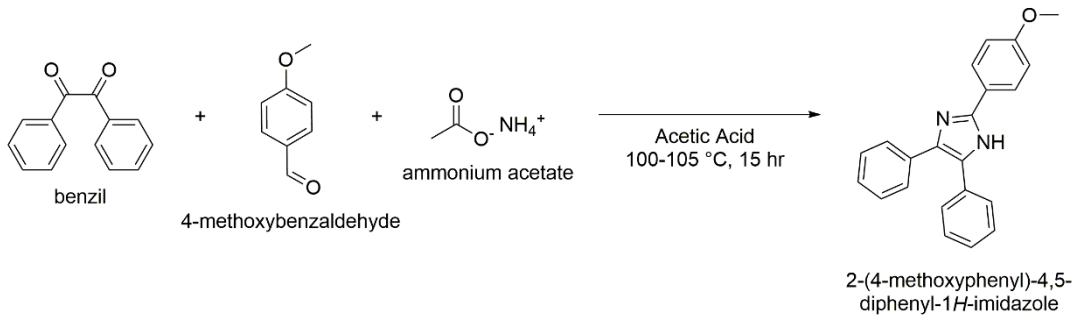

Figure 2.4. Reaction scheme of the synthesis of BIm-H-OMe

The synthetic route for BIm-H-OMe is illustrated in Figure 2.4. Benzil (1 equivalent), 4-methoxy benzaldehyde (1 equivalent), and ammonium acetate (6 equivalents) were dissolved in approximately 25 mL of glacial acetic acid in a round-bottom flask equipped with a reflux condenser and placed in an oil bath. The reaction mixture was refluxed at 100°C overnight, with the progress monitored by TLC.

After completion, the flask was removed from the oil bath and cooled to room temperature. The resulting product was poured into a beaker containing ice, and gravitational filtration was used to isolate the solid. The crude product was washed with distilled water and dried. The crude product was dissolved in the minimum amount of ethanol and tetrahydrofuran for crystallization, heated, and then cooled for crystallization. The white solid product was obtained after gravitational filtration.

NMR and HRMS characterizations were conducted to confirm whether the target molecule was obtained.

^{1}H NMR (400 MHz, DMSO-d_6) δ 12.53 (s, 1H), 8.03 (d, J = 8.8 Hz, 2H), 7.56 (d, J = 7.2 Hz, 2H), 7.50 (d, J = 7.2 Hz, 2H), 7.43 (dd, J = 8.4, 6.5 Hz, 2H), 7.36 (t, J = 7.2 Hz, 1H), 7.30 (dd, J = 8.4, 6.5 Hz, 2H), 7.21 (t, J = 7.3 Hz, 1H), 7.05 (d, J = 8.8 Hz, 2H), 3.81 (s, 1H).

^{13}C NMR (100 MHz, DMSO) δ 159.4, 145.6, 140.5, 136.7, 135.3, 131.2, 128.6, 128.3, 128.1, 127.6, 127.6, 127.0, 126.7, 126.4, 126.4, 123.1, 114.1, 55.2.

HRMS analysis provided the mass of compound BIm-Ph-*t*Bu ($C_{22}H_{18}N_2O$) as 327.1497, which is calculated as 327.1497.

2.2.5 Synthesis of 2-(4-methoxyphenyl)-1,4,5-triphenyl-1H-imidazole, BIm-Ph-OMe

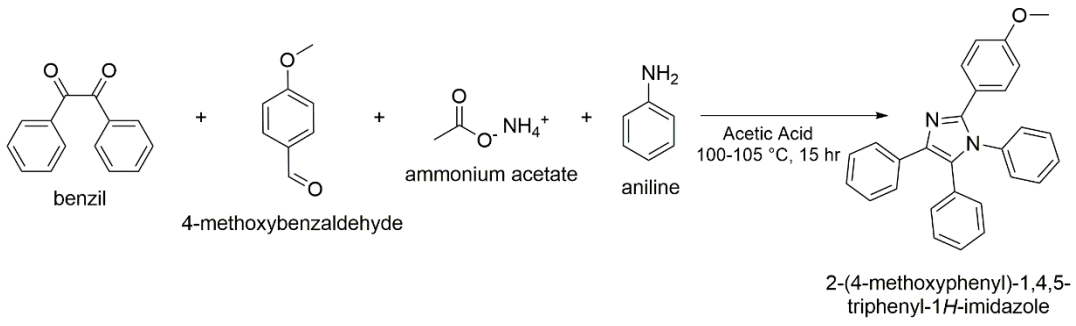

Figure 2.5. Reaction scheme of the synthesis of BIm-Ph-OMe

The reaction scheme of the synthesis of BIm-Ph-OMe is shown in Figure 2.5. In a round-bottom flask equipped with a reflux condenser and placed in an oil bath, benzil (1 equivalent), 4-methoxybenzaldehyde (1 equivalent.), aniline (4 equivalents), and ammonium acetate (10 equivalents) were dissolved in approximately 30 mL of glacial acetic acid. The reaction mixture was refluxed at 105°C overnight, and TLC was used to monitor the reaction progress.

After completion, the flask was removed from the oil bath and cooled to room temperature. The reaction mixture was then poured into a 100 mL beaker filled with ice. Gravitational filtration was used to isolate the solid once the ice melted. The crude product was washed with distilled water and dried. The crude product was dissolved in the minimum amount of ethanol and tetrahydrofuran for crystallization. After heating and cooling, the substance became a white solid. The crude product was collected by gravitational filtration.

The analysis of NMR and HRMS was used to confirm the product.

^{1}H NMR (400 MHz, DMSO-d_6) δ 7.47 (d, J = 8.4 Hz, 2H), 7.36 – 7.27 (m, 8H), 7.27 – 7.20 (m, 6H), 7.17 (d, J = 7.7 Hz, 1H), 6.84 (d, J = 8.8 Hz, 2H), 3.72 (s, 3H).

^{13}C NMR (100 MHz, $CDCl_3$) δ 157.8, 145.1, 135.4, 129.3, 128.5, 127.3, 126.7, 126.5, 126.4, 126.3, 126.1, 125.6, 124.7, 111.7, 53.4.

HRMS analysis provided the mass of compound BIm-Ph-*t*Bu ($C_{28}H_{22}N_2O$) as 403.1810, which is calculated as 403.1810.

2.2.6 Synthesis of 1-(4-chlorophenyl)-2-(4-methoxyphenyl)-4,5-diphenyl-1H imidazole (BIm-PhCl-OMe)

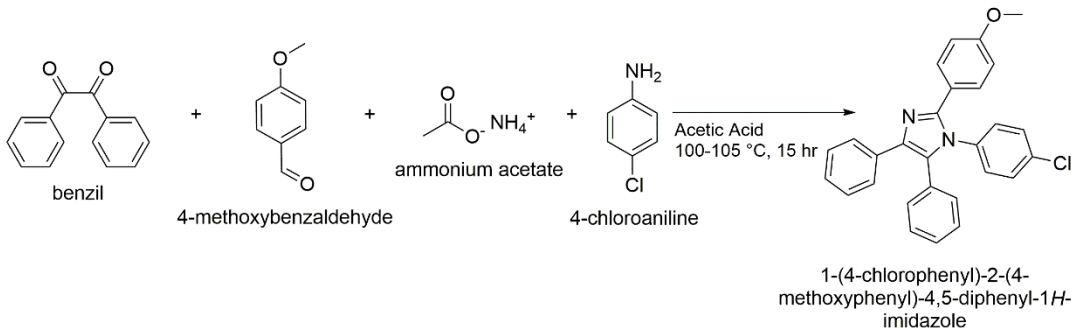

Figure 2.6. Reaction scheme of the synthesis of BIm-PhCl-OMe

The synthetic pathway of molecule BIm-PhCl-OMe is illustrated in Figure 2.4. In a round-bottom flask, benzil (1 equivalent), 4-methoxybenzaldehyde (1 equivalent), 4-chloroaniline (4 equivalents), and ammonium acetate (10 equivalents) were dissolved in approximately 30 mL of glacial acetic acid. The flask was equipped with a reflux condenser and placed in an oil bath to maintain the reaction temperature. The mixture was refluxed at 105 °C overnight, and TLC was used to monitor the reaction progress.

After reaction completion, the flask was removed from the oil bath and cooled to room temperature. The reaction mixture was then poured into a beaker containing 100 mL of ice. Gravitational filtration was used to isolate the solid once the ice melted. The crude product was washed with distilled water and dried. The crude product was dissolved in the minimum amount of ethanol and tetrahydrofuran for crystallization. After heating and cooling, the product became a white solid. The crude product was collected by gravitational filtration.

The presence of the target product was confirmed by analyzing the NMR spectrum HRMS.

^{1}H NMR (400 MHz, DMSO-d_6) δ 7.47 (d, J = 7.5 Hz, 2H), 7.40 (d, J = 8.5 Hz, 2H), 7.35 – 7.29 (m, 6H), 7.28 – 7.20 (m, 5H), 7.17 (t, J = 7.3 Hz, 1H), 6.89 (d, J = 8.7 Hz, 2H), 3.74 (s, 3H).

^{13}C NMR (100 MHz, $CDCl_3$) δ 159.9, 147.0, 135.8, 134.2, 131.2, 130.5, 130.4, 129.8, 129.5, 128.7, 128.3, 128.3, 127.5, 126.8, 113.8, 77.5, 55.4.

HRMS analysis provided the mass of compound BIm-Ph-*t*Bu ($C_{28}H_{21}ClN_2O$) as 437.1421, which is calculated as 437.1421.

2.3 Characterizations of the Imidazole Derivatives

2.3.1 Ultraviolet-Visible (UV-Vis) Spectroscopy

UV-Vis spectroscopy is a type of spectroscopic technique that measures the absorption properties of the molecules under radiation in the range of ultraviolet and visible regions in the spectrum. Absorption of the UV-visible radiation results in the excitation of the electrons from lower to higher energy levels. This study uses this measurement to obtain the optical band gap and maximum absorption wavelength. For the UV-Vis experiments, both thin film and solution forms of the molecules were used. Organic semiconductor molecules can have photoactive and electroactive properties thanks to their π-conjugation systems [47]. Those molecules absorb the light, and they are activated photonically. The absorption at the highest wavelength that corresponds to the lowest energy that molecule is able to absorb equals its band gap, which is the energy difference between the highest occupied molecular orbital (HOMO) and the lowest unoccupied molecular orbital (LUMO) [48]. Also, by using the $\lambda_{maxonset}$ value, corresponding to the lowest energy that the molecule absorbed of the UV-Vis spectra, the optical band gap of the material can be calculated by using the "$E^o = \frac{h \times c}{\lambda}$" formula where E^o represents the band gap energy, h is Plank's constant (6.626×10^{-34} J.s), c is the speed of light (2.998×10^{8} m.s^{-1}), and λ is the $\lambda_{maxonset}$ value from UV-Vis spectrum.

2.3.2 Electrochemical Studies

The electrochemical properties of the synthesized molecules were investigated by the cyclic voltammetric (CV) analysis. CV is a method for characterization in which the voltage is alternated between two values at a specific scan rate to examine the reduction and oxidation properties of materials. The synthesized six molecules were dissolved in dichloromethane (DCM). Then, they were coated onto an ITO-coated glass substrate via drop-casting. During the electrochemical studies, a three-electrode system, which consists of a counter, a working, and a reference electrode, was used. ITO, silver (Ag), and platinum (Pt) electrodes comprise the working, reference, and counter electrodes, respectively. The 0.1 M supporting electrolyte was prepared using tetrabutylammonium hexafluorophosphate ($TBAPF_6$) in acetonitrile (ACN). Cyclic voltammograms were monitored by adjusting the scan rate to 1.5 V for n-doping and -1.7 V for p-doping. Also, the scan rate of all cycles was set to 100 $mV.s^{-1}$. By using the oxidation and reduction potential data obtained from the cyclic voltammograms were used to calculate the HOMO and LUMO levels of the molecules.

2.3.3 Photoluminescence Spectroscopy

Photoluminescence spectroscopy studies were conducted to determine the light emission properties of molecules in both solution and solid-state form. Further investigation was employed to determine their emission properties if they perform light emission. The concept of photoluminescence spectroscopy is based on the excitation of a molecule from its ground electronic state to an excited electronic state by photons coming from a light source followed by returning to its original state via the emission of light without any destroying the molecule. Based on the UV-Vis spectrums, the excitation wavelength of the experiment was determined. Then, the scan was started 10nm ahead of the excitation wavelength, and the scan rate was adjusted to 300 nm/s.

The photoluminescence quantum yields of the six molecules were determined by following the below procedure:

- Firstly, a reference material that has a compatible emission wavelength with the molecule, quinine sulfate, was chosen.
- Then, the solution of this material was prepared with sulfuric acid, and UV-Vis spectra were recorded to give absorption intensities in the range of 0.01-0.1. Absorption and emission spectra were collected for each different concentration.
- After that, a linear graph was plotted using the emission spectrum area and the absorption intensities, and the slope of this graph was obtained. For the results to be reliable, the R^2-value must be 0.99.
- The same processes were applied to the other six molecules.
- As the quantum yield of quinine sulfate is known, the slopes of the graphs obtained from the other molecules were compared to that of quinine sulfate. Using quinine sulfate as a reference, the PLQY values of the imidazole derivatives were calculated in this manner.

2.3.4 Theoretical Calculations

This section of this thesis was performed by Assist. Prof. Dr. Erol Yıldırım and Phd student Tuğba Hacıefendioğlu. All calculations were performed at the level of B3LYP/6–311+g(d,p) basis sets using the Jaguar package as implemented in the Schrödinger Material Science Suite [49,50]. Geometry optimizations were initiated from different initial structures by controlling the torsional angle between connected units of six molecules to achieve the lowest energy geometry. Electrostatic potential surface (ESP) and frontier molecular orbital surfaces (HOMO and LUMO) were determined and mapped onto the six molecules using Gaussview. Intrinsic properties of optimized molecular geometries were computed DFT in an automated fashion using the Optoelectronics calculation module in the Schrödinger Material Science Suite. Oxidation and reduction potential (Eox and Ered) were obtained with

Koopmans approximations, taking the value of orbital energy to be the HOMO energy from the neutral molecule for E^{ox} and the LUMO energy for the reduction potential. Marcus theory inner sphere reorganization energies for holes and electrons (λ_{hole} and ($\lambda_{electron}$) are the sum of the energy for the neutral molecule to relax from the ion geometry to the neutral geometry and the energy for the ion to relax from the neutral geometry to the ion geometry. Adiabatic and vertical ionization energy (AIE and VIE) for electron and hole were calculated by the energy difference between the neutral molecule and its anionic/cationic form, respectively.

2.4 Device Fabrication

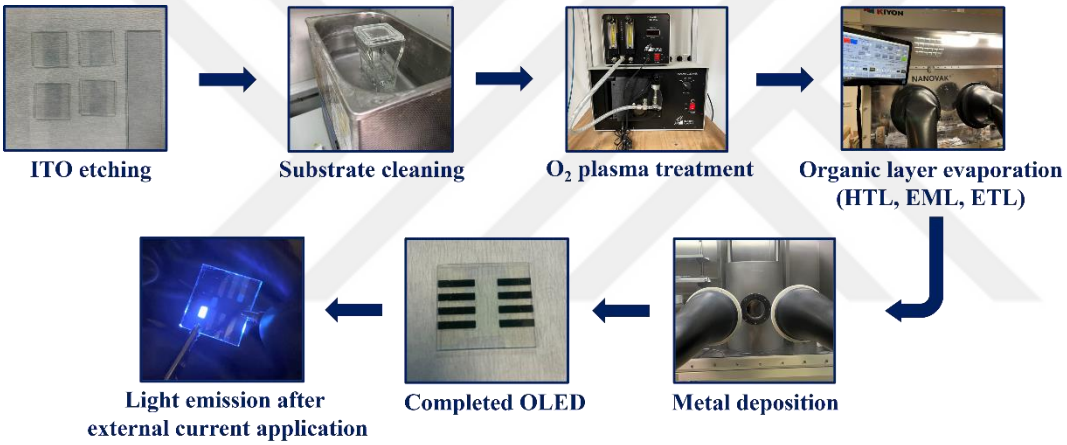

Figure 2.7. Schematic illustration of OLED device fabrication.

2.4.1 ITO Etching and Cleaning

ITO-coated glass substrates supplied by VisionTek were etched using zinc powder and 7.3 M HCl solution to minimize the defects on the device area. Firstly, the ITO-coated glass strips were taped 2.5 cm in width from the middle. Then, zinc powder was sprinkled on the exposed edges. After that, the diluted HCl solution was dropped to the edges. A redox reaction occurred between them, and ITO on the edges was removed. After removal of the tape, the strips were cleaned with distilled water and acetone. Then, the strips were cut at 2.5 cm intervals. The ITO-coated glass

substrates (2.5 cm×2.5 cm) were cleaned firstly by Hellmanex detergent for 15 minutes in an ultrasonic bath. It was followed by distilled water, acetone, and isopropyl alcohol for 15 minutes individually in an ultrasonic bath. When the cleaning process ends, the substrates are ready to use.

2.4.2 Oxygen Plasma Treatment

Before oxygen (O_2) plasma treatment, the substrates were dried by a nitrogen gas gun. Then, they were placed into a petri dish with the ITO-coated surface up (the electrically conductive ITO side of the substrates was checked by a multimeter). After that, they were put into the O_2 plasma instruments. After the plasma was formed, substrates were treated with O_2 plasma for 15 minutes, which is an optimized time to enhance the work function (φ) of ITO compatible with the HOMO level of alpha-NPD (α-NPD) [51]. The reason behind this treatment is to improve the device efficiency by reducing the Fermi Level of the ITO and cleaning the surface[52–54]. This oxidative treatment helps remove the organic impurities on the ITO surface and increases its wettability. Moreover, increasing the work function of the ITO (anode contact) decreases the energy barrier between the α-NPD as HTL to make easy the hole injection process.

2.4.3 Organic Small Molecule Deposition Inside Vacuum Evaporator

The materials used in the hole transport, emissive, and electron transport layers comprised organic molecules. Different than organic polymers, organic small molecules can be evaporated inside the vacuum system due to their low melting temperature. All the organic layer deposition processes proceeded in a vacuum evaporator system inside nitrogen-filled glove box systems. The materials that were going to be evaporated were put in boron nitride crucibles. Then, by applying heat to the crucibles under a vacuum environment of around 10^{-7} Torr, organic layers

were evaporated onto the substrates that were taped on a mask at a consistent rate of around 0.4 Å.s^{-1}.

2.4.4 Metal Contact Deposition Inside Vacuum Evaporator

Cathode metals were deposited on ETL in a vacuum evaporator system inside nitrogen atmosphere glove box systems. When the pressure of the system decreases to 10-7 Torr and the system gives the "STABLE WATER ON" sign, metal deposition can be started. Firstly, 0.6 nm LiF (as a buffer layer) was deposited at the rate of the LiF adjusted to $\leq$ 0.1 Å.s^{-1}. Then, 100nm cathode metal, Al, was evaporated. The LiF/Al pair was deposited in the NANOVAK evaporation system, where the deposition was controlled by integrated computers in the evaporation systems. In the device architecture where calcium (Ca) metal was used, using the mBraun vacuum system and Inficon SQC-310 Thin Film Deposition Controller, Ca, and Al metals were deposited at 20 nm and 100 nm, respectively. In the Ca deposition, the first 10 nm evaporated without opening the substrate shutter to remove the oxidized Ca, and then 20 nm Ca was deposited onto the substrates at around 0.5 Å.s^{-1}.

2.5 Device Characterization

After the fabrication of OLED devices, they were characterized by using Ocean Optics Maya2000 Spectrometers, fiber optic cable and Ocean Optics Spectra Suit Software, and Kiethly2400 Source meter. By applying an external voltage, the current passing through the device and luminance values were recorded simultaneously. By using Ocean Optic Spectra Suit software, electroluminescence spectrums and color values of the devices were recorded using fiber optic cable to detect the light that was emitted from the device. After that, current density-luminescence vs. voltage, current efficiency vs voltage graphs, electroluminescence spectrums, and Commission Internationale de l'Éclairage, International Commission

on Illumination (CIE) diagrams of the color of light that devices emitted were generated.

CHAPTER 3

RESULTS AND DISCUSSION

3.1 Molecular Characterizations

3.1.1 Optical Studies

The optical studies of imidazole-based molecules were carried out using UV-Vis Spectroscopy, which has a detailed experimental explanation in Section 2.3.1. In Figure 3.2. and Figure 3.3., absorption spectra of all six molecules were shown in thin film and solution forms. By using the absorption peaks from the UV-Vis spectra, maximum absorption wavelengths (λ_{max}) (nm) and maximum absorption wavelength onset values (λ_{max}^{onset}) (nm) were obtained. By using the following formula, which is based on Plank's Law, the band gap energy (E_g^{op}) of molecules was calculated.

$$E_g^{op} = \frac{h \times c}{\lambda_{max}^{onset}} = \frac{1241}{\lambda_{max}^{onset}}$$

h and c are Plank's constant and speed of light, respectively. Due to the unit of E_g^{op} being eV, the multiplication of h and c, which gives the vacuum wavelength for a photon, is converted to eV, where the conversion factor is 1241. The absorption wavelength of a molecule is directly related to the band gap energy, which is the energy difference between HOMO and LUMO levels. The energy of the absorbed light equals the E_g^{op}. For synthesized imidazole molecules, λ_{max}, $\lambda_{max,onset}$, and E_g^{op} values were summarized in Table 3-1. and Table 3-2.

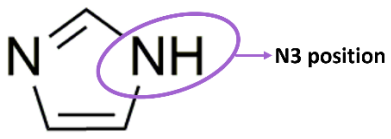

Figure 3.1. N3 position indicated imidazole core unit

It can be seen in the absorption spectrum of molecules containing phenyl and para-chlorophenyl substituent in the N3 position which is indicated in Figure 3.1. that there is a red-shift in their thin film concerning the solution forms in chloroform. The origin of this red shift is the π–π interactions and molecular aggregation in the solid state [55]. Because of the increase in the conjugation due to the molecular packing and π–π interactions, molecules shift to a lower energy state and, hence, to a longer wavelength. On the other hand, molecules BIm-H-tBu and BIm-H-OMe, which do not have any substituent in the N3 position, exhibit a blue shift in the UV-Vis spectrum. The molecular aggregation in a solid state results in H and J-type aggregation. J-aggregation is a molecular interaction in a head-to-tail manner. This type of aggregation causes energy splitting where the higher states are forbidden, and lower states are allowed optically. J-aggregates generally result in higher radiative decay rates, so higher fluorescence efficiency can be observed in this type of aggregation thanks to the lower excited energy states corresponding to the emission states. The fact that this aggregation improves fluorescence is an indication of the improvement in electroluminescence. In H-type aggregations, molecules are aligned side by side. Splitting to the higher energy level is due to the H-aggregation (blue-shift). The radiative decay at the lower energy level is forbidden, which culminates in feeble fluorescence so that it may withstand electroluminescence [56–59].

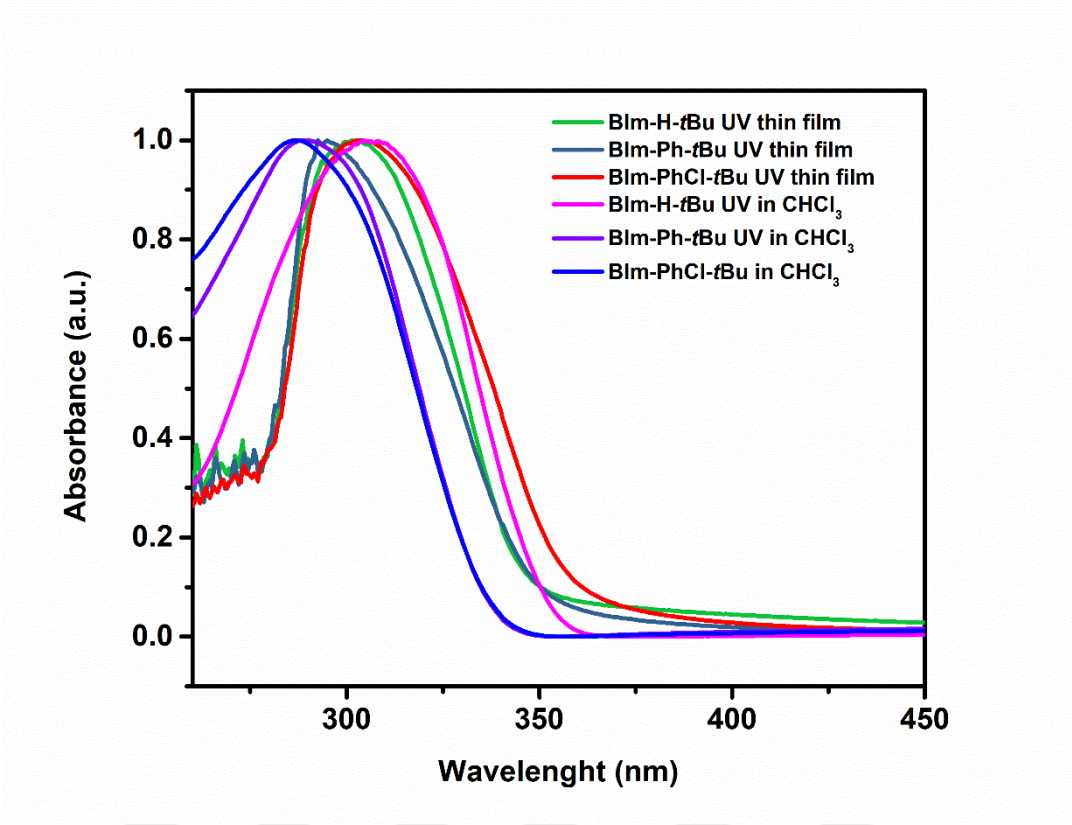

Figure 3.2. UV-Vis spectrum of molecules containing *tert*-butyl substituent in thin film and in solution forms

Table 3-1 Summary of the optical studies of BIm-H-*t*Bu, BIm-Ph-*t*Bu, and BIm-PhCl-*t*Bu

	$\lambda_{max,onset}$ (nm)	λ_{max} (nm)	Eg^{op} (eV)
BIm-H-*t*Bu	361	306	3.44
BIm-Ph-*t*Bu	351	289	3.54
BIm-PhCl-*t*Bu	355	285	3.54

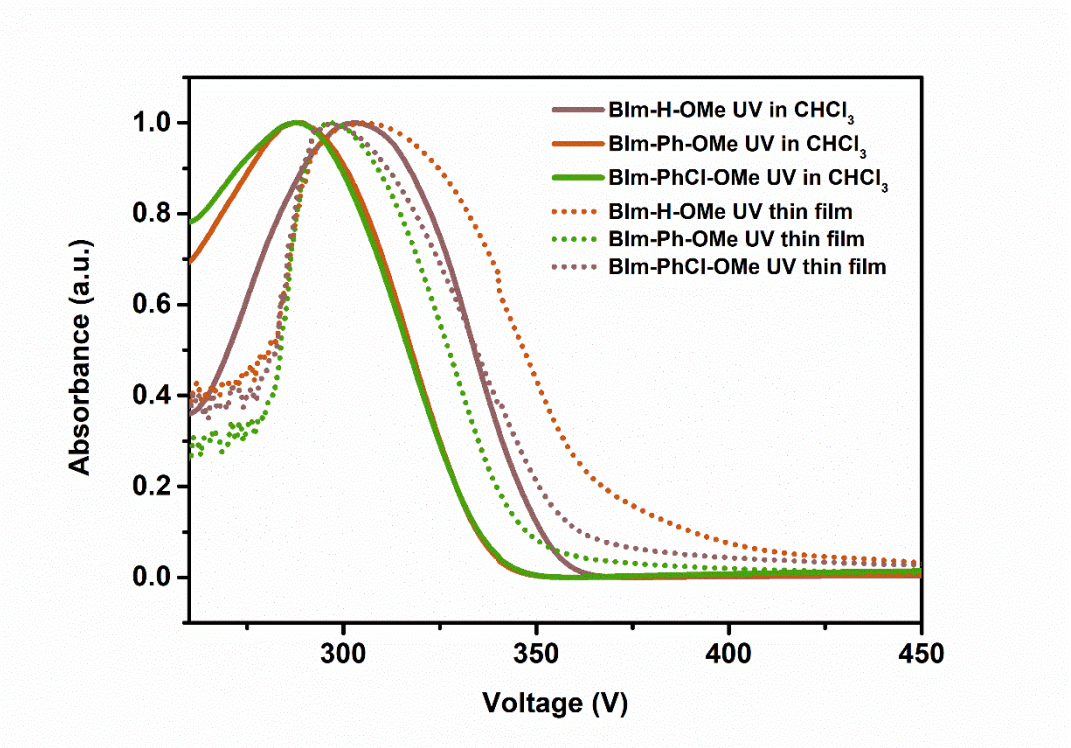

Figure 3.3. UV-Vis spectrum of molecules containing methoxy substituent in thin film and in solution forms

Table 3-2 Summary of the optical studies of BIm-H-OMe, BIm-Ph-OMe and BIm-PhCl-OMe

	$\lambda_{max,onset}$ (nm)	λ_{max} (nm)	Eg^{op} (eV)
BIm-H-OMe	378	302	3.28
BIm-Ph-OMe	350	287	3.55
BIm-PhCl-OMe	366	286	3.39

3.1.2 Photoluminescence Spectroscopy

The photoluminescence spectroscopies of all the molecules prove that those molecules can emit light in their solution and solid-state form. Molecules were excited at around their maximum absorption wavelength (290 nm). Then, their maximum photoluminescence is located at around 390 nm for their solution forms

and 490 nm for their thin film forms. The redshift (from a shorter to a longer wavelength) stems from the reason mentioned in Section 3.1.1.

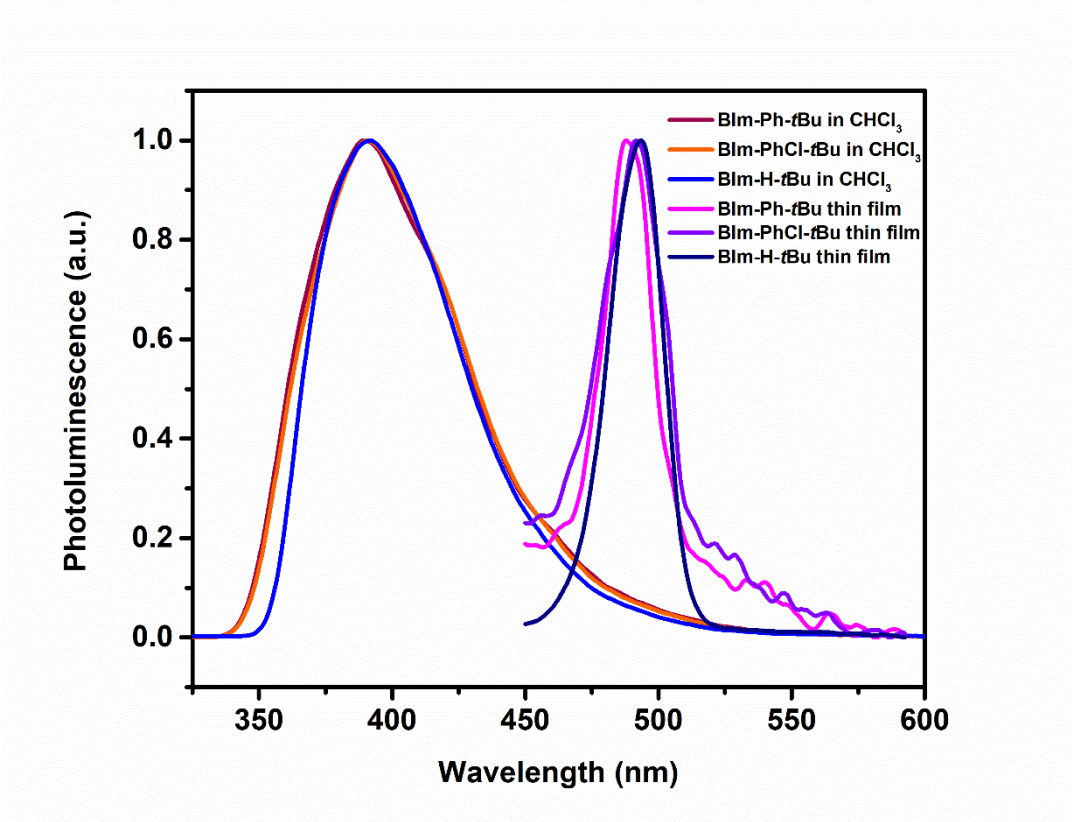

Figure 3.4. Photoluminescence spectrum of molecules containing *tert*-Butyl substituent in thin film and solution forms where they were excited at 290nm.

Table 3-3 List of maximum thin film and solution emission wavelengths and Stokes shifts of molecules containing *tert*-butyl substituent.

	$\lambda_{em,soln}$	$\lambda_{em,thinfilm}$	Stokes Shift (cm^{-1})
BIm-H-tBu	388	488	7038.71
BIm-Ph-tBu	389	491	8961.05
BIm-PhCl-tBu	391	494	9446.79

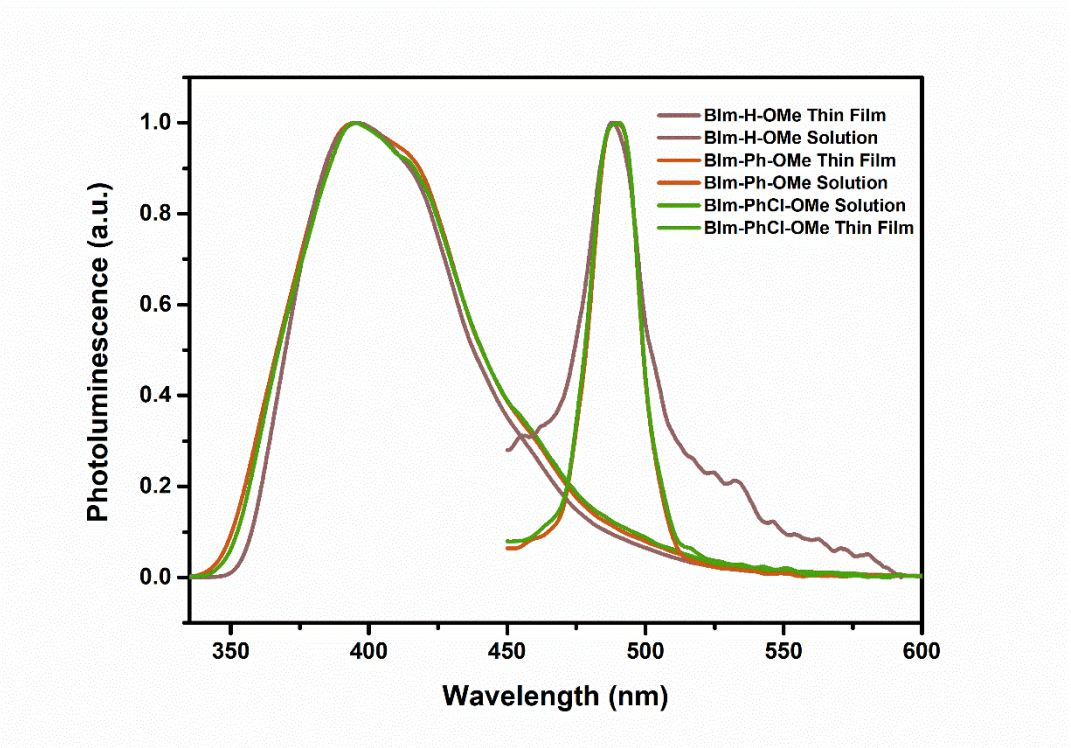

Figure 3.5. Photoluminescence spectrum of molecules containing methoxy substituent in thin film and solution forms where they were excited at 290nm.

Table 3-4 List of Stokes shifts of molecules containing methoxy substituent.

	$\lambda_{em,soln}$	$\lambda_{em,thinfilm}$	Stokes Shift (cm^{-1})
BIm-H-OMe	395	498	7796.13
BIm-Ph-OMe	394	498	9526.75
BIm-PhCl-OMe	395	499	9648.58

3.1.3 Photoluminescence Quantum Yield (PLQY) Calculation

According to the application note of Perkin Elmer, PLQY values of molecules were calculated by preparing the solutions of the molecules that give absorbance intensity between 0.01 and 0.1 [60]. Photoluminescent spectra of solutions with absorbance values of 0.01 and 0.1 for each molecule were taken. After that, the areas of these photoluminescent spectra were calculated. Then, the graph of absorbance intensity values versus the photoluminescent area was drawn, and best fits were taken for each

molecule. From the equation of the line, the slope of it was recorded. According to the dominant emission wavelength of molecules, a reference molecule, quinine sulfate (QS), was selected [61]. The same experimental procedure was applied to the QS under the same conditions as the imidazole molecules.

$$Q = Q_{ref} \times \left[\frac{m}{m_{ref}}\right]\left[\frac{n^2}{n_{ref}^2}\right]$$

According to the equation above, the PLQY values were calculated. Because the solvents used to solve QS and imidazole molecules differed, their square root of refractive indexes was multiplied. From Figure 3.6. to 3.12., photoluminescence area vs. absorbance intensities for QS and imidazole molecules were shown. Moreover, the results of PLQY are shown in Table 3-5. The highest PLQY values were achieved with the unsubstituted molecules in their N3 positions, corresponding to a value of around 37%. On the other hand, the lowest PLQY was observed with molecule BIm-PhCl-OMe with a corresponding value of 15%. Molecules containing phenyl substituent at the N3 position in imidazole core and BIm-Ph-*t*Bu resulted in around 25% quantum yield efficiency.

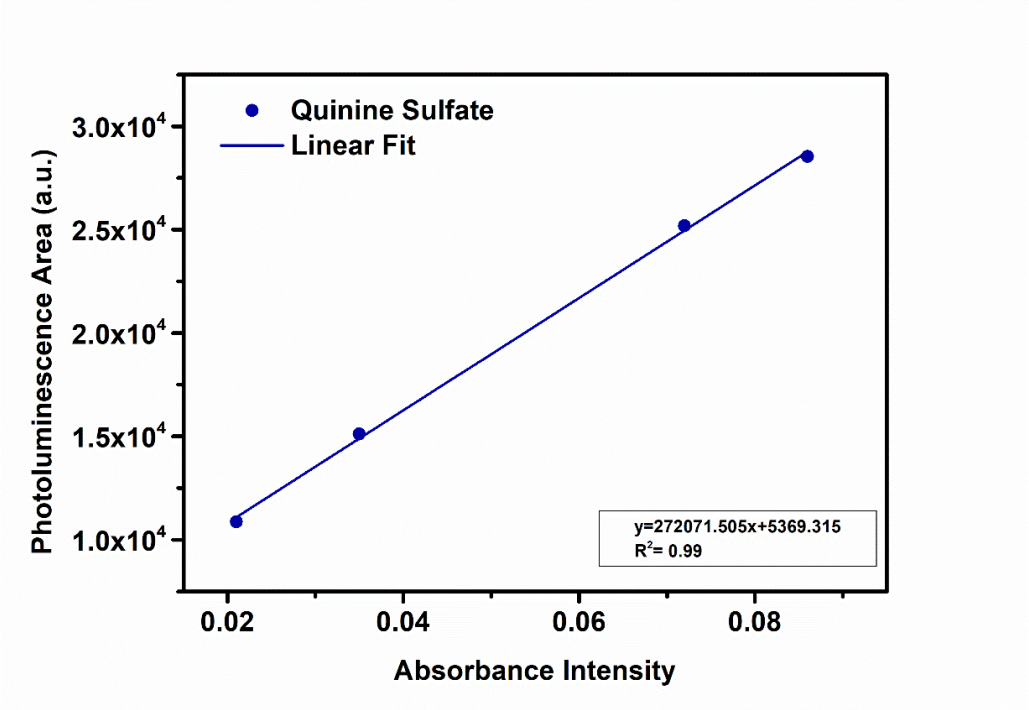

Figure 3.6. Photoluminescence area vs. absorbance intensity graph for quinine sulfate

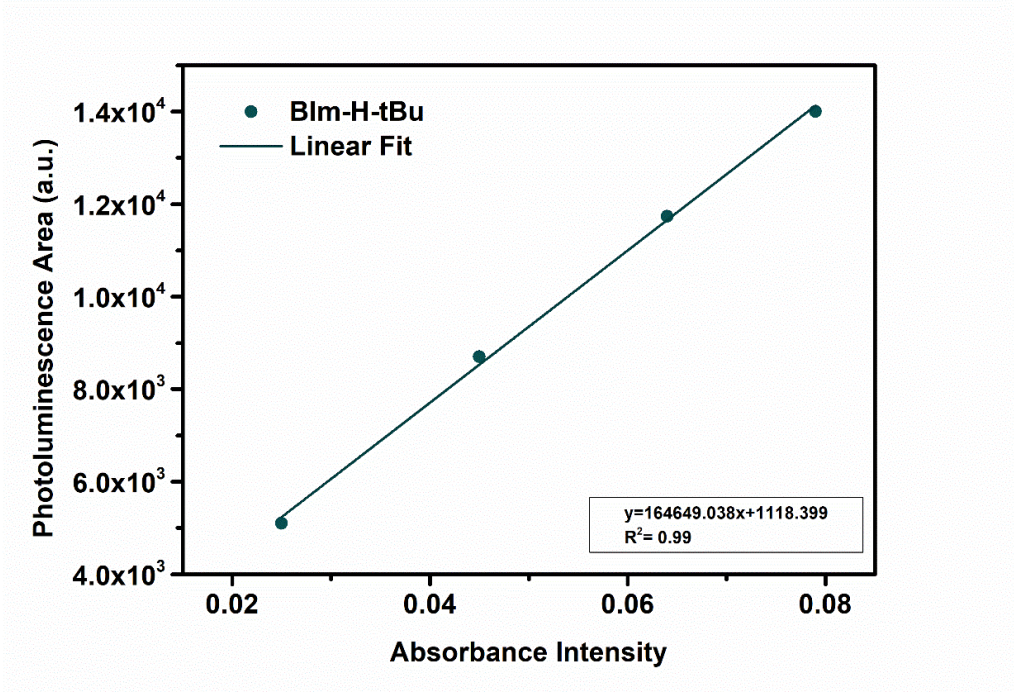

Figure 3.7. Photoluminescence area vs. absorbance intensity graph for BIm-H-*t*Bu

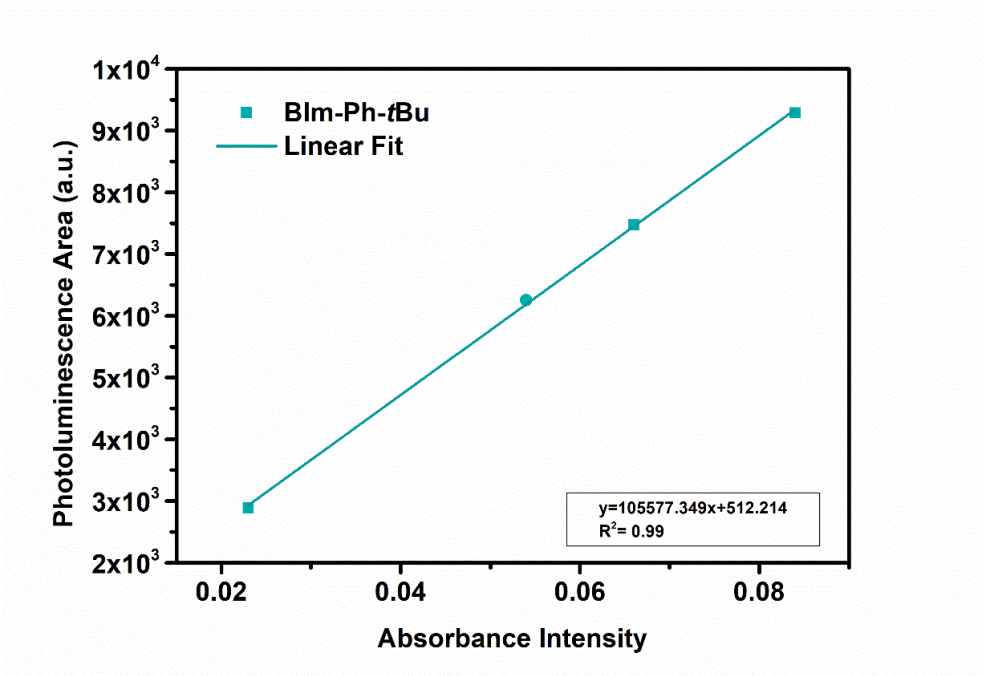

Figure 3.8. Photoluminescence area vs. absorbance intensity graph for BIm-Ph-*t*Bu

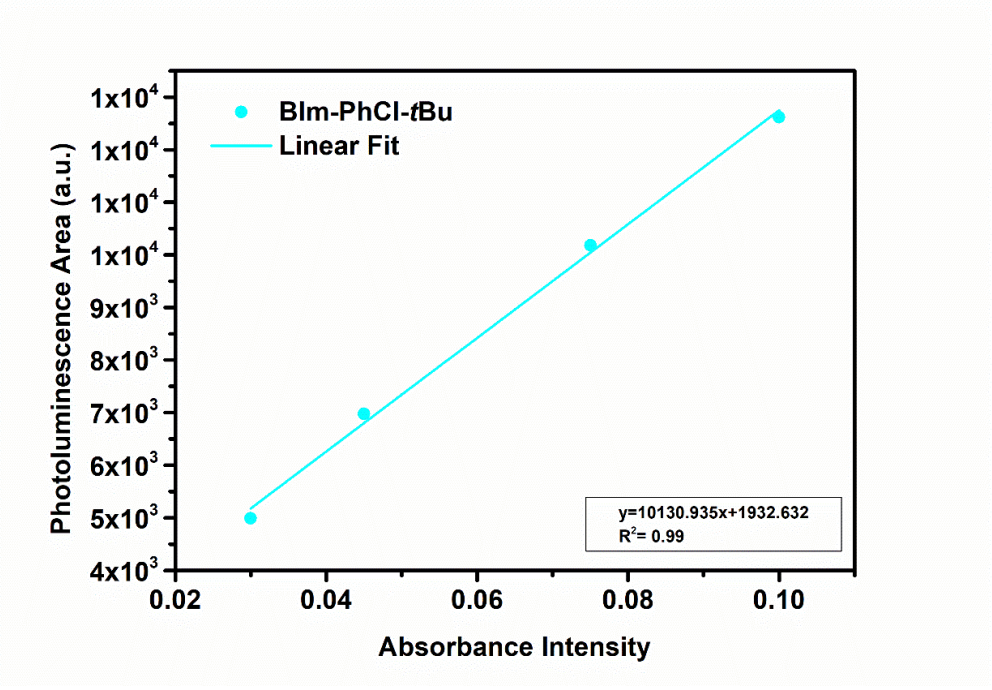

Figure 3.9. Photoluminescence area vs. absorbance intensity graph for BIm-PhCl-*t*Bu

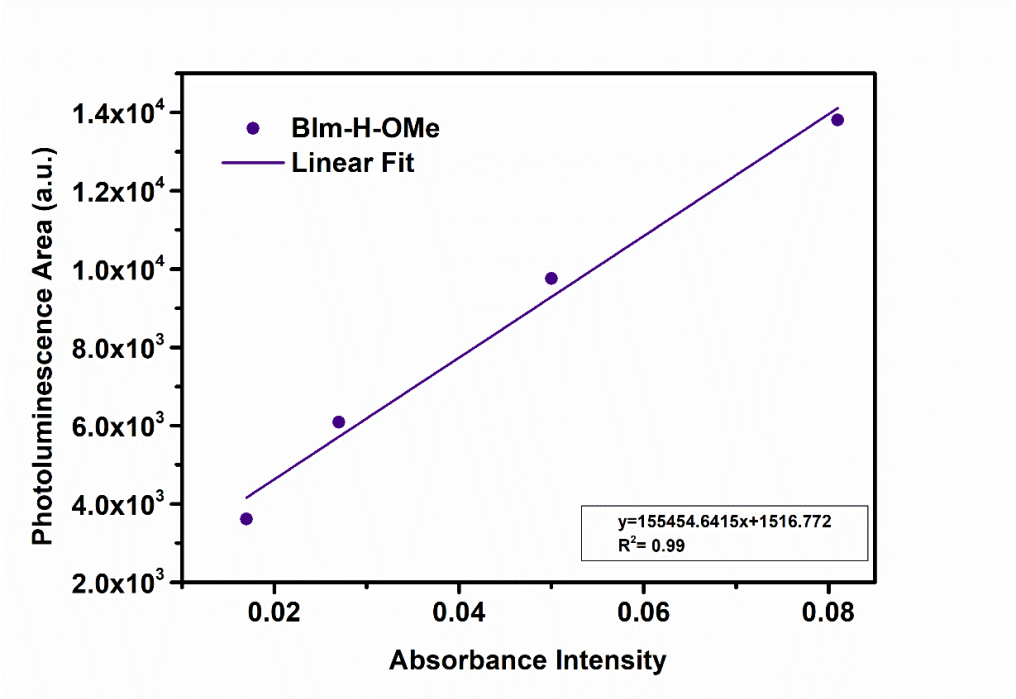

Figure 3.10. Photoluminescence area vs. absorbance intensity graph for BIm-H-OMe

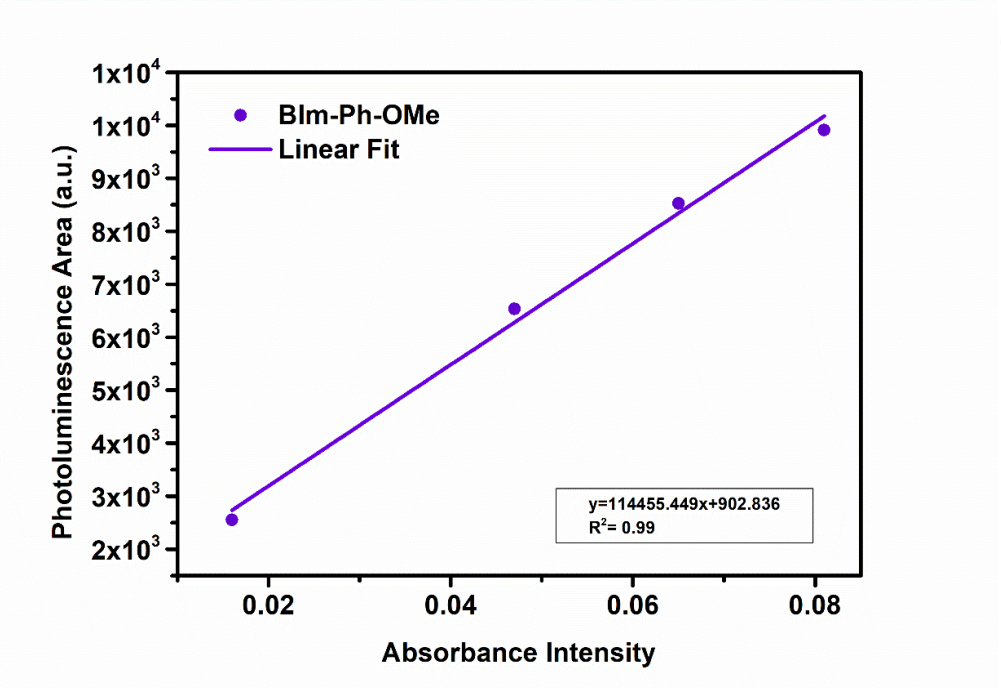

Figure 3.11. Photoluminescence area vs. absorbance intensity graph for BIm-Ph-OMe

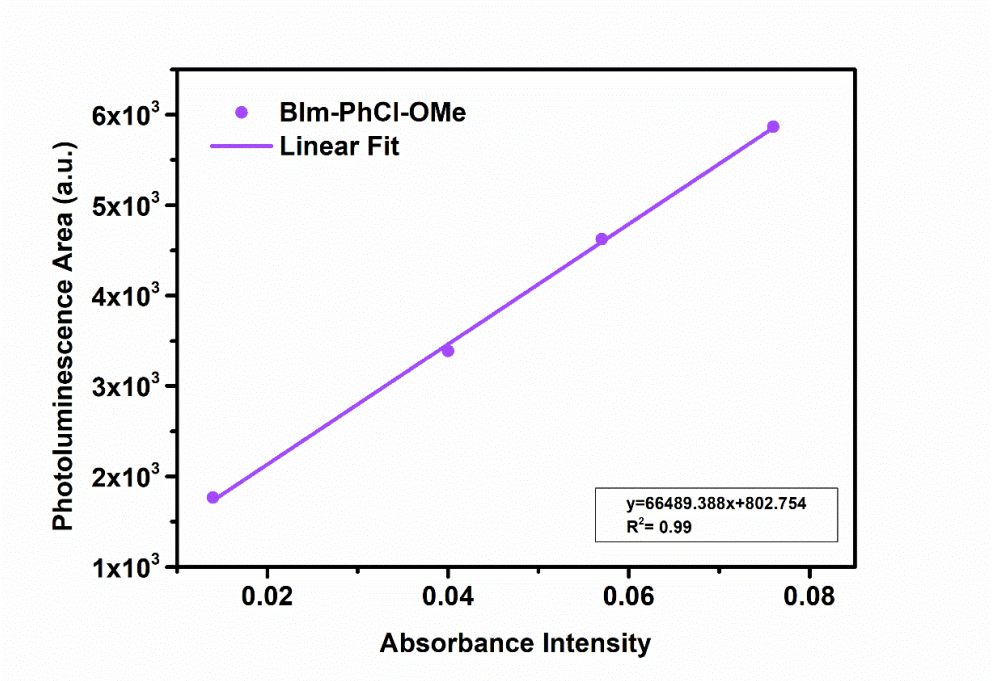

Figure 3.12. Photoluminescence area vs. absorbance intensity graph for BIm-PhCl-OMe

Table 3-5 Summary of PLQY values for all molecules

	BIm-H-*t*Bu	**BIm-Ph-*t*Bu**	**BIm-PhCl-*t*Bu**	**BIm-H-OMe**	**BIm-Ph-OMe**	**BIm-PhCl-OMe**
PLQY(%)	38	24	25	36	26	15

3.1.4 Electrochemical Studies

The experimental part of electrochemical studies of the synthesized molecules was explained in Section 2.3.2. The three-electrode system, which consists of a counter, a working, and a reference electrode, was used in this study. ITO, silver (Ag), and platinum (Pt) electrodes comprise the working, reference, and counter electrodes, respectively. The cyclic voltammograms and summary of electrochemical studies of the molecules containing tert-butyl substituent are shown in Figure 3.13. and Table 3-6, and the methoxy substituent is shown in Figure 3.14 and Table 3-7. As can be

seen in Figure 3.13. and 3.14., only the p-doping parts of the cyclic voltammograms are illustrated because the wide band gap of blue-emitting molecules results in deeper HOMO and lower LUMO levels. The working range of the working electrode, which is ITO, is between -2 V and +2 V. Due to the reduction potentials of the molecules exceeding the working limit of ITO, we cannot observe the n-doping of the molecules in their CVs.

By using the oxidation onset potential of molecules, their HOMO levels were calculated with the equation below;

$$HOMO = -(4.75 - E_{ox}^{onset})$$

Fe/Fe^{+} (ferrocene/ferrocenium) calibrated the Ag wire reference electrode. 4.75 constant comes from the HOMO level of ferrocene, which is actually 4.80, but it was adjusted by subtraction of 0.05, which is the half-wave potential of Fe/Fe^{+} [62–64].

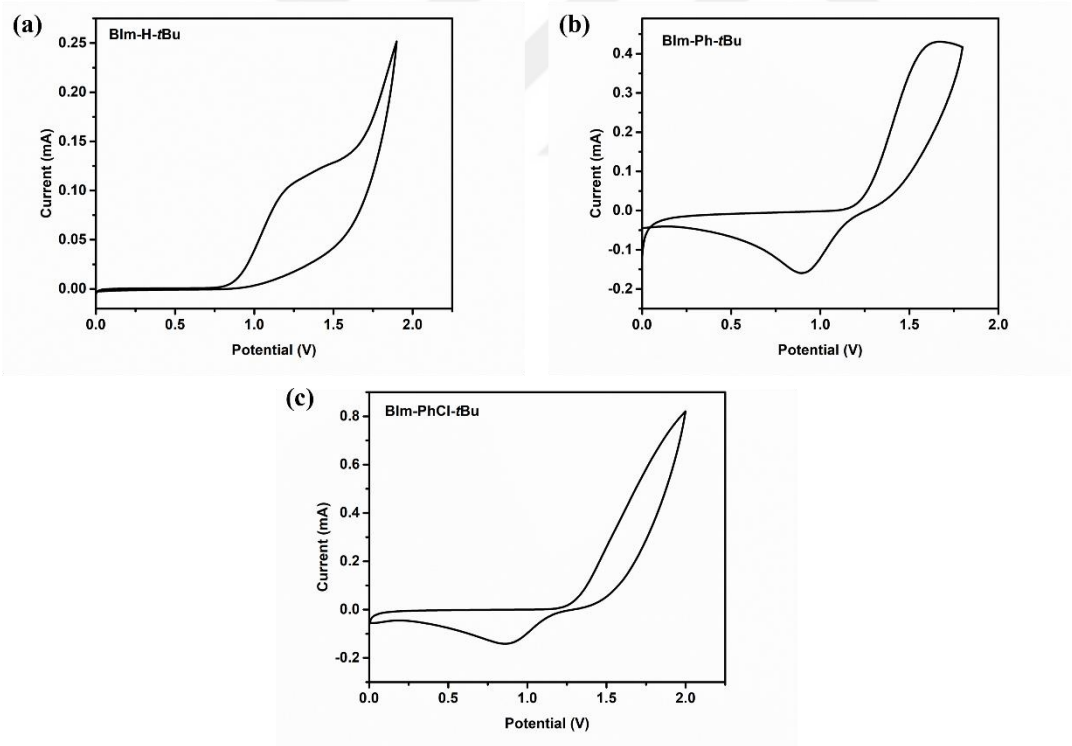

Figure 3.13. Cyclic voltammogram of molecules a) BIm-H-*t*Bu, b) BIm-Ph-*t*Bu, and c) BIm-PhCl-*t*Bu

Table 3-6 Summary of the electrochemical studies of BIm-H-*t*Bu, BIm-Ph-*t*Bu, and BIm-PhCl-*t*Bu

	E^{ox} (V)	E^{red} (V)	E^{ox}_{onset} (V)	E^{red}_{onset} (V)	HOMO (eV)	LUMO (eV)
BIm-H-*t*Bu	1.18	-	0.89	-	-5.64	-2.20
BIm-Ph-*t*Bu	1.62	-	1.25	-	-6.0	-2.46
BIm-PhCl-*t*Bu	1.85	-	1.29	-	-6.04	-2.50

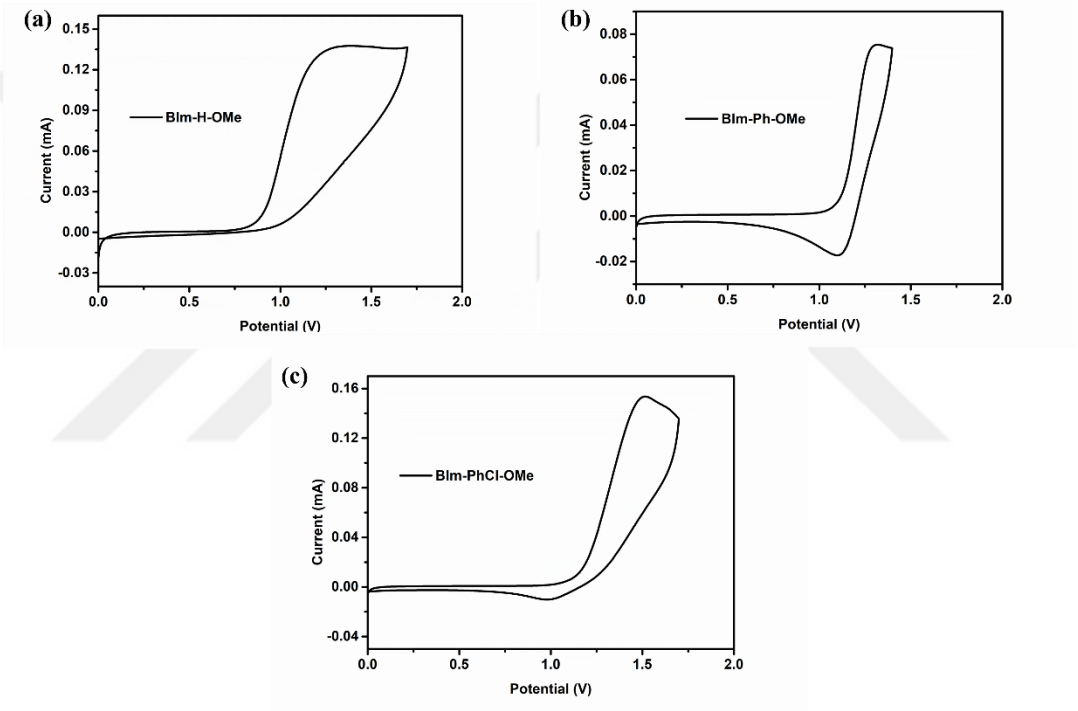

Figure 3.14. Cyclic voltammogram of molecules a) BIm-H-OMe, b) BIm-Ph-OMe, and c) BIm-PhCl-OMe

Table 3-7 Summary of the electrochemical studies of BIm-H-OMe, BIm-Ph-OMe, and BIm-PhCl-OMe

	E^{ox} (V)	E^{red} (V)	E^{ox}_{onset} (V)	E^{red}_{onset} (V)	HOMO (eV)	LUMO (eV)
BIm-H-OMe	1.31	-	1.13	-	-5.88	-2.37
BIm-Ph-OMe	1.25	-	0.90	-	-5.65	-2.33
BIm-PhCl-OMe	1.51	-	1.18	-	-5.93	-2.54

The oxidation onset potentials of molecules BIm-H-*t*Bu, BIm-Ph-*t*Bu, and BIm-PhCl-*t*Bu are 0.89 V, 1.25 V, and 1.29 V, respectively. Their HOMO energy levels were calculated as -5.64 eV, -6.0 eV, -6.04 eV by using the above formula, respectively. In addition, the molecules BIm-H-OMe, BIm-Ph-OMe, and BIm-PhCl-OMe oxidized at 1.13 V, 0.90 V, and 1.18 V, respectively. Like the first three molecules, their HOMO levels were calculated as -5.88 eV, -5.65 eV, and -5.93 eV. For all the molecules, the LUMO energy levels were calculated using the band gap energies, which were calculated from the absorption spectrum of the molecules.

3.1.5 Theoretical Studies

Theoretical studies were conducted to earn a deeper understanding of the intrinsic properties of molecules and their behavior in charge transport in the solid state. The optoelectronic properties are given in Table 3-8. These results are consistent with the experimental studies. Generally, tertiary-butyl substitution has a band gap energy-increasing effect compared to methoxy substituent. For tertiary-butyl and methoxy substituent, the highest band gap energies were obtained from BIm-Ph-tBu (3.59 eV) and BIm-Ph-OMe (3.56 eV), respectively, with the highest level of LUMO energy. For each substitution, the highest E_{ox} were obtained from BIm-PhCI-*t*Bu and BIm-PhCI-OMe at 1.44 eV and 1.38 eV, respectively. It is well known that λ_h and λ_e are widely considered in the performance of OLEDs. λ_h and λ_e, which are the energies required for the structural relaxation in the hole and electron transfer, were lower in

electron and hole pair for BIm-H-*t*Bu and BIm-Ph-OMe for each substitution type, indicating higher order in charge mobility. The lowest VIE and AIE of the hole and the highest VIE and AIE of the electron were obtained from BIm-Ph-*t*Bu and BIm-Ph-OMe, suggesting higher potential candidacy for OLED applications.

Table 3-8 Optoelectronic properties of BIm-H-*t*Bu, BIm-Ph-*t*Bu, BIm-PhCl-*t*Bu, BIm-H-OMe, BIm-Ph-OMe and BIm-PhCl-OMe calculated using DFT B3LYP/6–311+g(d,p) basis sets.

	HOMO (eV)	LUMO (eV)	Eg (eV)	λ_h (eV)	λ_e (eV)	E_{ox} (eV)	E_{red} (eV)	VIE_e (eV)	AIE_e (eV)	VIE_h (eV)	AIE_h (eV)	Dipole (D)
BIm-H-tBu	-5.88	-2.46	3.42	0.29	0.46	1.35	-2.07	-0.16	-0.41	6.77	6.62	3.19
BIm-Ph-tBu	-5.90	-2.31	3.59	0.38	0.49	1.37	-2.22	-0.04	-0.29	6.74	6.54	4.15
BIm-PhCl-tBu	-5.96	-2.45	3.51	0.39	0.47	1.44	-2.08	-0.21	-0.43	6.83	6.63	2.19
BIm-H-OMe	-5.81	-2.42	3.40	0.33	0.63	1.28	-2.12	-0.07	-0.33	6.67	6.50	4.56
BIm-Ph-OMe	-5.83	-2.28	3.56	0.42	0.46	1.31	-2.25	-0.02	-0.24	6.66	6.43	5.31
BIm-PhCl-OMe	-5.90	-2.44	3.47	0.43	0.46	1.38	-2.09	-0.16	-0.39	6.75	6.52	3.35

As given in Table 3-9, the lowest λ_{max} values were obtained using chloroform as solvent from BIm-Ph-*t*Bu (325.77 nm) and BIm-Ph-OMe (329.23 nm) with 0.30 and 0.26 oscillator strength, respectively, agreed with the experimental data.

Table 3-9 Calculated λ_{max} and *f* (oscillator strength) values of BIm-H-*t*Bu, BIm-Ph-*t*Bu, BIm-PhCl-*t*Bu, BIm-H-OMe, BIm-Ph-OMe, and BIm-PhCl-OMe. UV-Vis spectrum for the molecules was calculated using TDDFT calculations using chloroform as solvent.

	λ_{max} (nm)	*f*
BIm-H-*t*Bu	336.45	0.55
BIm-Ph-*t*Bu	325.77	0.30
BIm-PhCl-*t*Bu	331.17	0.22
BIm-H-OMe	340.75	0.43
BIm-Ph-OMe	329.23	0.26
BIm-PhCl-OMe	336.66	0.16

HOMO, HOMO-1, LUMO, LUMO+1, and ESP surfaces mapped onto the optimized geometries of six molecules are shown in Figure 1. The HOMO and LUMO orbitals are delocalized on the donor and the acceptor parts of the molecules, while HOMO-1 and LUMO+1 orbitals show more distinct localization on each unit. The phenyl chloride unit has a decreasing effect on HOMO level, whereas the phenyl unit has a more significant increasing influence on the LUMO energy level of molecules for both substitution types, leading to the highest band gap energy for BIm-Ph-*t*Bu and BIm-Ph-OMe. As a result, BIm-Ph-*t*Bu>BIm-PhCI-*t*Bu>BIm-H-*t*Bu>BIm-Ph-OMe>BIm-PhCI-OMe> BIm-H-OMe for the order of band gaps have been obtained that agree with the experimental results. ESP surfaces show high electrostatic potential in red color and low electrostatic potential in blue color in Figure 3.15. The high electrostatic potential is concentrated in the planar donor part of the imidazole derivatives for all cases. Localization of the electron-deficient part was more visible for BIm-Ph-*t*Bu and BIm-Ph-OMe, which were represented by an intensive blue color on each phenyl unit, leading to better acceptor properties.

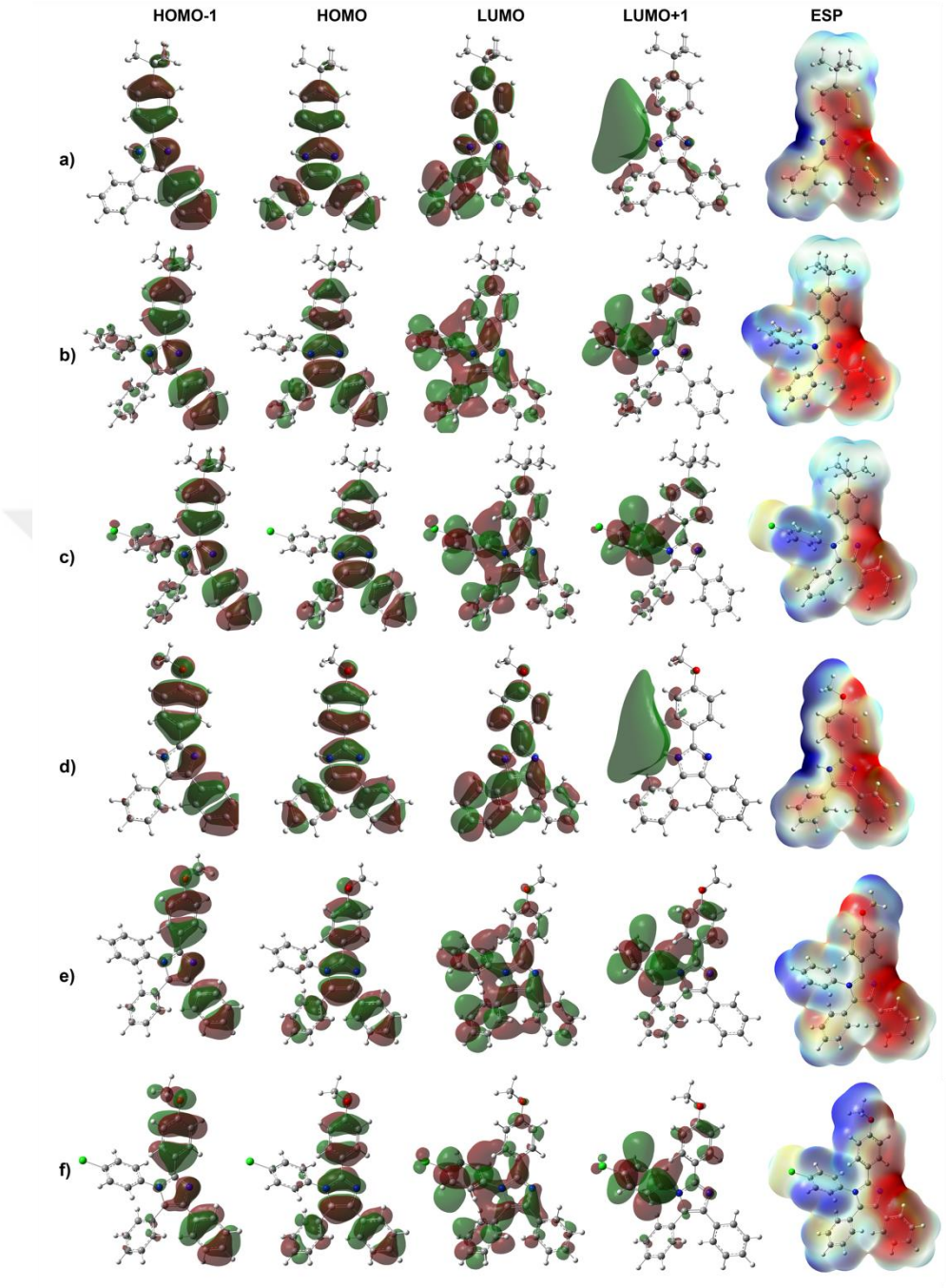

Figure 3.15. Frontier orbitals and ESP surfaces of a) BIm-H-*t*Bu, b) BIm-Ph-*t*Bu, c) BIm-PhCl-*t*Bu, d) BIm-H-OMe, e) BIm-Ph-OMe, and f) BIm-PhCl-OMe.

3.2 Optoelectronic Studies

OLED devices were fabricated using synthesized molecules in emissive material. After several trials, only the two molecules, BIm-Ph-*t*Bu and BIm-Ph-OMe, performed well out of the six molecules. This result supports the findings and predictions obtained in the theoretical studies presented in Section 3.1.5. Here, it can be understood that molecules that do not have a substituent at the N3 position in the imidazole core unit and those with a para-chlorophenyl substituent are unsuitable for use in OLED device fabrication. The substituents added to the N3 position of the imidazole molecule do not significantly affect its photophysical properties. The primary purpose of these substituents is to arrange molecular packing and regulate molecular interactions in this context [65]. In the prevention of non-radiative energy transfers, it is understood that closer molecular packing contributes significantly to conjugated systems [66]. The phenyl substituent attached to the N3 position fulfills this role, whereas the para-chlorophenyl substituent fails to do so. The chlorine atom in this substituent might be inhibiting π-π stacking interactions and hydrogen bonding between molecules in the solid state. For the other two molecules, BIm-H-*t*Bu and BIm-H-OMe, the absence of any substituent at the N3 position may have caused the molecules to accumulate within themselves, leading to poor performance due to induction in the balanced charge transport. The close proximity between planar-structured molecules when in a solid state causes aggregation-induced red-shift and self-quenching phenomena, leading to a reduction in both color purity and efficiency of electroluminescence [67]. Consequently, optimizations were done for molecules containing phenyl substituent in the N3 position. Optimizations were based on adjusting the thickness of the layers for balanced recombination of the charge carriers.

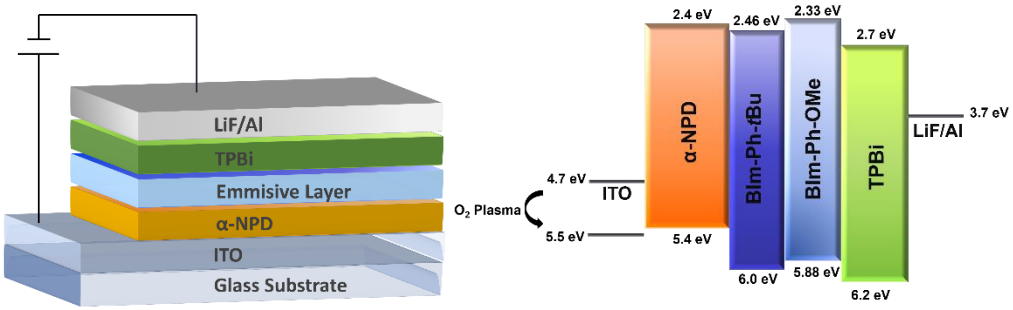

Figure 3.16. Architecture and energy level diagram of devices

The device architecture is as follows: ITO/α-NPD/EML/TPBi/LiF/Al. This and its energy level diagram are shown in Figure 3.14. ITO was the front contact, consisting of the anode electrode. α-NPD and TPBi were used as hole and electron transport layers, respectively. The function of LiF was working as a buffer layer between Al and organic films. Also, Al was the cathode contact. LiF and Al were deposited at 0.6 nm and 100 nm for all devices. The reason for selecting these layers in the device architecture is their compatibility, as seen in Figure 3.16, with the materials used in the emissive layer in terms of their HOMO-LUMO levels. The -5.4 eV HOMO level of α-NPD is compatible with the work function of ITO after exposure to O_2 plasma, facilitating hole transfer quickly. Additionally, the HOMO levels of the BIm-Ph-*t*Bu and BIm-Ph-OMe materials used in the EML are also well-matched for charge carrier transfer. The LUMO energy level difference between TPBi and the LUMO levels of the imidazole molecules is compatible. Therefore, TPBi was chosen as the electron transport layer to avoid any charge carrier injection imbalance.

Different thicknesses were performed for HTL, EML, and ETL, resulting in the optimum device architecture. The optimization started with HTL and ended with ETL for both devices based on BIm-Ph-*t*Bu and BIm-Ph-OMe molecules.

3.2.1 Optimizations of Device Based BIm-Ph-*t*Bu

Optimizations for the device based on BIm-Ph-*t*Bu began with the HTL. This was followed by EML optimizations. Subsequently, ETL adjustments were conducted. Finally, the buffer layer LiF was replaced with Ca, completing the optimizations.

3.2.1.1 HTL Optimizations

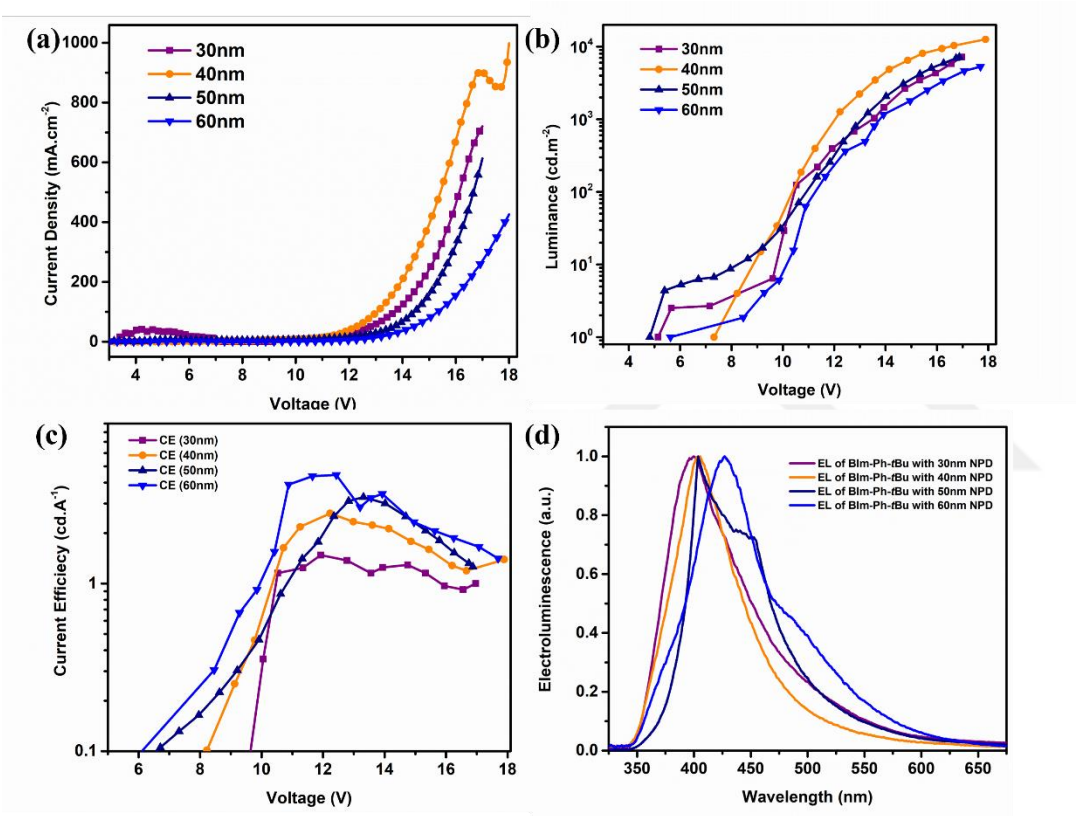

Figure 3.17. a) Jsc vs. Voltage graph, b) Luminance vs. Voltage graph, c) CE vs. Voltage graph, and d) Electroluminescence spectrum of device-based BIm-Ph-*t*Bu molecule with changing thickness HTL from 30nm to 60nm

Table 3-10 Summary of HTL thickness optimization in device-based BIm-Ph-*t*Bu

Thickness of Layer	V_{on} (V)	η_c (cd.A^{-1})	L_{max} (cd.m^{-2})	FWHM (nm)	CIE (x,y)
30nm	5.1	1.48	7169	79	(0.19, 0.15)
40nm	7.3	2.63	12612	90	(0.17, 0.10)
50nm	4.8	3.28	7163	88	(0.18, 0.12)
60nm	5.6	4.45	5280	80	(0.18, 0.16)

The HTL optimization was conducted by varying the thickness between 30 and 60 nm in 10 nm increments while keeping the other layers constant. At this stage, EML as BIm-Ph-*t*Bu and ETL as TPBi were deposited at 20 nm and 30 nm thick, respectively. The cathode metal and LiF were deposited at 100 nm and 0.6 nm. The combination of current density vs. voltage, luminance vs. voltage, current efficiency vs. voltage graphs, and electroluminescence spectrums for devices with different HTL thicknesses are shown in Figure 3.17. Moreover, the critical parameters which are turn-on voltage (V_{on}), current efficiency (η_c), maximum lumen value (L_{max}), full width at half maximum, which is the bandwidth of electroluminescence spectrum at its half maximum intensity (FWHM) value, and color values for these devices were shown in Table 3-8. 40 nm thick HTL gave a higher lumen value and deeper blue color in color coordination, which can be seen in Table 3-10. Even though this device did not have the highest current efficiency and the narrowest FWHM value among the others, the correct layer thickness for this layer has been determined based on properties such as high lumen and a deeper blue color for a device containing a 40nm thick HTL.

3.2.1.2 EML Optimizations

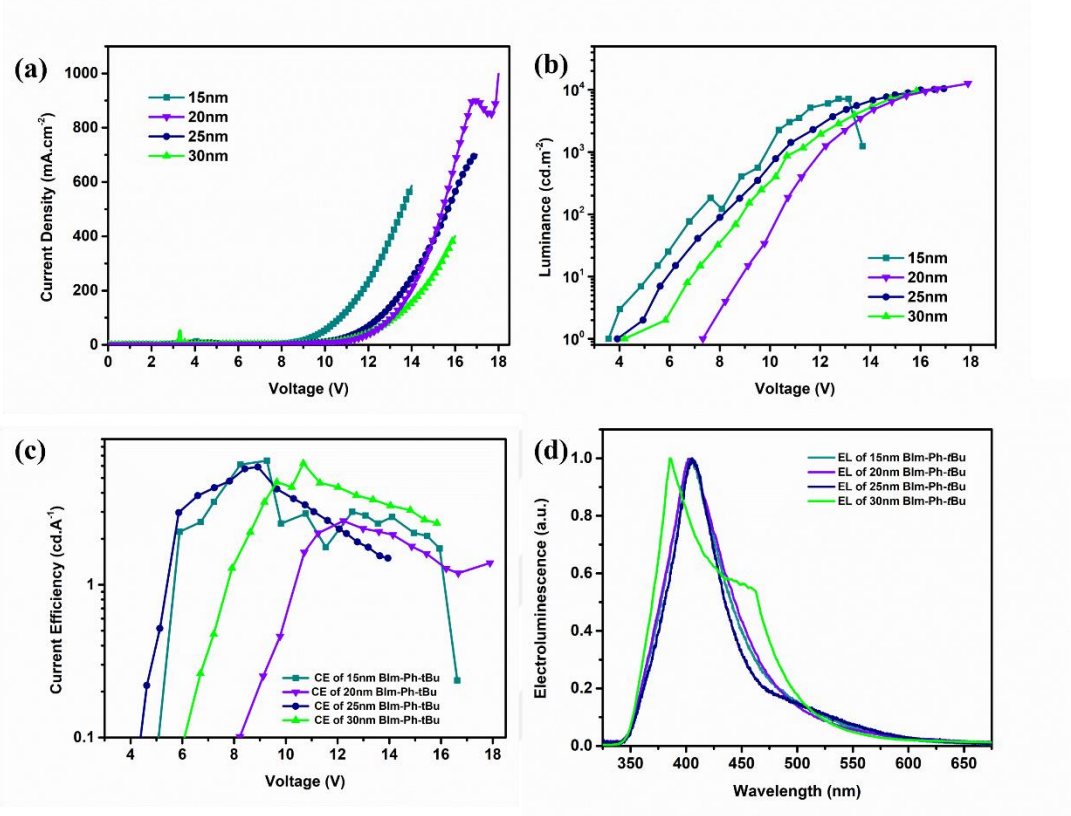

Figure 3.18. a) Jsc vs Voltage graph, b) Luminance vs. Voltage graph, c) CE vs. Voltage graph, and d) Electroluminescence spectrum of device-based BIm-Ph-tBu molecule and changing EML thickness from 15nm to 30nm

Table 3-11 Summary of EML thickness optimization in device-based BIm-Ph-*t*Bu

Thickness of Layer	V_{on} (V)	η_c (cd.A^{-1})	L_{max} (cd.m^{-2})	FWHM (nm)	CIE (x,y)
15nm	3.5	6.1	7154	63	(0.18, 0.13)
20nm	7.3	2.63	12612	90	(0.17, 0.10)
25nm	3.9	5.90	10445	53	(0.19, 0.14)
30nm	4.7	6.20	9659	94	(0.17, 0.10)

Optimizations for EML were studied by depositing BIm-Ph-*t*Bu from 15nm to 30nm in 5nm increments while keeping the other layers constant. Due to the optimum HTL

thickness being found out as 40 nm, in all subsequent devices, HTL has been used as 40 nm. TPBi LiF and Al were deposited as 40 nm, 0.6 nm, and 10 nm thick, respectively. According to Table 3-9, the turn-on voltage of a 15 nm thick HTL-containing device was the lowest one, and its current efficiency value was close to the highest one (6.2 $cd.A^{-1}$), which was achieved with the device featuring an HTL of 30 nm thickness. Although the highest lumen value, which is 12612, was obtained with a device incorporating an HTL 15 nm thick, it has poor performance according to the ηc, V_{on}, and FWHM parameters. While the highest η_c value was obtained with a device containing an HTL with a thickness of 30 nm, its FWHM value is very broad. As can be seen from Figure 3.18 and Table 3-11, a 25 nm thick EML-containing device turned on at a relatively lower voltage, 3.9 V. Moreover, having the lowest FWHM value, it also demonstrates a good performance with a current efficiency of 4.9 $cd.A^{-1}$ and a lumen value of 10445 $cd.m^{-2}$. As a result, the best option for HTL thickness was determined to be 25 nm thickness.

3.2.1.3 ETL Optimizations

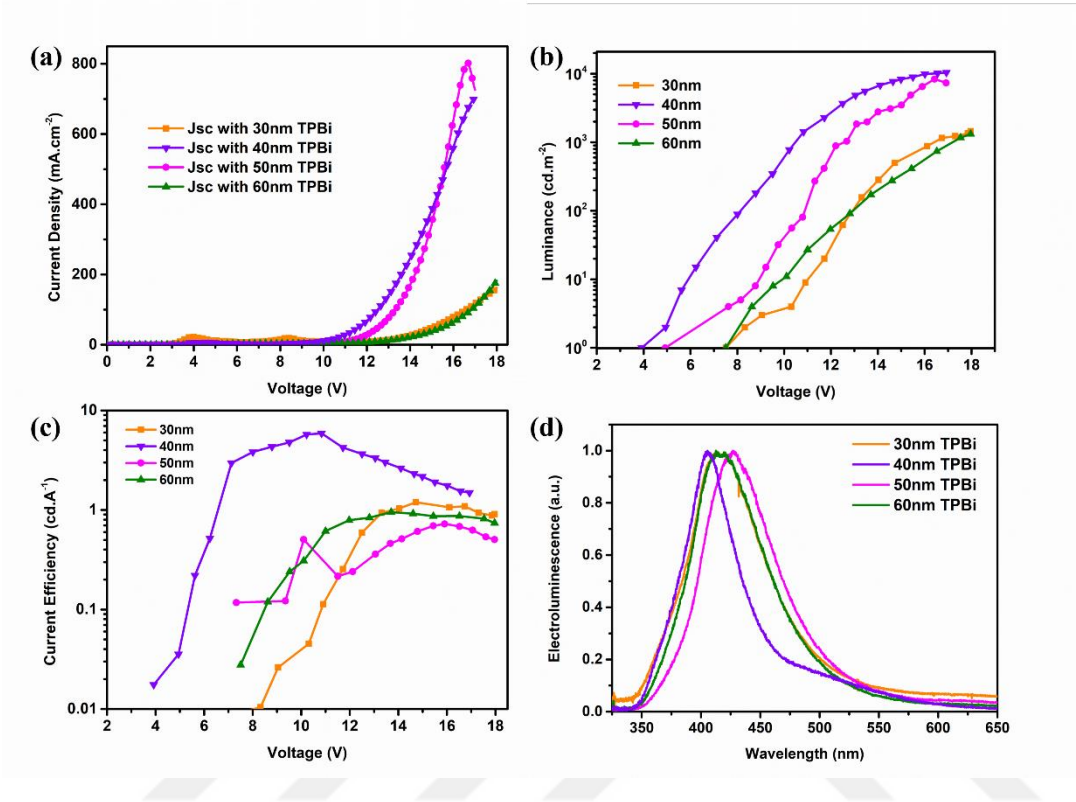

Figure 3.19. a) Jsc vs. Voltage graph, b) Luminance vs. Voltage graph, c) CE vs. Voltage graph, and d) Electroluminescence spectrum of device-based BIm-Ph-tBu molecule with changing thickness ETL from 30nm to 60nm

Table 3-12 Summary of ETL thickness optimization in device-based BIm-Ph-*t*Bu

Thickness of Layer	V_{on} (V)	η_c (cd.A^{-1})	L_{max} (cd.m^{-2})	FWHM (nm)	CIE (x,y)
30nm	7.5	1.20	1455	77	(0.18, 0.10)
40nm	3.9	5.90	10445	53	(0.18, 0.14)
50nm	7.3	0.72	1137	73	(0.18, 0.11)
60nm	7.5	0.95	1321	75	(0.18, 0.10)

During the ETL thickness optimization, HTL and EML were evaporated to a thickness of 40 nm and 25 nm. The buffer layer LiF and top contact Al were

deposited at 0.6 nm and 100 nm. The thickness of the ETL, TPBi, was changed between 30 nm to 60 nm. The current density, luminance current efficiency vs. voltage graphs, and EL spectrum of all devices were shown together in Figure 3.19. Devices containing TPBi at 30 nm, 50 nm, and 60 nm exhibited significantly lower performance compared to the 40 nm thick ETL-containing device, as can be observed from Table 3.10. According to Table 3.12, while the turn-on voltages of those devices are around 7.5 V, that of the one containing 40 nm TPBi is 3.9 V. Besides this, η_c and L_{max} values, being as 5.9 $cd.A^{-1}$ and $cd.m^{-2}$ of 40 nm thick ETL device, are considerably higher than the rest. In addition to these, depositing ETL for 40 nm decreases the FWHM from the EL spectrum.

3.2.1.4 CIL Optimizations

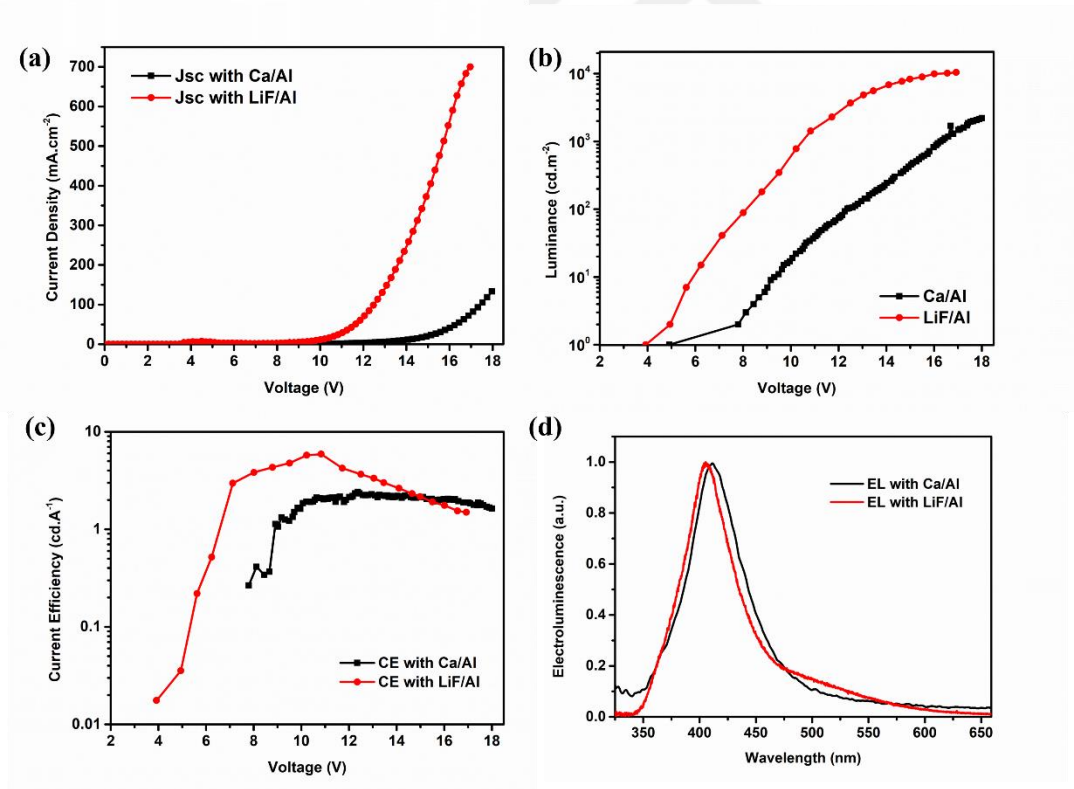

Figure 3.20. a) Jsc vs. Voltage graph, b) Luminance vs. Voltage graph, c) CE vs. Voltage graph, and d) Electroluminescence spectrum of device-based BIm-Ph-tBu molecule with changing CIL, LiF with Ca

Table 3-13 Summary of CIL optimization in device-based BIm-Ph-tBu

CIL	V_{on} (V)	η_c (cd.A^{-1})	L_{max} (cd.m^{-2})	FWHM (nm)	CIE (x,y)
Ca	4.9	2.64	2210	57	(0.19, 0.11)
LiF	3.9	5.90	10445	53	(0.18, 0.14)

The last optimization of a device containing BIm-Ph-*t*Bu in EML is changing the buffer layer. As seen from Figure 3.20. and Table 3-13, the performance of the device was decreased when using Ca under Al as interlayer. The parameters crucial for determining device performance were negatively influenced. Moreover, the light emitted by the device shifted from a darker blue shade to a lighter blue shade with Ca containing device.

As a result of all these studies for BIm-Ph-tBu-based OLED devices, the optimum device architecture was determined as ITO/αNPD(40nm)/EML(25nm)/TPBi(40nm)/LiF(0.6nm)/Al(100nm).

3.2.2 Optimizations of Device Based BIm-Ph-OMe

To achieve a higher-performance device-based BIm-Ph-OMe molecule, thickness optimizations for HTL, EML, and ETL were performed, similar to the previous device type. Also, a small study was conducted in an effort to explore the potential benefits of using a different buffer layer to determine if this would lead to any improvements in device performance.

3.2.2.1 HTL Optimizations

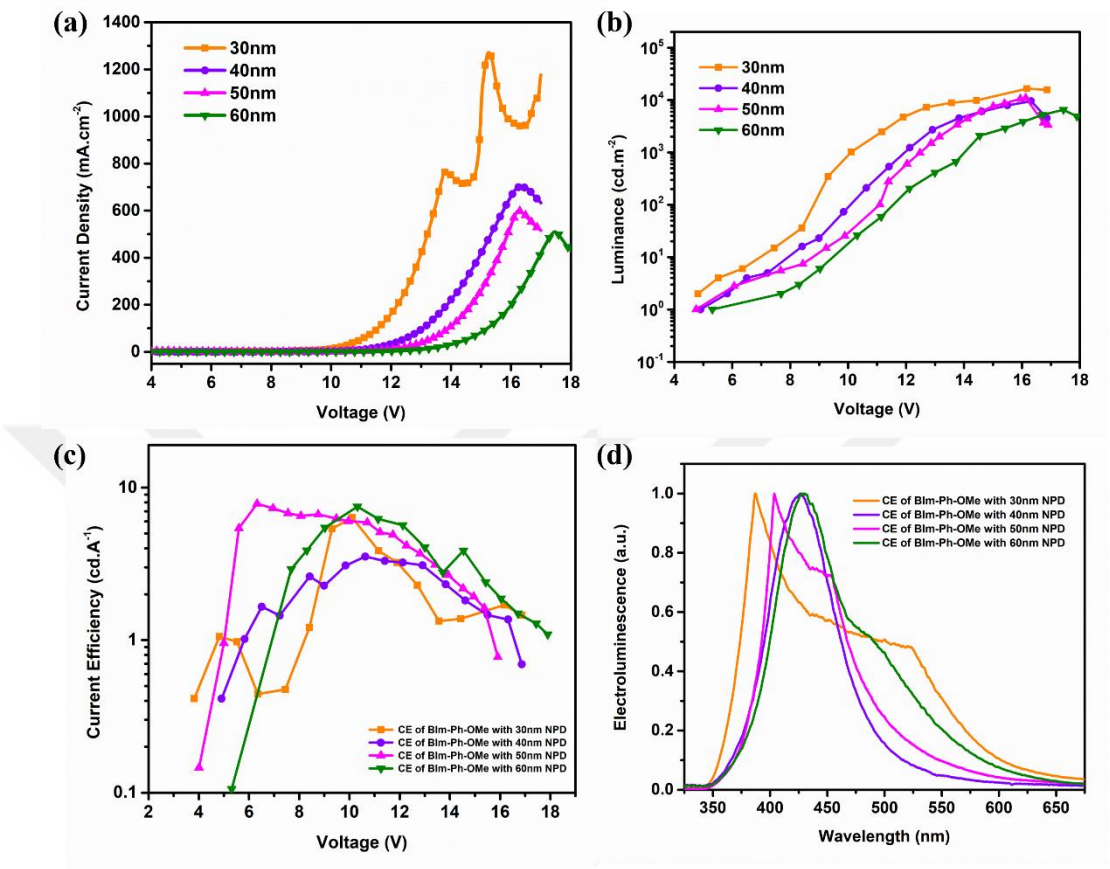

Figure 3.21. a) Jsc vs. Voltage graph, b) Luminance vs. Voltage graph, c) CE vs. Voltage graph, and d) Electroluminescence spectrum of device-based BIm-Ph-OMe molecule with changing thickness HTL from 30nm to 60nm

Table 3-14 Summary of HTL thickness optimization in device-based BIm-Ph-OMe

Thickness of Layer	V_{on} (V)	η_c (cd.A^{-1})	L_{max} (cd.m^{-2})	FWHM (nm)	CIE (x,y)
30nm	3.8	6.35	16442	128	(0.20, 0.21)
40nm	4.9	4.8	4531	72	(0.17, 0.11)
50nm	4.5	7.84	10393	71	(0.18, 0.12)
60nm	5.3	7.51	6536	91	(0.18, 0.17)

The optimization of HTL was carried out through the variation of thickness ranging from 30 nm to 60 nm in increments of 10 nm, with the remaining layers held constant as in the previous device type. During this phase, EML was utilized as BIm-Ph-OMe and ETL as TPBi, at 20 nm and 30 nm thicknesses, respectively. The cathode metal and LiF were deposited at 100 nm and 0.6 nm. Figure 3.21. compares current density versus voltage, luminance versus voltage, current efficiency versus voltage graphs, and electroluminescence spectrums for devices with different HTL thicknesses. Additionally, Table 3-14 displayed crucial parameters, including V_{on}, η_c, Lmax, and FWHM, and color values for these devices.

3.2.2.2 EML Optimizations

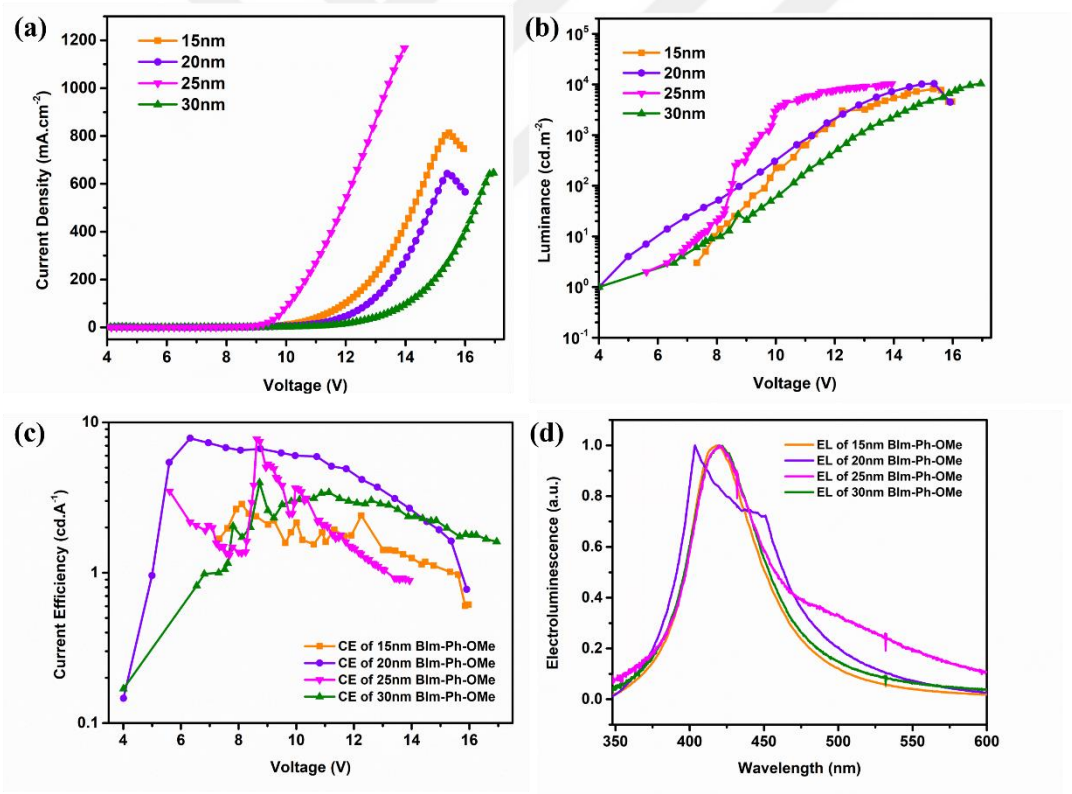

Figure 3.22. a) Jsc vs Voltage graph, b) Luminance vs. Voltage graph, c) CE vs. Voltage graph, and d) Electroluminescence spectrum of device-based BIm-Ph-OMe molecule and changing EML thickness from 15 nm to 30 nm

Table 3-15 Summary of EML thickness optimization in device-based BIm-Ph-OMe

Thickness of Layer	V_{on} (V)	η_c (cd.A^{-1})	L_{max} (cd.m^{-2})	FWHM (nm)	CIE (x,y)
15nm	3.9	2.86	8123	53	(0.18, 0.12)
20nm	4.5	7.84	10393	71	(0.17, 0.11)
25nm	3.9	7.73	10288	60	(0.18, 0.14)
30nm	4.0	3.98	10405	58	(0.17, 0.10)

After completing the HTL optimization and deciding that the most optimal thickness for this layer is 50 nm, studies continued with the EML optimization. EML thickness was changed from 15 nm to 30 nm by keeping the other variables constant. The optimization results for this layer are shown in Figure 3.22 and Table 3-15. V_{on} and FWHM values for 20 nm thick BIm-Ph-OMe are 3.9 V and 60 nm, which are higher than the other devices. These characteristics have proven that this thickness is not the optimal choice, even if it results in the highest η_c. The purest blue color was obtained with a 15 nm thick EML-containing device, yet the lowest efficiency belongs to this device. The optimum thickness, which is highlighted in Table 3-15, was determined as 25 nm for this layer due to having the lowest Von (3.9 V), narrow bandwidth (60 nm), high lumen value (10288 cd.m^{-2})and relatively high efficiency (7.73 cd.A^{-1}).

3.2.2.3 ETL Optimizations

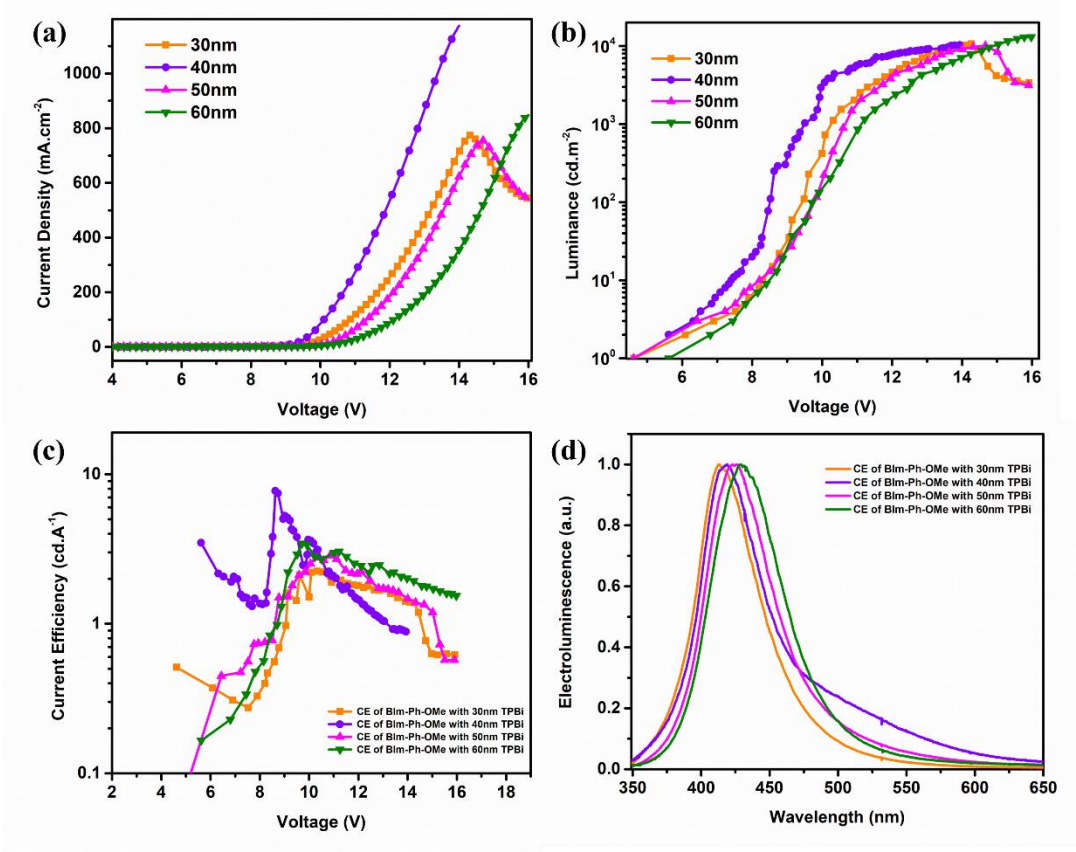

Figure 3.23. a) Jsc vs. Voltage graph, b) Luminance vs. Voltage graph, c) CE vs. Voltage graph, and d) Electroluminescence spectrum of device-based BIm-Ph-OMe molecule with changing thickness ETL from 30nm to 60nm

Table 3-16 Summary of ETL thickness optimization in device-based BIm-Ph-OMe

Thickness of Layer	V_{on} (V)	η_c (cd.A^{-1})	L_{max} (cd.m^{-2})	FWHM (nm)	CIE (x,y)
30nm	4.6	2.25	10657	54	(0.16, 0.06)
40nm	3.9	7.73	10288	60	(0.18, 0.14)
50nm	4.6	2.85	10127	59	(0.17, 0.08)
60nm	5.6	3.44	13021	62	(0.16, 0.07)

During the optimization process of the ETL thickness, the HTL and EML layers were deposited to achieve a thickness of 50 nm and 25 nm, respectively. Subsequently, the buffer layer LiF and top contact Al were applied at 0.6 nm and 100 nm thicknesses. The ETL layer, TPBi, was varied from 30 nm to 60 nm. Figure 3.23. presents the current density, luminance, current efficiency vs. voltage curves, and EL spectrum for all devices collectively. Devices with TPBi thicknesses of 30 nm, 50 nm, and 60 nm displayed notably inferior performance in comparison to the device with a 40 nm thick ETL layer, as evidenced in Table 3-16. As indicated in Table 3-14, the turn-on voltages for the former devices are approximately 5 V, while the device with 40 nm TPBi has a turn-on voltage of 3.9 V. Moreover, the values of η_c and $L_{max,}$ which are 7.73 $cd.A^{-1}$ and 10288 $cd.m^{-2}$, respectively, for the 40 nm thick ETL device, are significantly higher than those of the other devices. Furthermore, depositing the ETL layer at 40 nm reduces the Von and increases in η_c.

3.2.2.4 CIL Optimizations

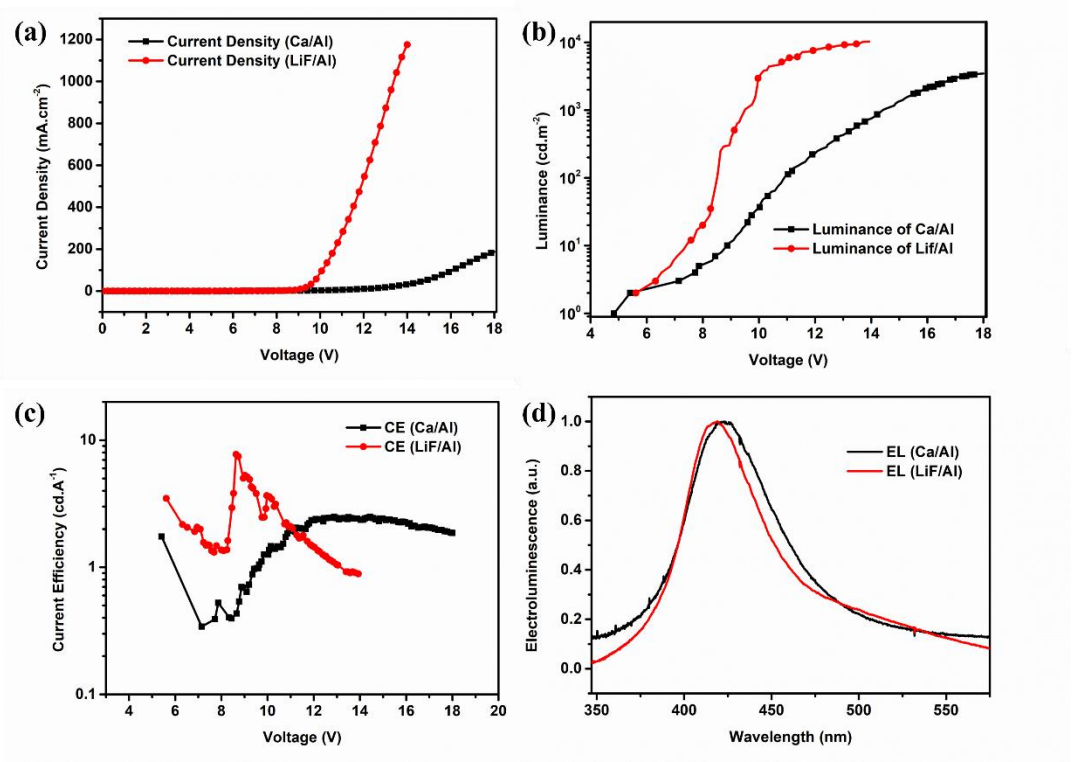

Figure 3.24. a) Jsc vs. Voltage graph, b) Luminance vs. Voltage graph, c) CE vs. Voltage graph, and d) Electroluminescence spectrum of device-based BIm-Ph-OMe molecule with changing CIL, LiF with Ca

Table 3-17 Summary of CIL optimization in device-based BIm-Ph-OMe

Thickness of Layer	V_{on} (V)	η_c (cd.A^{-1})	L_{max} (cd.m^{-2})	FWHM (nm)	CIE (x,y)
Ca	4.8	2.59	3479	66	(0.16, 0.07)
LiF	3.9	7.73	10288	60	(0.18, 0.14)

The final enhancement of the device incorporating BIm-Ph-*t*Bu in EML involves modifying the buffer layer. This alteration decreased device performance, as illustrated in Figure 3.24. and Table 3-17, when utilizing Ca instead of Al as the interlayer. The essential parameters that determine the device's performance were

adversely affected. Furthermore, the light emitted by the device transitioned from a darker blue hue to a lighter blue shade with a Ca-inclusive device.

Following an extensive examination of the BIm-Ph-tBu-based OLED device, the most effective device architecture was identified as ITO/α-NPD(50nm)/EML(25nm)/TPBi(40nm)/LiF(0.6nm)/Al(100nm).

3.2.3 Optimization Results

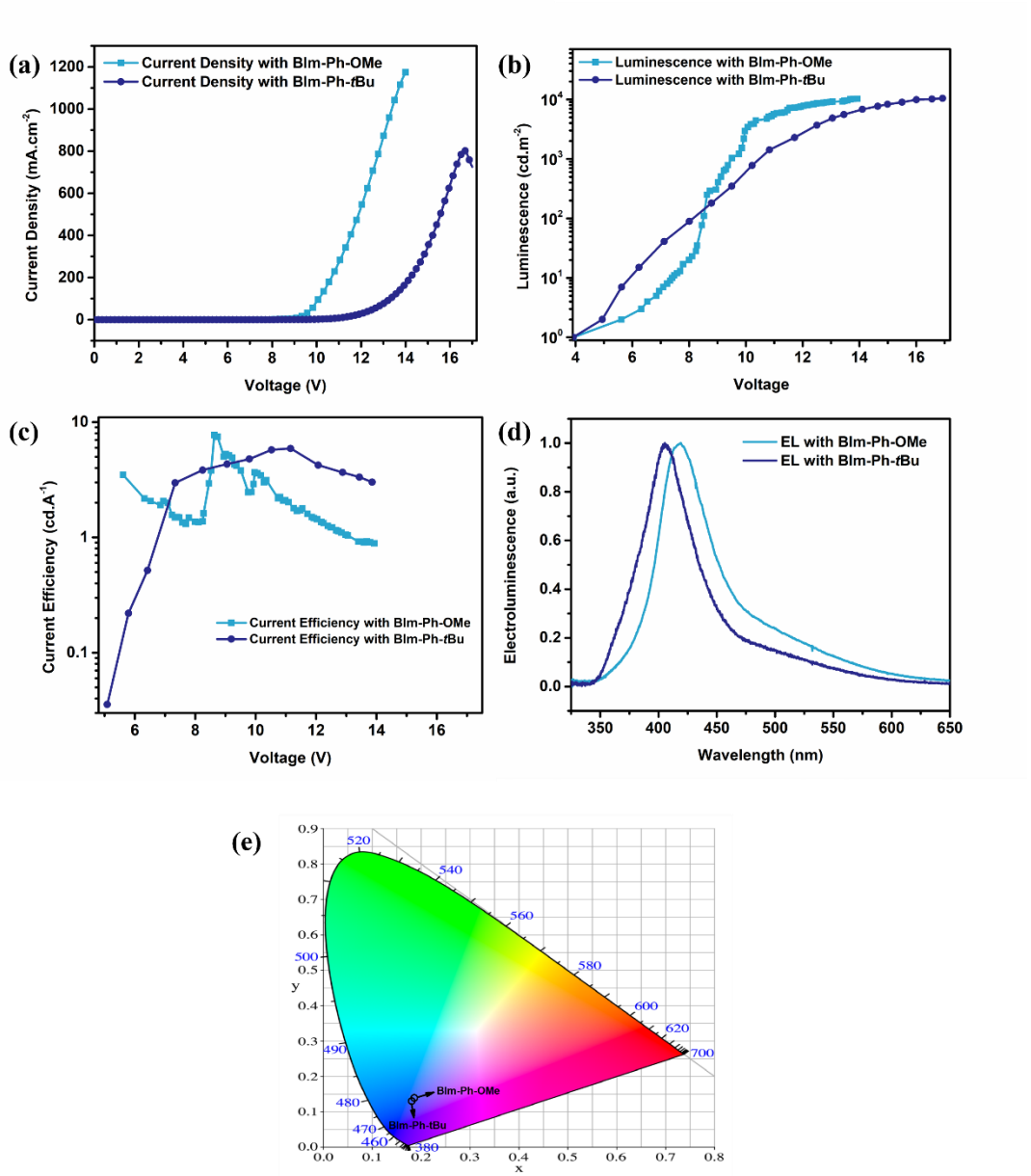

Figure 3.25. Combine versions of a) Current Density vs. Voltage Graph, b) Luminance vs. Voltage Graph, c) Current Efficiency vs. Voltage Graph, d) Electroluminescence Spectrum of best-performed device-based BIm-Ph-*t*Bu and BIm-Ph-OMe

Table 3-18 Comparison of the device performance based on BIm-Ph-*t*Bu and BIm-Ph-OMe

EML	V_{on} (V)	η_c (cd.A^{-1})	L_{max} (cd.m^{-2})	λ_{max} (nm)	FWHM (nm)	CIE (x,y)
BIm-Ph-*t*Bu	3.9	5.90	10445	406	53	(0.18, 0.14)
BIm-Ph-OMe	3.9	7.73	10288	419	60	(0.18, 0.14)

The optimized versions of both molecule-based devices are shown comparatively in Figure 3.25. As seen in Table 3-18, the performances of these two devices are quite similar. The band gaps of these molecules are very close to each other, resulting in similar outcomes in their optimized device versions. Both devices have a quite low turn-on voltage. The BIm-Ph-*t*Bu molecule-based device has a L_{max} value of 10445 cd.m^{-2}, which is around 200 cd.m^{-2} higher than the other device. However, the BIm-Ph-OMe molecule-based device has a maximum current efficiency of 7.73 cd.A^{-1}, which is 1.5 cd.A^{-1} higher than the other device. This is due to the luminance value being higher relative to the current density at the voltage where maximum η_c is achieved, different than the device-based BIm-Ph-*t*Bu. As per existing literature, the introduction of a *tert*-butyl-phenyl moiety through the employment of a steric hindrance approach is recognized for its ability to escalate steric inhibition, consequently impeding self-aggregation, preventing intramolecular vibrational relaxation and ultimately advancing intramolecular electron transfer [67–71]. At this point, it has been noted that the two compounds containing distinct electron-donating entities, namely tertiary-butyl and methoxy, did not manifest markedly disparate impacts based on their position.

CHAPTER 4

CONCLUSIONS

Six different imidazole derivatives, BIm-H-*t*Bu, BIm-Ph-*t*Bu, BIm-PhCl-*t*Bu, BIm-H-OMe, BIm-Ph-OMe, and BIm-PhCl-OMe, were synthesized and structures were confirmed by NMR spectra and HRMS. Optical, electrochemical, and photophysical studies were carried out in order to characterize molecules. The optical and electrochemical properties of the molecules, BIm-H-*t*Bu, BIm-Ph-*t*Bu, BIm-PhCl-*t*Bu, BIm-H-OMe, BIm-Ph-OMe, and BIm-PhCl-OMe are consistent with the theoretical calculation results. The photoluminescence spectra of the molecules depicted their maximum emission wavelengths in the blue region of the spectrum. The two molecules are suitable for OLED application. After optimizations of their devices, the ideal device architectures for optimum charge balance are determined as follows;

ITO/α-NPD(40nm)/BIm-Ph-*t*Bu(25nm)/TPBi(40nm)/LiF(0.6nm)/Al(100nm)

ITO/α-NPD(50nm)/BIm-Ph-OMe(25nm)/TPBi(40nm)/LiF(0.6nm)/Al(100nm).

These devices were turned on at 3.9 V, and their L_{max} values are over 10,000 $cd.m^{-2}$. The highest η_c obtained over 7.0 $cd.A^{-1}$. The emission from devices based on both molecules, as well as the FWHM values of their EL spectra, are less than 450 nm and 60 nm, respectively. This demonstrates a pure blue color emission.

REFERENCES

[1] Xi N, Huang Q, Liu L. Imidazoles. Comprehensive Heterocyclic Chemistry III, Elsevier; 2008, p. 143–364. https://doi.org/10.1016/B978-008044992-0.00402-8.

[2] Godge R, Dighe A, Kolhe P. An Overview of Imidazole, Derivatives Ofimidazole and its Pharmacological Applications. Asian Journal of Research in Chemistry 2023:71–8. https://doi.org/10.52711/0974-4150.2023.00012.

[3] Hofmann C, editor. Chemistry of Heterocyclic Compounds. vol. 6. Wiley; 1953. https://doi.org/10.1002/9780470186541.

[4] Lin Y, Tsai W, Lu C. Exploring the Electroluminescent Applications of Imidazole Derivatives. Chemistry – A European Journal 2023;29. https://doi.org/10.1002/chem.202203040.

[5] Shabalin DA, Camp JE. Recent advances in the synthesis of imidazoles. Org Biomol Chem 2020;18:3950–64. https://doi.org/10.1039/D0OB00350F.

[6] Chandler ASR by K, Keep A, Ellis S, Ball S. "Combinatorial and High-Throughput Discovery and Optimization of Catalysts and Materials." Platin Met Rev 2007;51:204–7. https://doi.org/10.1595/147106707X238860.

[7] KAVAKCIOĞLU YARDIMCI B. Imidazole Antifungals: A Review of Their Action Mechanisms on Cancerous Cells. International Journal of Secondary Metabolite 2020;7:139–59. https://doi.org/10.21448/ijsm.714310.

[8] Anderson EB, Long TE. Imidazole- and imidazolium-containing polymers for biology and material science applications. Polymer (Guildf) 2010;51:2447–54. https://doi.org/10.1016/j.polymer.2010.02.006.

[9] Cornec A-S, Monti L, Kovalevich J, Makani V, James MJ, Vijayendran KG, et al. Multitargeted Imidazoles: Potential Therapeutic Leads for Alzheimer's

and Other Neurodegenerative Diseases. J Med Chem 2017;60:5120–45. https://doi.org/10.1021/acs.jmedchem.7b00475.

[10] Wang Z, Lu P, Chen S, Gao Z, Shen F, Zhang W, et al. Phenanthro[9,10-d]imidazole as a new building block for blue light emitting materials. J Mater Chem 2011;21:5451. https://doi.org/10.1039/c1jm10321k.

[11] Xiao L, Su S, Agata Y, Lan H, Kido J. Nearly 100% Internal Quantum Efficiency in an Organic Blue- Light Electrophosphorescent Device Using a Weak Electron Transporting Material with a Wide Energy Gap. Advanced Materials 2009;21:1271–4. https://doi.org/10.1002/adma.200802034.

[12] Will P-A, Reineke S. Organic light-emitting diodes. In: Ostroverkhova O, editor. Handbook of Organic Materials for Electronic and Photonic Devices. 2nd ed., Duxford: Elsevier; 2019, p. 704. https://doi.org/10.1016/B978-0-08-102284-9.00021-8.

[13] 'Islam A, 'Tsou C-C, 'Hsu H-J, 'Shih W-L', 'Liu C-H, 'Cheng C-H'. Novel Blue Fluorescent Dopants Based on Imidazole-Containing Compound for Organic Electroluminescent Devices . Journal of Applied Science and Engineering 2002;5.

[14] Murthy KVR, Virk HS. Luminescence Phenomena: An Introduction. Defect and Diffusion Forum 2013;347:1–34. https://doi.org/10.4028/www.scientific.net/DDF.347.1.

[15] Ladiler KJ, Meiser JH. Physical Chemistry. 3rd ed. Boston: Houghton Mifflin Company; 1999.

[16] Atkins P, Paula J. Physical Chemistry: Thermodynamics, Structure and Change. 10th ed. New York: Oxford University Press; 2014.

[17] Capelletti R. Luminescence. Encyclopedia of Condensed Matter Physics, Elsevier; 2005, p. 178–89. https://doi.org/10.1016/B0-12-369401-9/00675-6.

[18] Destriau G, Ivey H. Electroluminescence and Related Topics. Proceedings of the IRE 1955;43:1911–40. https://doi.org/10.1109/JRPROC.1955.278058.

[19] Juqing G, Li Z, Li Q. From single molecule to molecular aggregation science. Coord Chem Rev 2022.

[20] Tyan Y-S. Organic light-emitting-diode lighting overview. J Photonics Energy 2011;1:011009. https://doi.org/10.1117/1.3529412.

[21] Ha JM, Hur SH, Pathak A, Jeong J-E, Woo HY. Recent advances in organic luminescent materials with narrowband emission. NPG Asia Mater 2021;13:53. https://doi.org/10.1038/s41427-021-00318-8.

[22] Bauri J, Choudhary RB, Mandal G. Recent advances in efficient emissive materials-based OLED applications: a review. J Mater Sci 2021;56:18837–66. https://doi.org/10.1007/s10853-021-06503-y.

[23] Keum C, Murawski C, Archer E, Kwon S, Mischok A, Gather MC. A substrateless, flexible, and water-resistant organic light-emitting diode. Nat Commun 2020;11:6250. https://doi.org/10.1038/s41467-020-20016-3.

[24] Patel BN, Prajapati MM. OLED: A modern display technology. International Journal of Scientific and Research Publications 2014;4.

[25] Pope M, Kallmann HP, Magnante P. Electroluminescence in Organic Crystals. J Chem Phys 1963;38:2042–3. https://doi.org/10.1063/1.1733929.

[26] Helfrich W, Schneider WG. Recombination Radiation in Anthracene Crystals. Phys Rev Lett 1965;14:229–31. https://doi.org/10.1103/PhysRevLett.14.229.

[27] Vincett PS, Barlow WA, Hann RA, Roberts GG. Electrical conduction and low voltage blue electroluminescence in vacuum-deposited organic films. Thin Solid Films 1982;94:171–83. https://doi.org/10.1016/0040-6090(82)90509-0.

[28] Tang CW, VanSlyke SA. Organic electroluminescent diodes. Appl Phys Lett 1987;51:913–5. https://doi.org/10.1063/1.98799.

[29] Pioneer Corporation. Pioneer 1999. Retrieved from: https://global.pioneer/en/corp/news/press/index/1484

[30] Sony Group Corporation. SONY 2007. Retrieved from: https://www.sony.com/en/SonyInfo/News/Press/200710/07-1001E/

[31] Hong G, Gan X, Leonhardt C, Zhang Z, Seibert J, Busch JM, et al. A Brief History of OLEDs—Emitter Development and Industry Milestones. Advanced Materials 2021;33. https://doi.org/10.1002/adma.202005630.

[32] Endo A, Sato K, Yoshimura K, Kai T, Kawada A, Miyazaki H, et al. Efficient up-conversion of triplet excitons into a singlet state and its application for organic light emitting diodes. Appl Phys Lett 2011;98. https://doi.org/10.1063/1.3558906.

[33] Tanaka H, Shizu K, Miyazaki H, Adachi C. Efficient green thermally activated delayed fluorescence (TADF) from a phenoxazine–triphenyltriazine (PXZ–TRZ) derivative. Chemical Communications 2012;48:11392. https://doi.org/10.1039/c2cc36237f.

[34] Kagan J. Applied photochemistry. Organic Photochemistry, Elsevier; 1993, p. 201–21. https://doi.org/10.1016/B978-0-12-394320-0.50015-6.

[35] Facchetti A, Marks TJ, editors. Transparent Electronics. Wiley; 2010. https://doi.org/10.1002/9780470710609.

[36] Geffroy B, le Roy P, Prat C. Organic light- emitting diode (OLED) technology: materials, devices and display technologies. Polym Int 2006;55:572–82. https://doi.org/10.1002/pi.1974.

[37] Kappaun S, Slugovc C, List E. Phosphorescent Organic Light-Emitting Devices: Working Principle and Iridium Based Emitter Materials. Int J Mol Sci 2008;9:1527–47. https://doi.org/10.3390/ijms9081527.

[38] Hughes G, Bryce MR. Electron-transporting materials for organic electroluminescent and electrophosphorescent devices. J Mater Chem 2005;15:94. https://doi.org/10.1039/b413249c.

[39] Wei Q, Fei N, Islam A, Lei T, Hong L, Peng R, et al. Small- Molecule Emitters with High Quantum Efficiency: Mechanisms, Structures, and Applications in OLED Devices. Adv Opt Mater 2018;6. https://doi.org/10.1002/adom.201800512.

[40] Udhiarto A, Haryanto LM, Khoerun B, Hartanto D. Effect of anode and cathode workfunction on the operating voltage and luminance of a single emissive layer organic light emitting diode. 2017 15th International Conference on Quality in Research (QiR) : International Symposium on Electrical and Computer Engineering, IEEE; 2017, p. 65–8. https://doi.org/10.1109/QIR.2017.8168453.

[41] Braveenth R, Kim K, Bae I-J, Raagulan K, Kim BM, Kim M, et al. Acridine Based Small Molecular Hole Transport Type Materials for Phosphorescent OLED Application. Molecules 2021;26:7680. https://doi.org/10.3390/molecules26247680.

[42] Thanikachalam V, Seransenguttuvan B, Jayabharathi J. Efficient and chromaticity stable green and white organic light-emitting devices with organic–inorganic hybrid materials. RSC Adv 2020;10:21206–21. https://doi.org/10.1039/D0RA02122A.

[43] Turak A. On the Role of LiF in Organic Optoelectronics. Electronic Materials 2021;2:198–221. https://doi.org/10.3390/electronicmat2020016.

[44] Lee CW, Lee JY. Improved power efficiency in blue phosphorescent organic light-emitting diodes using diphenylmethyl linkage based high triplet energy hole transport materials. Org Electron 2013;14:370–7. https://doi.org/10.1016/j.orgel.2012.11.004.

[45] Xu L, Yu Y, Shi J, Cui W, Lv X, Cang M, et al. Highly efficient nondoped blue organic light-emitting diodes based on a star-group tetraphenylethylene-substituted aggregation-induced-emission-active organic fluorescent small molecules. Dyes and Pigments 2020;175:108082. https://doi.org/10.1016/j.dyepig.2019.108082.

[46] Ebel K, Koehler H, Gamer AO, Jäckh R. Imidazole and Derivatives. Ullmann's Encyclopedia of Industrial Chemistry, Wiley; 2000. https://doi.org/10.1002/14356007.a13_661.

[47] Shirota Y, Kageyama H. Organic materials for optoelectronic applications: Overview. Handbook of Organic Materials for Electronic and Photonic Devices, Elsevier; 2019, p. 3–42. https://doi.org/10.1016/B978-0-08-102284-9.00001-2.

[48] Costa JCS, Taveira RJS, Lima CFRAC, Mendes A, Santos LMNBF. Optical band gaps of organic semiconductor materials. Opt Mater (Amst) 2016;58:51–60. https://doi.org/10.1016/j.optmat.2016.03.041.

[49] Schrödinger. Jaguar 2021.

[50] Bochevarov AD, Harder E, Hughes TF, Greenwood JR, Braden DA, Philipp DM, et al. Jaguar: A high- performance quantum chemistry software program with strengths in life and materials sciences. Int J Quantum Chem 2013;113:2110–42. https://doi.org/10.1002/qua.24481.

[51] Alemdar Yılmaz E. Rational molecular design enables efficient organic solar cells and organic light emitting devices. Middle East Technical University, 2022.

[52] Yu HY, Feng XD, Grozea D, Lu ZH, Sodhi RNS, Hor A-M, et al. Surface electronic structure of plasma-treated indium tin oxides. Appl Phys Lett 2001;78:2595–7. https://doi.org/10.1063/1.1367897.

[53] Mason MG, Hung LS, Tang CW, Lee ST, Wong KW, Wang M. Characterization of treated indium–tin–oxide surfaces used in electroluminescent devices. J Appl Phys 1999;86:1688–92. https://doi.org/10.1063/1.370948.

[54] Wu CC, Wu CI, Sturm JC, Kahn A. Surface modification of indium tin oxide by plasma treatment: An effective method to improve the efficiency, brightness, and reliability of organic light emitting devices. Appl Phys Lett 1997;70:1348–50. https://doi.org/10.1063/1.118575.

[55] Gong P, Xue P, Qian C, Zhang Z, Lu R. Balanced π–π interactions directing the self-assembly of indolocarbazole-based low molecular mass organogelators. Org Biomol Chem 2014;12:6134–44. https://doi.org/10.1039/C4OB00873A.

[56] Ma S, Du S, Pan G, Dai S, Xu B, Tian W. Organic molecular aggregates: From aggregation structure to emission property. Aggregate 2021;2. https://doi.org/10.1002/agt2.96.

[57] Liu X, Wei X, Miao Y, Tao P, Wang H, Xu B. Triphenylamine-based small molecules with aggregation-induced emission and mechanochromic luminescence properties for OLED application. Tetrahedron 2021;86:132061. https://doi.org/10.1016/j.tet.2021.132061.

[58] Deng Y, Yuan W, Jia Z, Liu G. H- and J-Aggregation of Fluorene-Based Chromophores. J Phys Chem B 2014;118:14536–45. https://doi.org/10.1021/jp510520m.

[59] Khasbaatar A, Xu Z, Lee J-H, Campillo-Alvarado G, Hwang C, Onusaitis BN, et al. From Solution to Thin Film: Molecular Assembly of π-Conjugated Systems and Impact on (Opto)electronic Properties. Chem Rev 2023;123:8395–487. https://doi.org/10.1021/acs.chemrev.2c00905.

[60] Lawson-Wood K "Upstone, S". Determination of Relative Fluorescence Quantum Yields using the FL6500 Fluorescence Spectrometer. UK: 2018.

[61] Brouwer AM. Standards for photoluminescence quantum yield measurements in solution (IUPAC Technical Report). Pure and Applied Chemistry 2011;83:2213–28. https://doi.org/10.1351/PAC-REP-10-09-31.

[62] Deng P, Liu L, Ren S, Li H, Zhang Q. N-acylation: an effective method for reducing the LUMO energy levels of conjugated polymers containing five-membered lactam units. Chemical Communications 2012;48:6960. https://doi.org/10.1039/c2cc32184j.

[63] Li Y., Cao Y., Gao J., Wang D., Yu G. "Heeger, A." Electrochemical properties of luminescent polymers and polymer light-emitting electrochemical cells. Synth Met 1999;99:243–8.

[64] Liu Y., Liu MS., Jen AK-Y. Synthesis and characterization of a novel and highly efficient light-emitting polymer. Acta Polymerica 1999;50:105–8.

[65] Chen W-C, Yuan Y, Xiong Y, Rogach AL, Tong Q-X, Lee C-S. Aromatically C6- and C9-Substituted Phenanthro[9,10- *d*]imidazole Blue Fluorophores: Structure–Property Relationship and Electroluminescent Application. ACS Appl Mater Interfaces 2017;9:26268–78. https://doi.org/10.1021/acsami.7b06547.

[66] Li X, Yang M, Chen X, Jia J, Zhao W, Wu X, et al. Synergistic Intra- and Intermolecular Noncovalent Interactions for Ultralong Organic Phosphorescence. Small 2019;15. https://doi.org/10.1002/smll.201903270.

[67] Chen W, Yuan Y, Wu G, Wei H, Tang L, Tong Q, et al. Staggered Face-to- Face Molecular Stacking as a Strategy for Designing Deep- Blue Electroluminescent Materials with High Carrier Mobility. Adv Opt Mater 2014;2:626–31. https://doi.org/10.1002/adom.201400078.

[68] Xie F-M, An Z-D, Xie M, Li Y-Q, Zhang G-H, Zou S-J, et al. *tert* -Butyl substituted hetero-donor TADF compounds for efficient solution-processed non-doped blue OLEDs. J Mater Chem C Mater 2020;8:5769–76. https://doi.org/10.1039/D0TC00718H.

[69] Hu D, Zhu M, Shi C, Yuan W, Sun N, Huang B, et al. Manipulating peripheral non-conjugated substituents in carbazole/oxadiazole hybrid TADF emitters towards high-efficiency OLEDs. J Mater Chem C Mater 2021;9:13384–91. https://doi.org/10.1039/D1TC02778F.

[70] Feng Q, Zheng X, Wang H, Zhang H, Qian Y, Tan K, et al. A 9-fluorenyl substitution strategy for aromatic-imide-based TADF emitters towards efficient and stable sky blue OLEDs with nearly 30% external quantum efficiency. Mater Adv 2021;2:4000–8. https://doi.org/10.1039/D1MA00181G.

[71] Bezvikonnyi O, Bernard RS, Andruleviciene V, Volyniuk D, Keruckiene R, Vaiciulaityte K, et al. Derivatives of Imidazole and Carbazole as Bifunctional Materials for Organic Light-Emitting Diodes. Materials 2022;15:8495. https://doi.org/10.3390/ma15238495.

APPENDICES

A. NMR Spectra

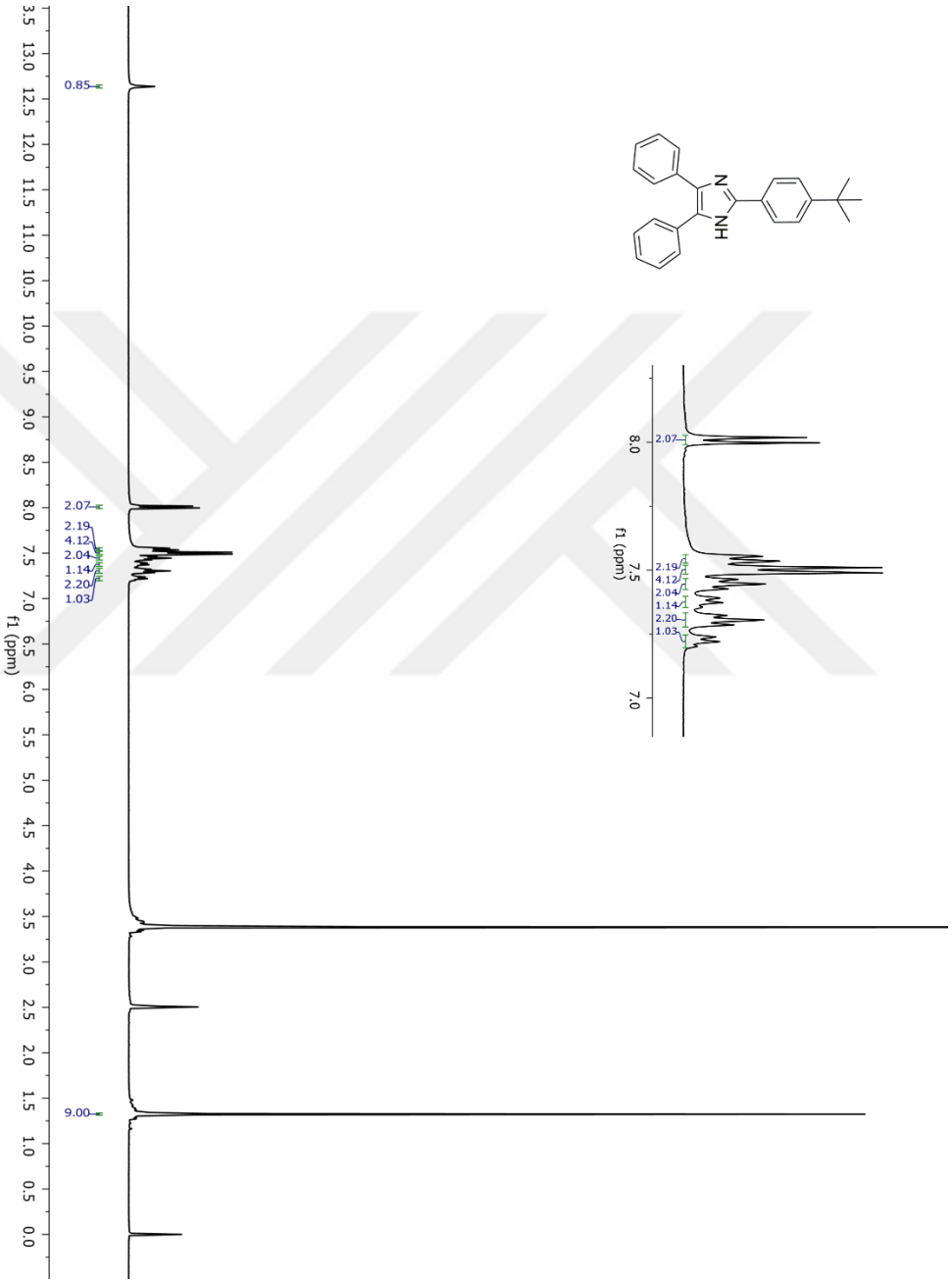

Figure A.1. ^{1}H NMR spectrum of molecule BIm-H-*t*Bu in DMSO-d_6

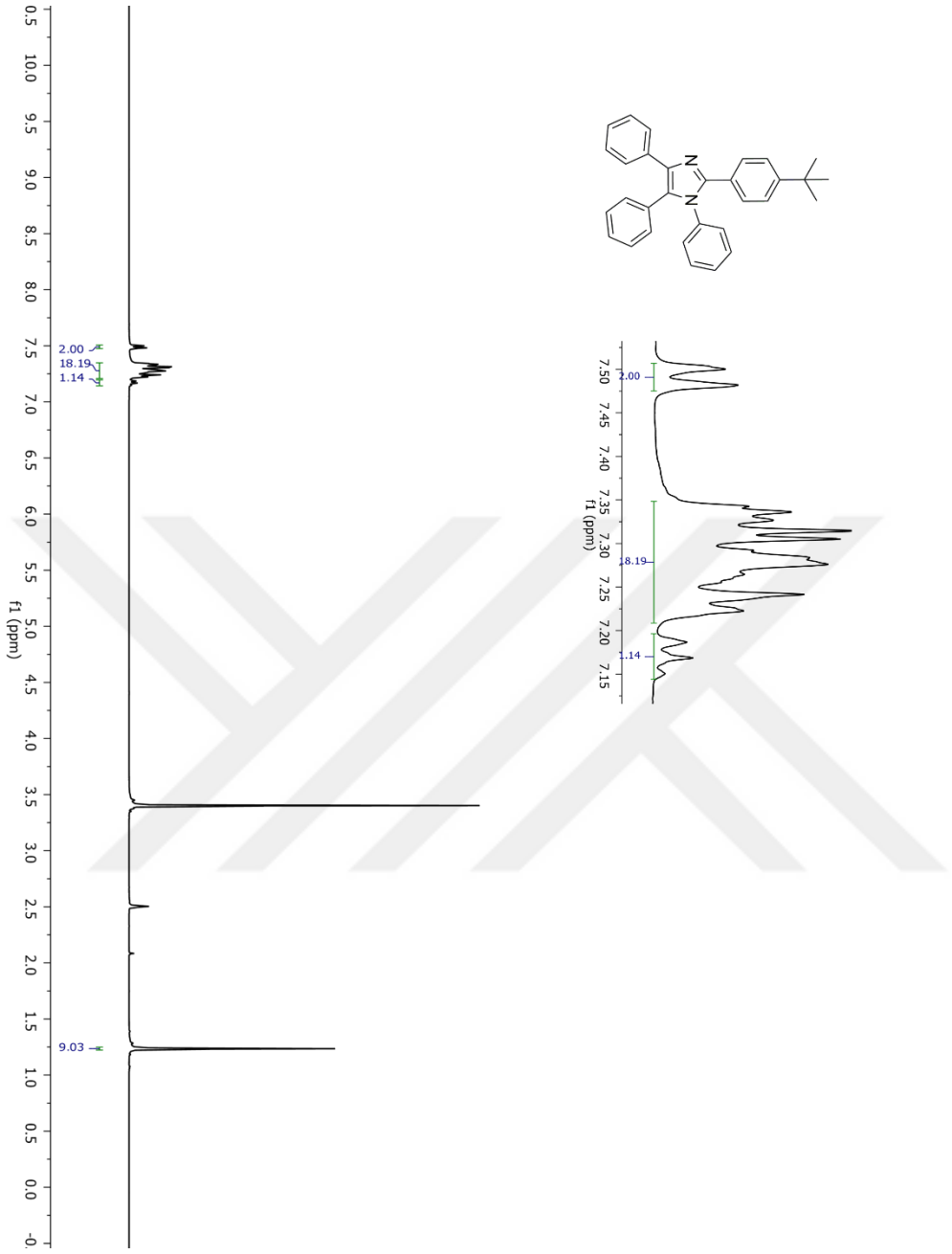

Figure A.2. ^{1}H NMR spectrum of compound BIm-Ph-*t*Bu in DMSO-d_6

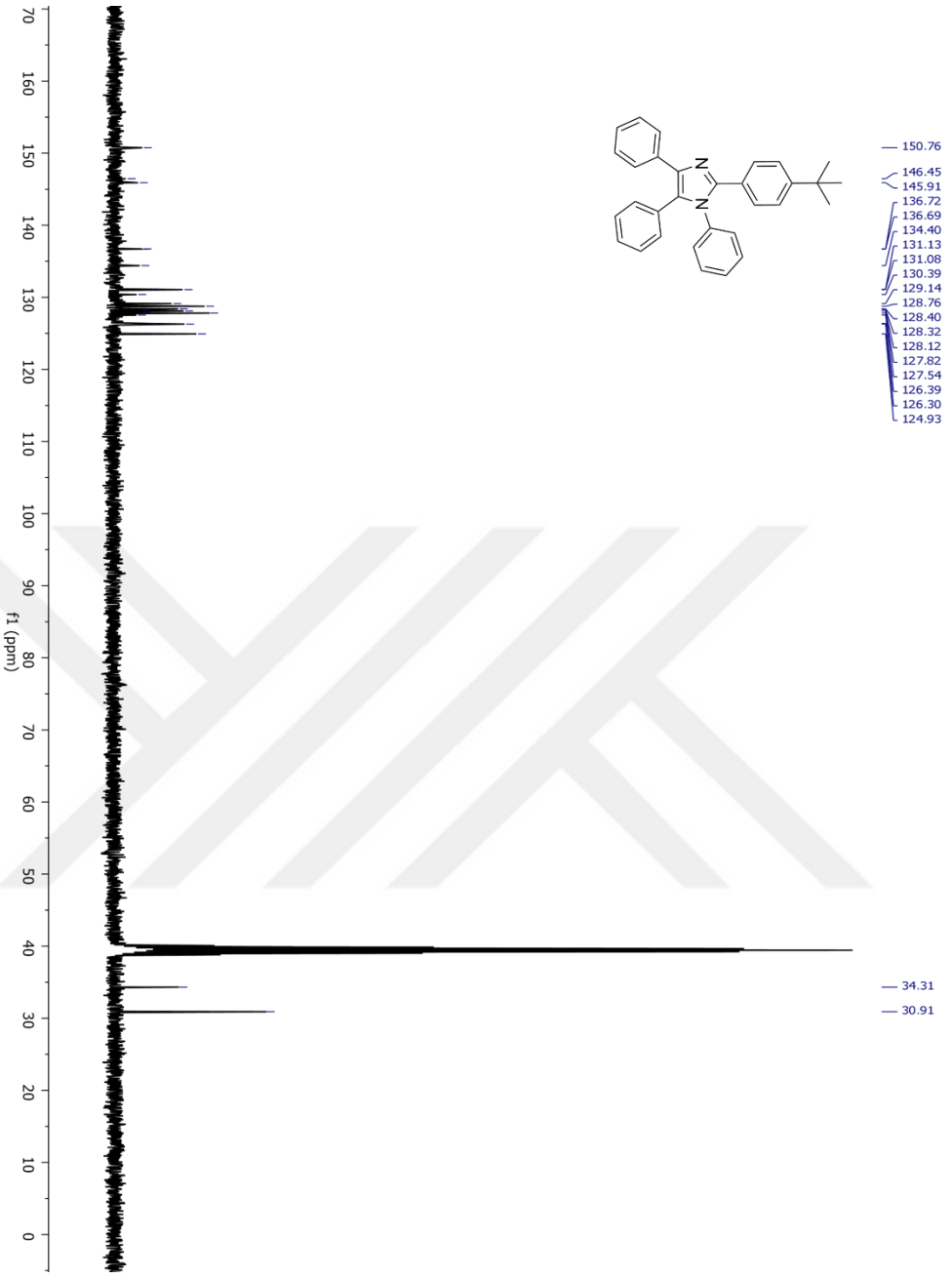

Figure A.3. ^{13}C NMR spectrum of compound BIm-Ph-*t*Bu in DMSO-d_6

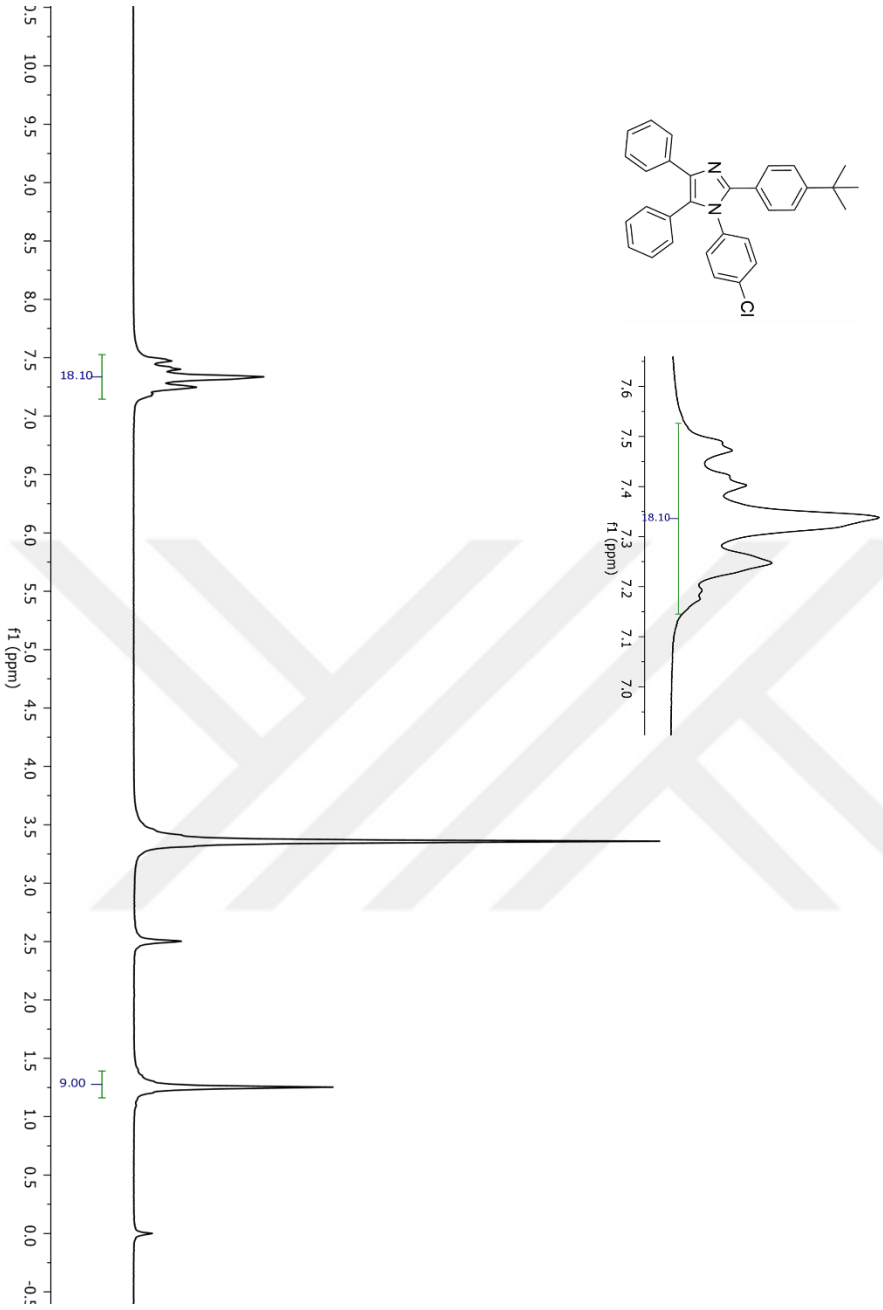

Figure A.4. ^{1}H NMR spectrum of compound BIm-PhCl-*t*Bu in DMSO-d_6

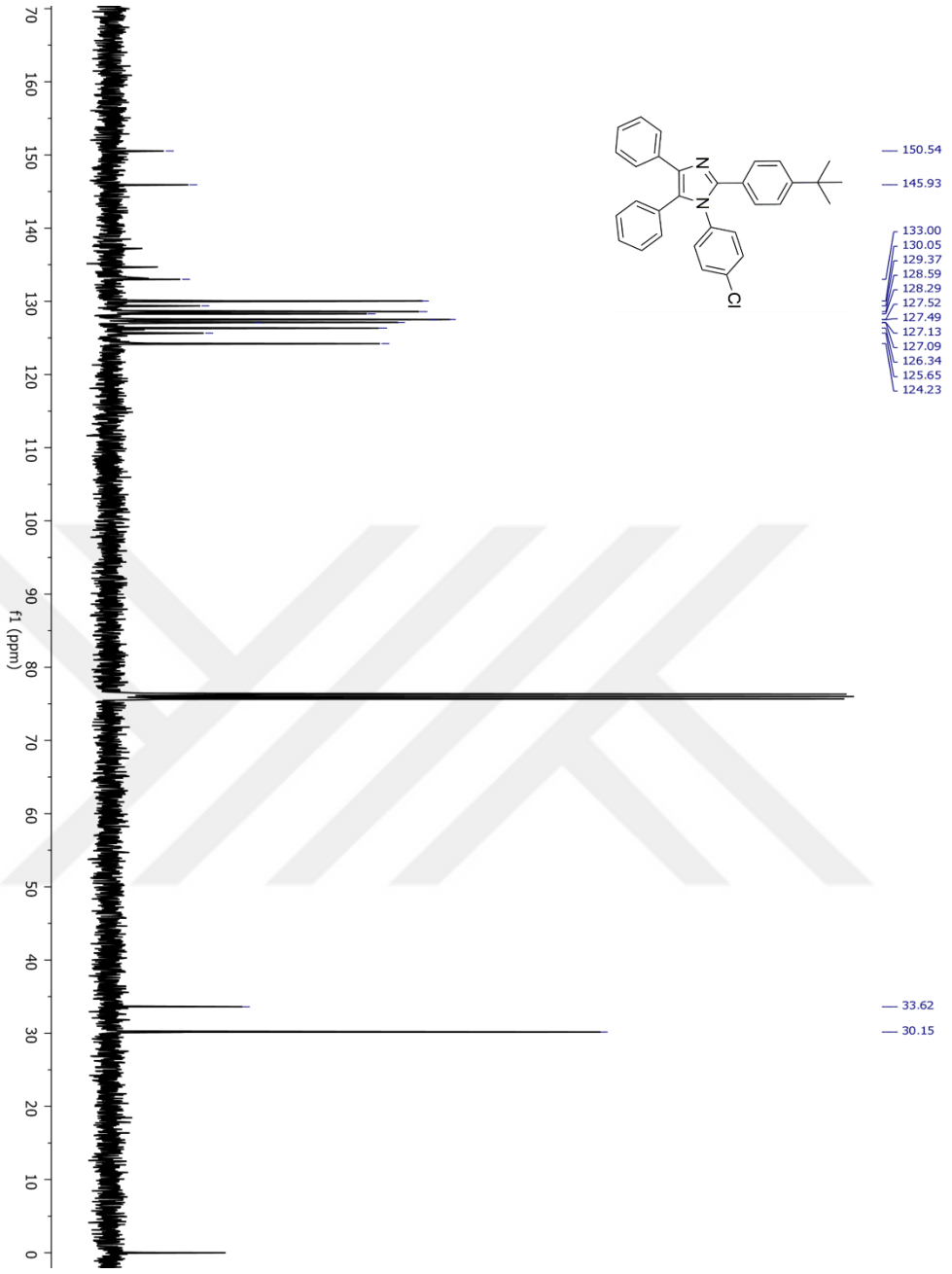

Figure A.5. ^{13}C NMR spectrum of compound BIm-PhCl-*t*Bu in $CDCl_3$

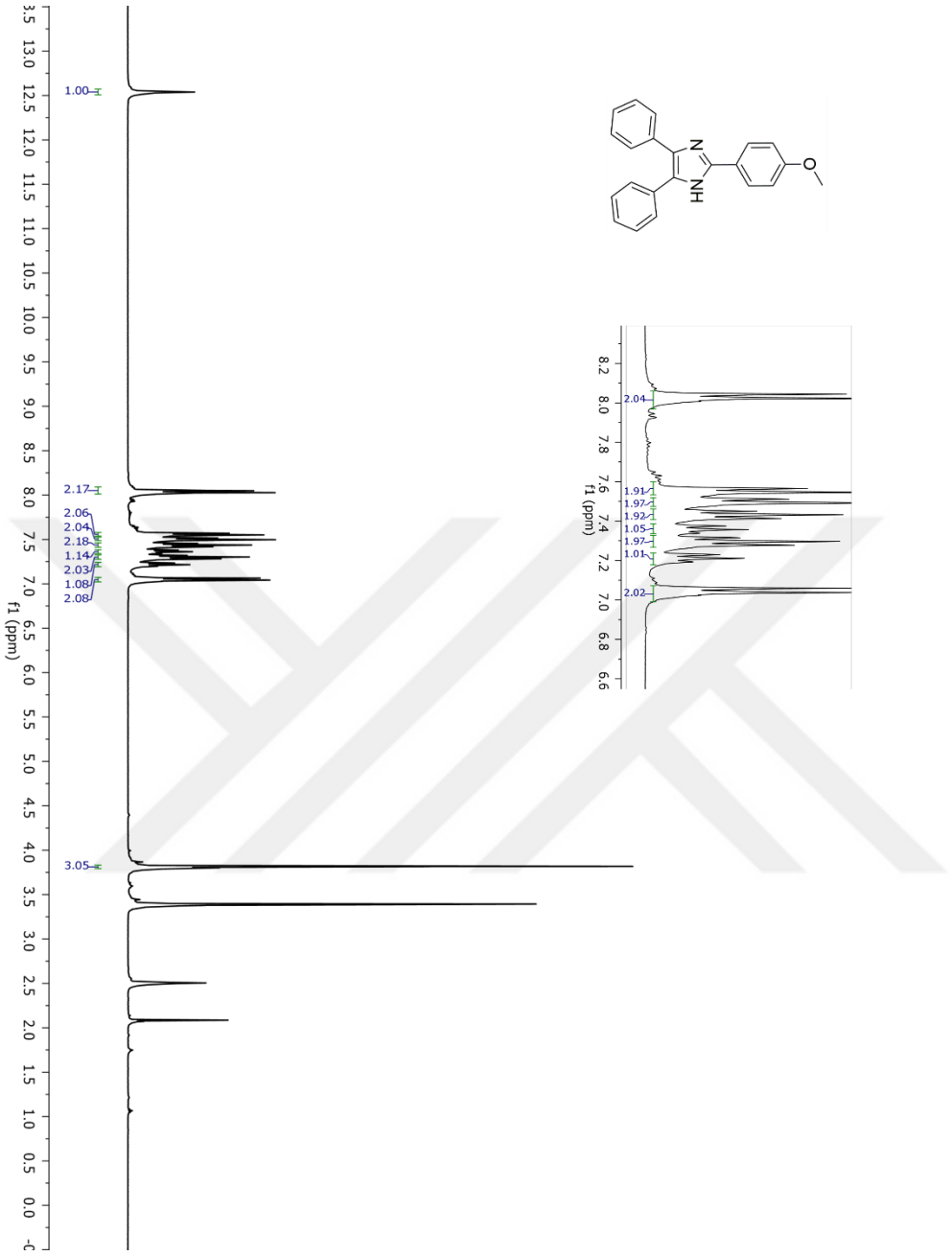

Figure A.6. ^{1}H NMR spectrum of compound BIm-H-OMe in DMSO-d_6

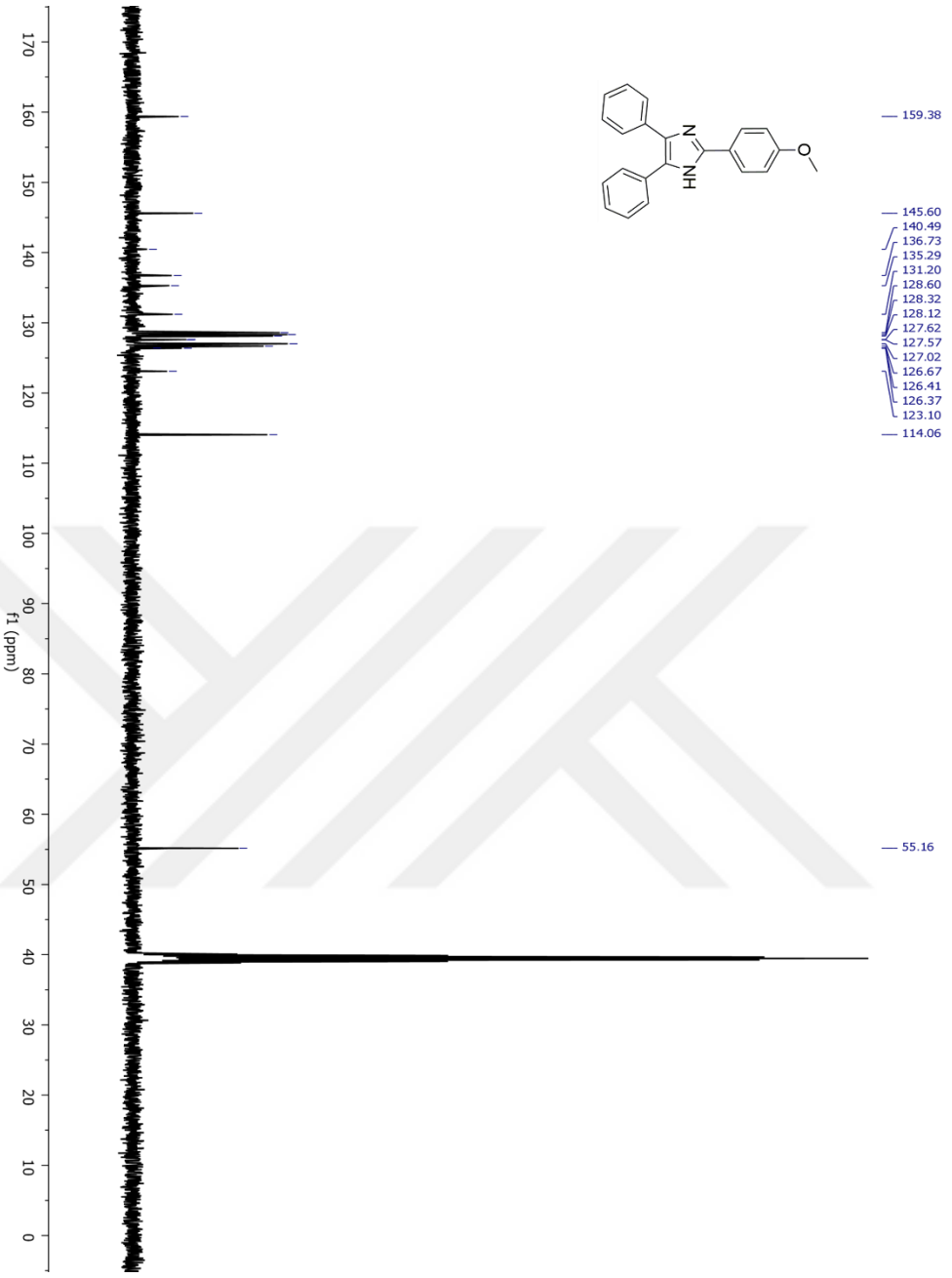

Figure A.7. ^{13}C NMR spectrum of compound BIm-H-OMe in DMSO-d_6

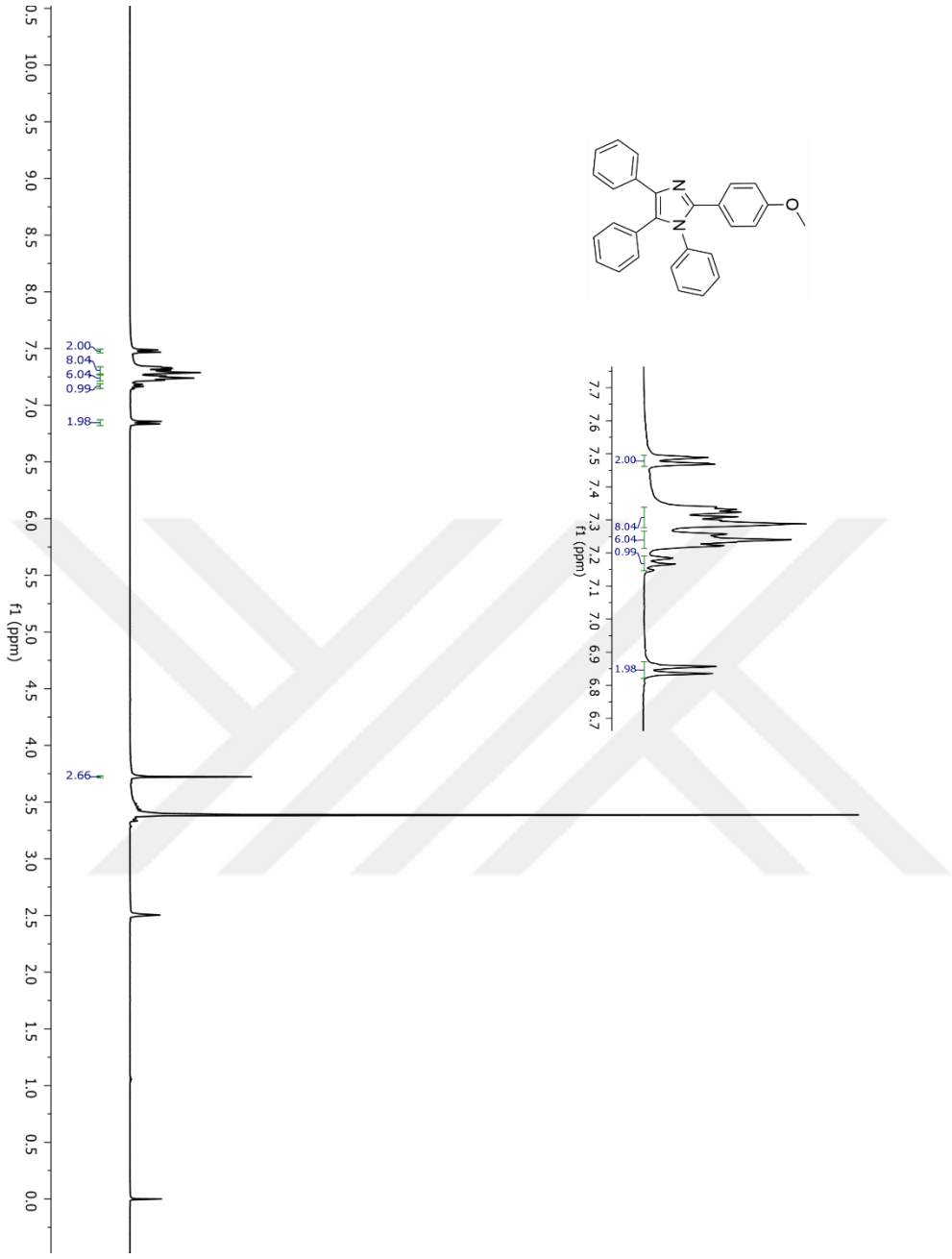

Figure A.8. ^{1}H NMR spectrum of compound BIm-Ph-OMe in DMSO-d_6

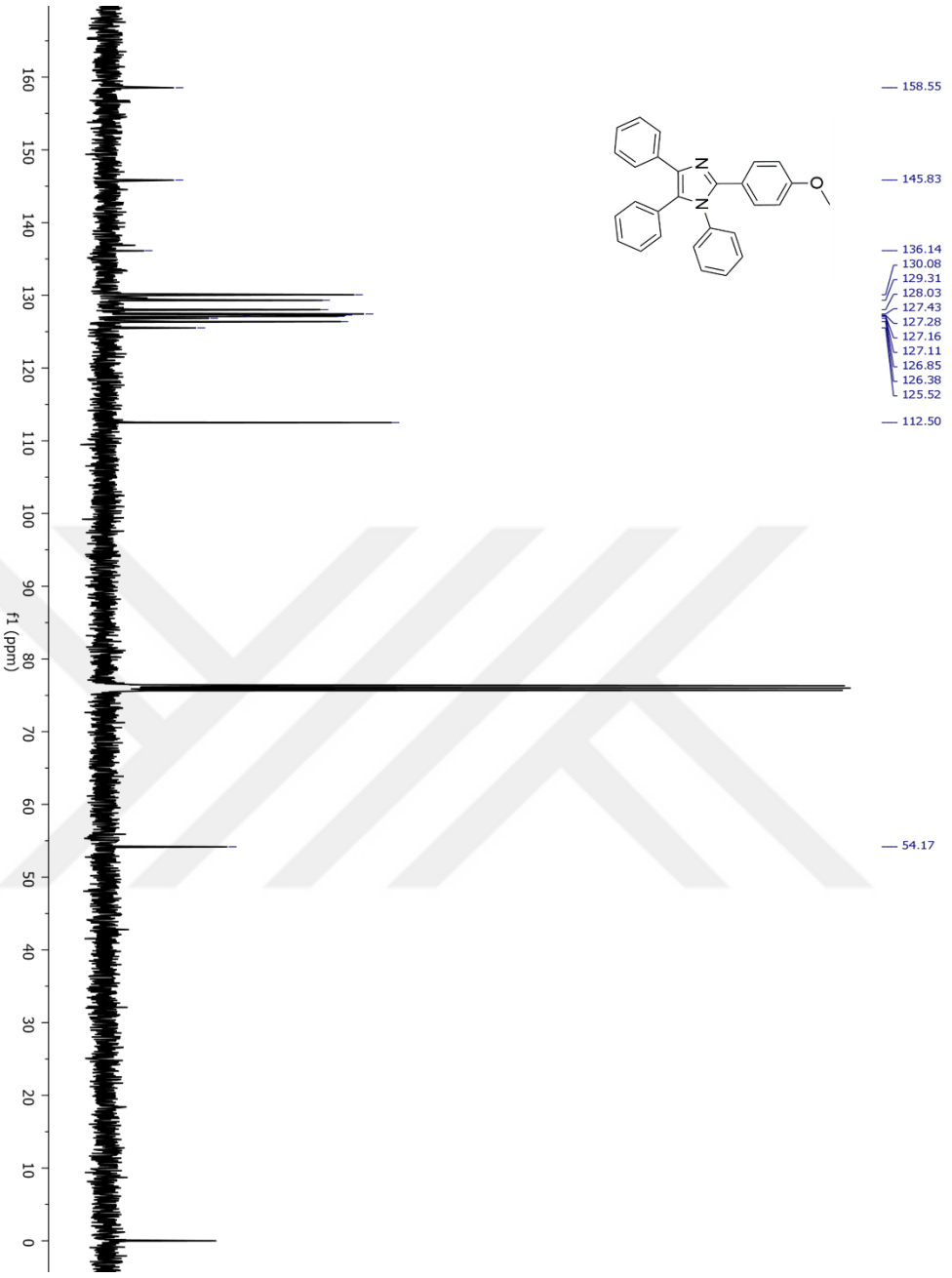

Figure A.9. ^{13}C NMR spectrum of compound BIm-Ph-OMe in $CDCl_3$

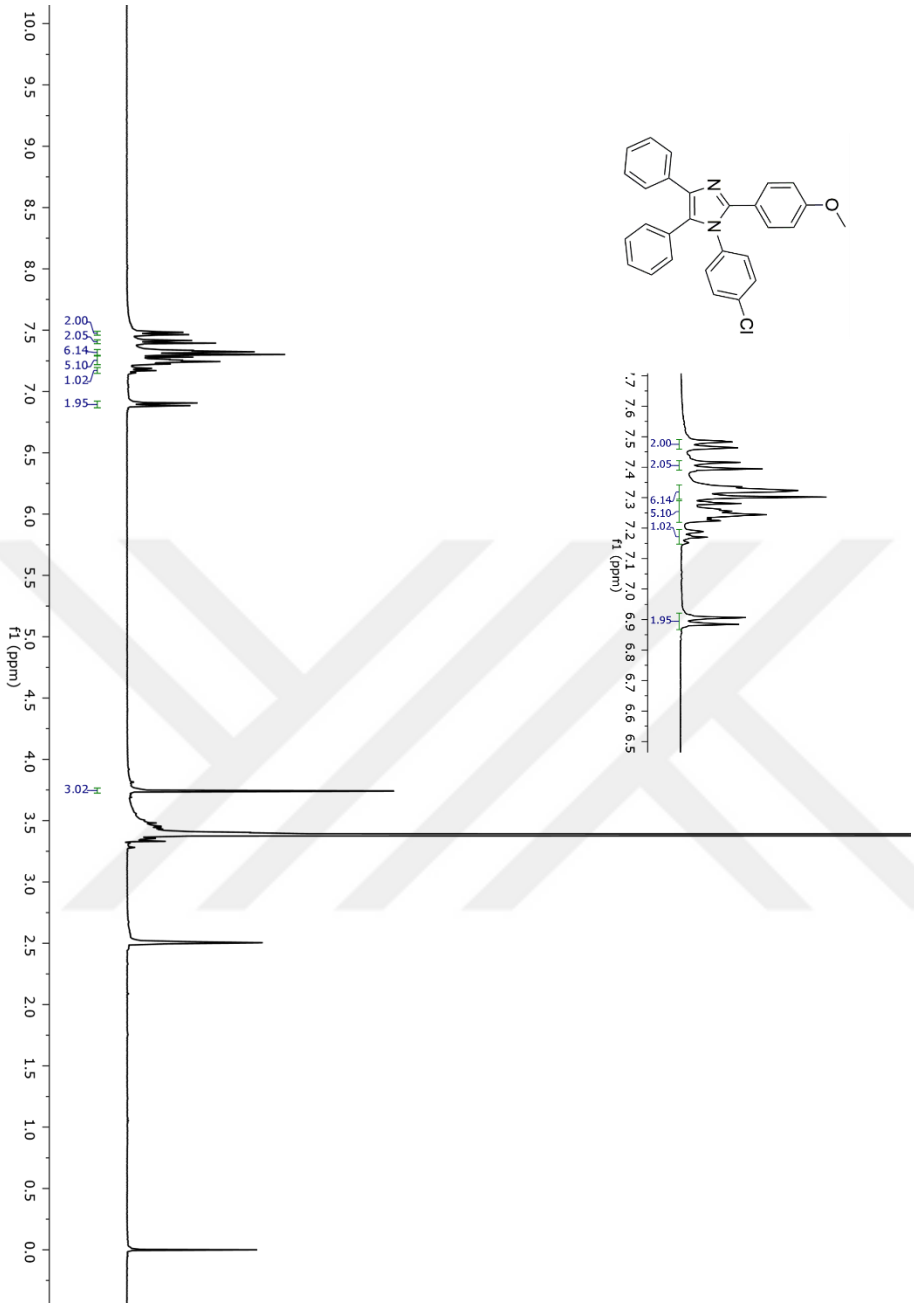

Figure A.10. ^{1}H NMR spectrum of compound BIm-PhCl-OMe in DMSO-d_6

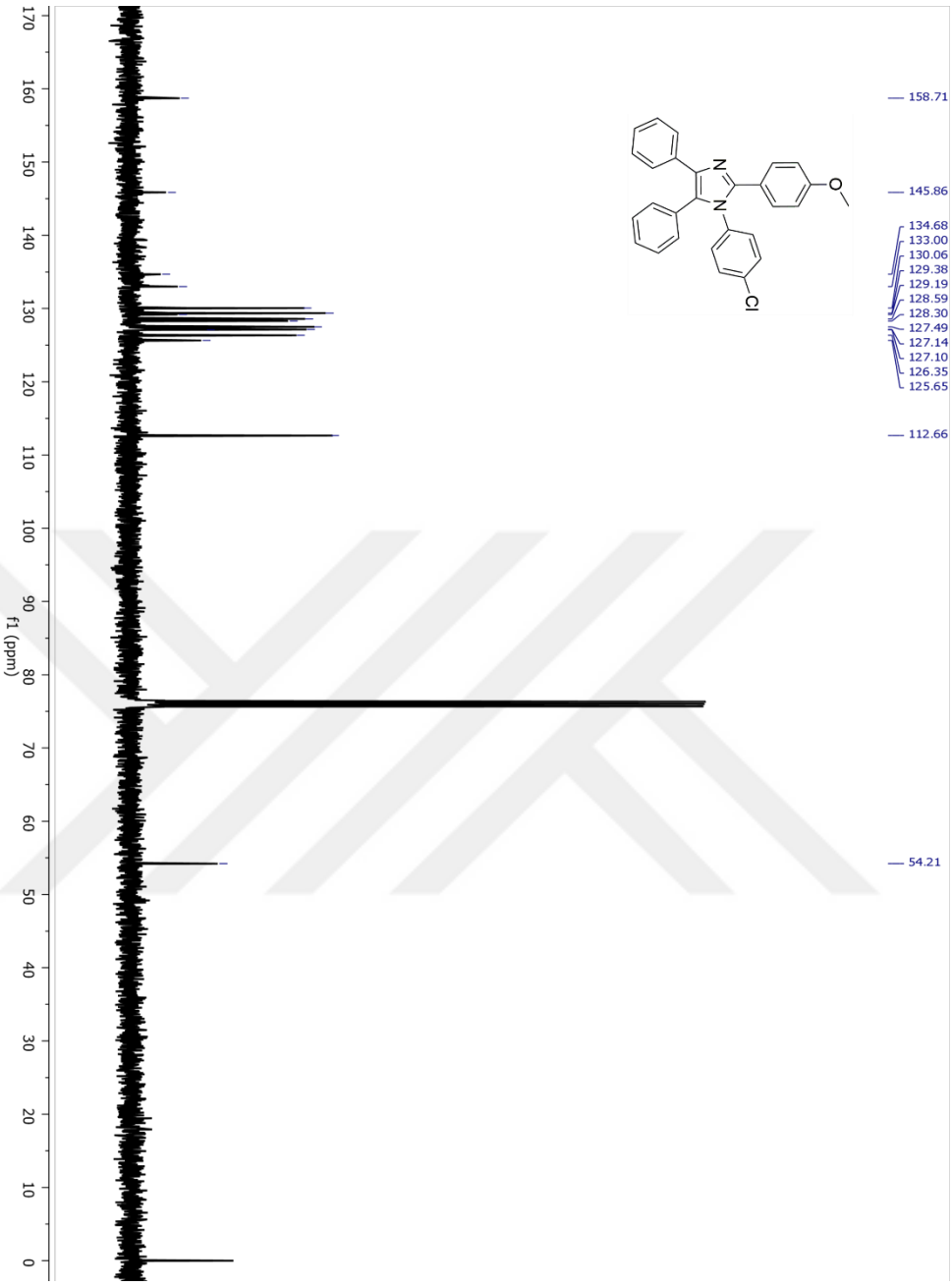

Figure A.11. ^{13}C NMR spectrum of compound BIm-PhCl-OMe in $CDCl_3$

B. HRMS

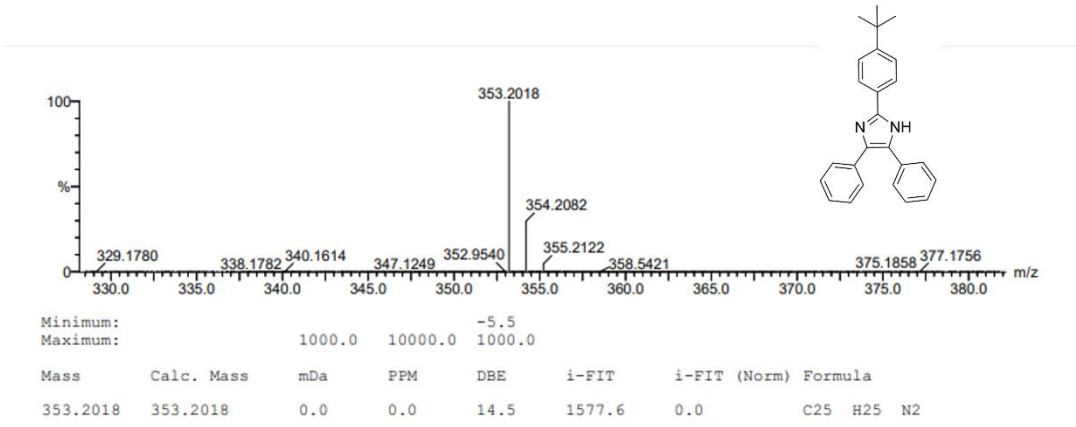

Minimum:			-5.5			
Maximum:		1000.0	10000.0	1000.0		
Mass	Calc. Mass	mDa	PPM	DBE	i-FIT	i-FIT (Norm)	Formula
353.2018	353.2018	0.0	0.0	14.5	1577.6	0.0	C25 H25 N2

Figure B.1. HRMS result of compound BIm-H-*t*Bu

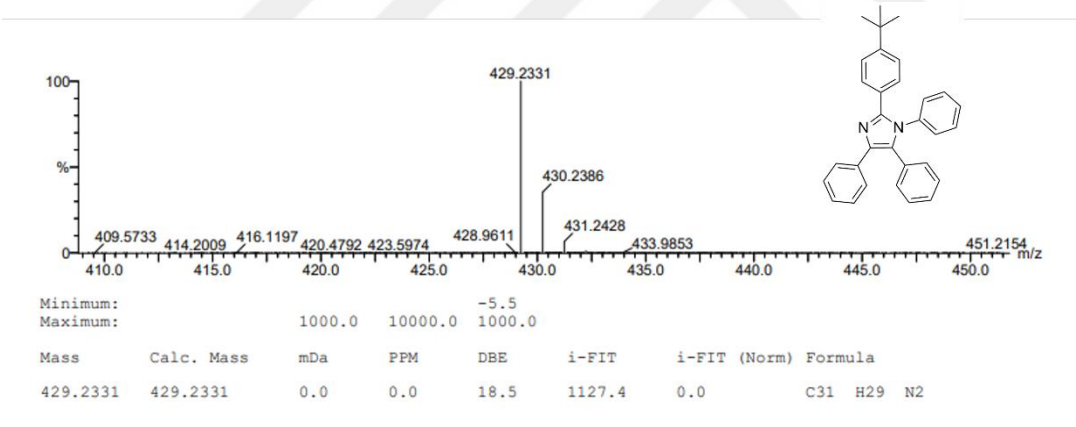

Minimum:			-5.5			
Maximum:		1000.0	10000.0	1000.0		
Mass	Calc. Mass	mDa	PPM	DBE	i-FIT	i-FIT (Norm)	Formula
429.2331	429.2331	0.0	0.0	18.5	1127.4	0.0	C31 H29 N2

Figure B.2. HRMS result of compound BIm-Ph-*t*Bu

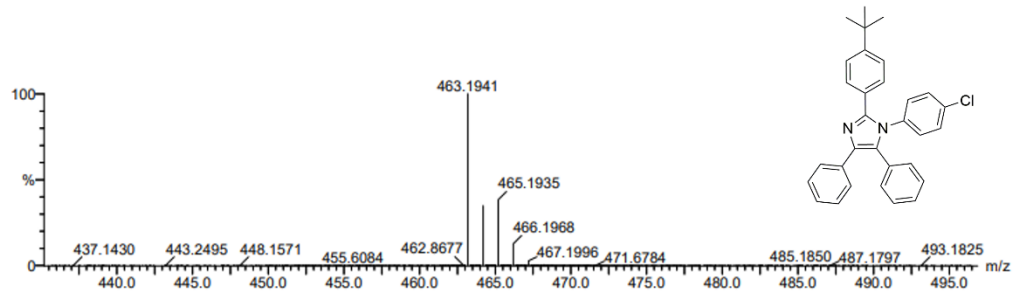

Minimum:				-5.5			
Maximum:		1000.0	10000.0	1000.0			
Mass	Calc. Mass	mDa	PPM	DBE	i-FIT	i-FIT (Norm)	Formula
463.1941	463.1941	0.0	0.0	18.5	1205.3	0.0	C31 H28 N2 Cl

Figure B.3. HRMS result of compound BIm-PhCl-*t*Bu

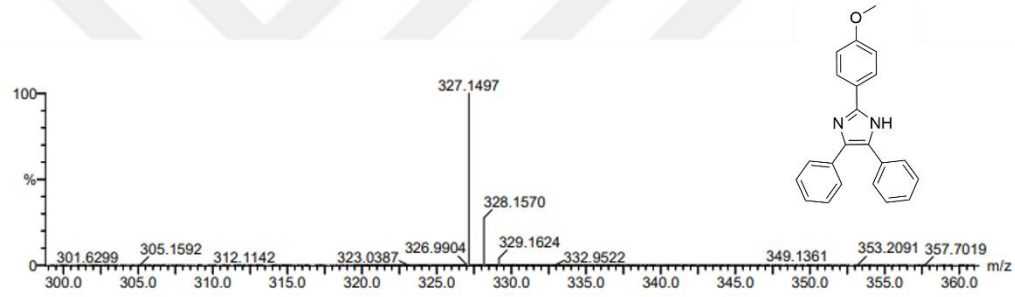

Minimum:				-5.5			
Maximum:		1000.0	10000.0	1000.0			
Mass	Calc. Mass	mDa	PPM	DBE	i-FIT	i-FIT (Norm)	Formula
327.1497	327.1497	0.0	0.0	14.5	1237.5	0.0	C22 H19 N2 O

Figure B.4. HRMS result of compound BIm-H-OMe

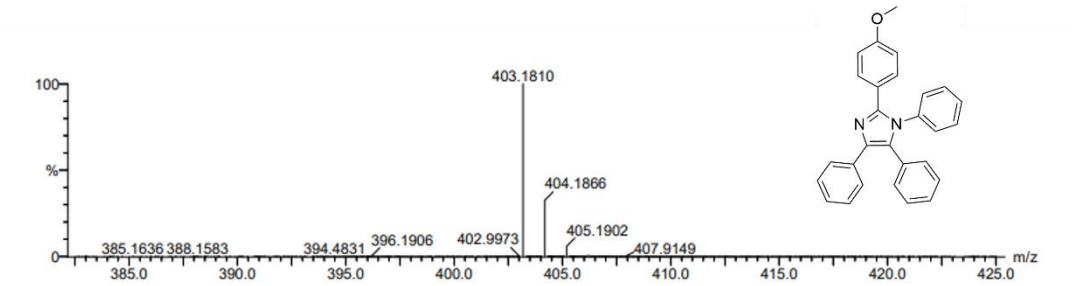

Minimum:				-5.5			
Maximum:		1000.0	10000.0	1000.0			
Mass	Calc. Mass	mDa	PPM	DBE	i-FIT	i-FIT (Norm)	Formula
403.1810	403.1810	0.0	0.0	18.5	1336.4	0.0	C28 H23 N2 O

Figure B.5. HRMS result of compound BIm-Ph-OMe

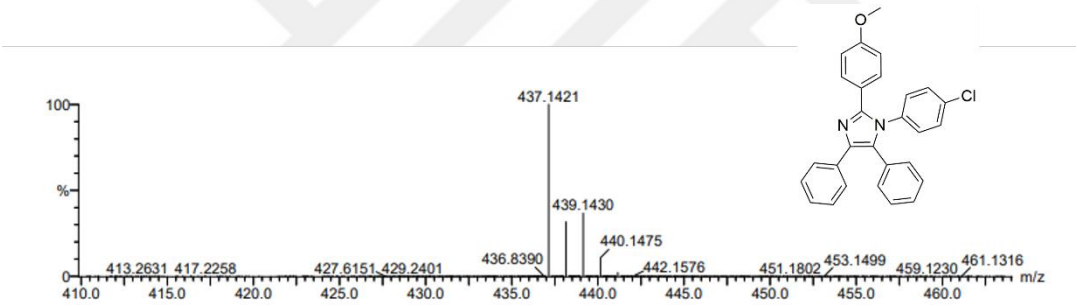

Minimum:				-5.5			
Maximum:		1000.0	10000.0	1000.0			
Mass	Calc. Mass	mDa	PPM	DBE	i-FIT	i-FIT (Norm)	Formula
437.1421	437.1421	0.0	0.0	18.5	1083.0	0.0	C28 H22 N2 O Cl

Figure B.6. HRMS result of compound BIm-PhCl-OMe